

Discrete X-ray Sources
in the Small Magellanic Cloud
— Tracing the Star Forming Activity —

Jun Yokogawa

*Department of Physics, Graduate School of Science,
Kyoto University, Sakyo-ku, Kyoto 606-8502, Japan*

Submitted to the Department of Physics, Kyoto University
in partial fulfillment of the requirements
for the degree of Doctor of Science

January 7, 2002

This thesis will be available at
<http://www-cr.scphys.kyoto-u.ac.jp/member/jun/job/phd/>.

Abstract

The Advanced Satellite for Cosmology and Astrophysics (ASCA) has made 22 observations on the Small Magellanic Cloud (SMC) by the end of the mission. We performed systematic analyses on all of these observation data and made comprehensive catalogues. We detected 106 discrete sources with a criterion of $S/N > 5$. The source positions were determined with an $\sim 40''$ error radius (90% confidence) for sources detected in the central $20'$ radius of the GIS. We detected coherent pulsations from 17 sources. Among them, eight were newly discovered during this study. We classified most of these pulsars as X-ray binary pulsars (XBPs) based on their properties such as flux variability. X-ray emission was detected from eight supernova remnants (SNRs). Among them, five SNRs showed emission lines in their spectra, hence we regarded the five as thermal. We find that XBPs and thermal SNRs in the SMC can be clearly separated by their spectral hardness ratio. Applying this empirical law to faint (thus unclassified) sources, we find 20 XBP candidates and four thermal SNR candidates. We find the spatial distributions of the XBPs and thermal SNRs (including candidates) resemble the distribution of young stars with ages $\sim 2 \times 10^7$ yr. We compare the source populations in the SMC and in our Galaxy and discuss the star forming activity of the SMC.

Contents

1	Introduction	1
2	Review — the Small Magellanic Cloud	3
2.1	The Magellanic System	5
2.2	Interaction between the Magellanic Clouds and our Galaxy	6
2.3	Structure of the Small Magellanic Cloud	7
2.4	Previous High Energy Observations	10
2.4.1	X-ray surveys	10
2.4.2	GeV and TeV γ -ray observations	12
3	Instruments	15
3.1	Overview of the ASCA Satellite	15
3.2	XRT: X-ray Telescope	15
3.3	GIS: Gas Imaging Spectrometer	19
3.4	SIS: Solidstate Imaging Spectrometer	22
4	Observations and Data Reduction	27
4.1	Observation Fields	27
4.2	Data Reduction	27

5	Systematic Analyses on Discrete Sources	31
5.1	X-Ray Images	31
5.1.1	Images in the sky/detector coordinate systems	31
5.1.2	Source extraction	32
5.1.3	Construction of mosaic images	32
5.2	Position Determination	33
5.2.1	Absolute accuracy of the position	36
5.2.2	Identification of sources detected in multiple ASCA observations	39
5.3	Timing Analyses	42
5.4	Spectral Analyses	44
5.4.1	Overview	44
5.4.2	Hardness ratio	44
5.4.3	SNRs	45
5.4.4	X-ray pulsars and HMXBs	46
5.4.5	Remaining sources	46
5.5	Catalogue of Discrete X-Ray Sources in the SMC Region	47
5.5.1	Catalogue – I. Source identification	47
5.5.2	Catalogue – II. Names and comments	51
5.5.3	Catalogue – III. Spectral parameters	55
6	Comments on Specific Sources and Pulsar Statistics	59
6.1	X-Ray Pulsars	59
6.1.1	Overview	59
6.1.2	No. 17 — AX J0043–737	60
6.1.3	No. 24 — AX J0049–729	63

6.1.4	No. 26 — AX J0049–732	65
6.1.5	No. 30 — AX J0049.5–7323	66
6.1.6	No. 32 — AX J0051–733	68
6.1.7	No. 37 — AX J0051–722	71
6.1.8	No. 40 — AX J0051.6–7311	72
6.1.9	No. 43 — RX J0052.1–7319?	73
6.1.10	No. 44 — XTE J0054–720	75
6.1.11	No. 47 — 1WGA J0053.8–7226 = XTE J0053–724	76
6.1.12	No. 49 — SMC X-2	76
6.1.13	No. 51 — XTE J0055–724 = 1SAX J0054.9–7226	79
6.1.14	No. 56 — AX J0057.4–7325	80
6.1.15	No. 61 — AX J0058–7203	82
6.1.16	No. 67 — RX J0059.2–7138	84
6.1.17	No. 74 — RX J0101.3–7211	86
6.1.18	No. 78 — 1SAX J0103.2–7209	87
6.1.19	No. 83 — AX J0105–722	88
6.1.20	No. 90 — XTE J0111.2–7317	90
6.1.21	No. 94 — SMC X-1	92
6.1.22	Other pulsars not detected with ASCA — 2E 0050.1–7247, XTE J0052–723, RX J0117.6–7330, and XTE J0050–732#1 and #2	94
6.2	Period Distribution of XBPs	96
6.3	SNRs – I: from SIS	101
6.3.1	No. 21 — 0045–734 (N19)	101
6.3.2	No. 25 — 0047–735	104

6.3.3	No. 66 — 0057–7226 (N66)	104
6.3.4	No. 81 — 0102–723	106
6.3.5	No. 82 — 0103–726	106
6.4	SNRs – II: from GIS	109
6.4.1	No. 23 — 0046–735	109
6.4.2	No. 36 — 0049–736	109
6.4.3	No. 64 — 0056–725	110
6.5	Other Interesting Sources	112
6.5.1	No. 20 — IKT1	112
6.5.2	No. 22 — AX J0048.2–7309	113
6.5.3	No. 105 — AX J0128.4–7329	114
7	Source Classification	117
7.1	Criteria for Source Classification	117
7.2	Classification by Hardness Ratio	119
7.2.1	XBPs and thermal SNRs	119
7.2.2	Validity of the classification by hardness ratio	121
7.2.3	Candidates for XBPs and thermal SNRs	122
8	Implication for the Star Forming Activity	125
8.1	Source Populations in the SMC and in our Galaxy	125
8.1.1	Basic data	125
8.1.2	Comparison of the source populations	126
8.2	Spatial Distribution of Various Classes of Sources	128
9	Conclusion	131

A Two Color X-Ray Mosaic Image of the SMC

133

List of Figures

2.1	Photo of a Cerro Tololo sky	3
2.2	Optical images of the Magellanic Clouds	4
2.3	H I distribution of the Magellanic System	5
2.4	Spatial distribution of stars with different ages	8
2.5	H I distribution in the SMC	9
2.6	Distances to Cepheids in the SMC	9
2.7	X-ray view of the SMC in late 1970's	10
2.8	X-ray view of the SMC with ROSAT PSPC	11
3.1	Schematic view of ASCA	16
3.2	Mechanism of an X-ray telescope	17
3.3	Effective area of XRT vs. X-ray energy	17
3.4	Effective area of XRT vs. off-axis angle	18
3.5	Point spread function of XRT	18
3.6	Stray light of XRT	19
3.7	Schematic view of GIS	20
3.8	Effective area of GIS with XRT	21
3.9	SIS chip configuration	23

3.10	Effective area of SIS with XRT	23
3.11	Grade definition for an SIS event	25
4.1	Observation fields of ASCA	29
5.1	X-ray mosaic image of the SMC (0.7–2.0 keV)	34
5.2	X-ray mosaic image of the SMC (2.0–7.0 keV)	35
5.3	Separation angles between the selected ROSAT–ASCA counterparts	37
5.4	Separation vs. off-axis for ASCA sources detected multiple times	40
5.5	Examples of power spectrum densities	43
5.6	Periodogram for XTE J0055–724	43
6.1	History of pulsar discoveries in the SMC	60
6.2	Power spectrum densities of AX J0043–737	62
6.3	GIS spectrum and pulse profile of AX J0043–737	63
6.4	GIS spectrum and pulse profiles of AX J0049–729	64
6.5	GIS spectrum and pulse profile of AX J0049–732	66
6.6	GIS spectrum and pulse profiles of AX J0049.5–7323	67
6.7	GIS spectrum and pulse profiles of AX J0051–733	69
6.8	Light curves of AX J0051–733 in obs. Q	70
6.9	GIS spectrum and pulse profiles of AX J0051–722	71
6.10	GIS spectrum and pulse profiles of AX J0051.6–7311	73
6.11	GIS spectrum of No. 43 (= RX J0052.1–7319?)	74
6.12	GIS spectrum and pulse profiles of XTE J0054–720	75
6.13	GIS spectrum and pulse profiles of 1WGA J0053.8–7226	77
6.14	GIS spectrum and pulse profiles of SMC X-2	78

6.15	ROSAT PSPC image around SMC X-2	79
6.16	GIS spectrum of XTE J0055–724	80
6.17	GIS spectrum and pulse profiles of AX J0057.4–7325	81
6.18	GIS spectrum and pulse profiles of AX J0058–7203	83
6.19	Power spectrum densities of AX J0058–7203	84
6.20	GIS spectrum and pulse profiles of RX J0059.2–7138	85
6.21	GIS spectrum and pulse profiles of RX J0101.3–7211	86
6.22	GIS spectrum and pulse profiles of 1SAX J0103.2–7209	88
6.23	GIS images around AX J0105–722	89
6.24	GIS spectrum and pulse profiles of AX J0105–722	90
6.25	GIS spectrum and pulse profiles of XTE J0111.2–7317	91
6.26	GIS spectra and pulse profiles of SMC X-1 in obs. A and I	93
6.27	GIS spectrum and pulse profiles of SMC X-1 in obs. C	94
6.28	Period distribution of XBPs in the SMC and our Galaxy	97
6.29	Period vs. minimum luminosity of XBPs in the SMC	99
6.30	SIS spectrum and ROSAT HRI image of 0045–734	102
6.31	Element mass and theoretical predictions for 0045–734	104
6.32	SIS spectrum of 0047–735	105
6.33	SIS spectrum and ROSAT HRI image of 0057–7226	106
6.34	SIS spectrum and ROSAT HRI image of 0103–726	107
6.35	Element mass and theoretical predictions for 0103–726	108
6.36	GIS spectrum of 0046–735	109
6.37	GIS spectrum of 0049–736	110
6.38	GIS spectrum of 0056–725	111

6.39	GIS spectrum of IKT1	112
6.40	Light curves of IKT1 in obs. Q	113
6.41	GIS spectra of AX J0048.2–7309	114
6.42	GIS spectrum of AX J0128.4–7329	115
7.1	HR vs. L_{obs} for XBPs, thermal SNRs, Crab-like SNRs, and BH binaries . . .	120
7.2	HR vs. L_{obs} for the other sources in the SMC	121
7.3	HR vs. L_{obs} for all sources in the SMC	123
8.1	Spatial distribution of various classes of sources	129
8.2	Spatial distribution of HMXBs and young stars	130
A.1	Two color X-ray mosaic image of the SMC	134

List of Tables

3.1	Basic properties of GIS	19
3.2	Bit assignment for GIS	21
3.3	Temporal properties of GIS	22
3.4	Basic properties of SIS	24
3.5	Temporal properties of SIS	24
4.1	Observation fields of ASCA	28
5.1	Selected ASCA counterparts for ROSAT sources	38
5.2	ASCA sources detected in multiple observations	41
5.3	Final ASCA catalogue of X-ray sources in the SMC (source identification)	48
5.4	Final ASCA catalogue of X-ray sources in the SMC (names and comments)	52
5.5	Final ASCA catalogue of X-ray sources in the SMC (spectral parameters)	56
6.1	X-ray pulsars in the SMC	61
6.2	Spectral parameters for AX J0043–737	63
6.3	Spectral parameters for AX J0049–729	64
6.4	Spectral parameters for AX J0049–732	66
6.5	Spectral parameters for AX J0049.5–7323	67
6.6	Spectral parameters for AX J0051–733	68

6.7	Spectral parameters for AX J0051–722	71
6.8	Spectral parameters for AX J0051.6–7311	73
6.9	Spectral parameters for No. 43 (= RX J0052.1–7319?)	74
6.10	Spectral parameters for XTE J0054–720	75
6.11	Spectral parameters for 1WGA J0053.8–7226	76
6.12	Spectral parameters for SMC X-2	78
6.13	Spectral parameters for XTE J0055–724	80
6.14	Spectral parameters for AX J0057.4–7325	82
6.15	Spectral parameters for AX J0058–7203	83
6.16	Spectral parameters for RX J0059.2–7138	85
6.17	Spectral parameters for RX J0101.3–7211	86
6.18	Spectral parameters for 1SAX J0103.2–7209	87
6.19	Spectral parameters for AX J0105–722	90
6.20	Spectral parameters for XTE J0111.2–7317	91
6.21	Spectral parameters for SMC X-1	94
6.22	Minimum luminosities of XBPs	100
6.23	Spectral parameters for 0045–734, 0057–7226, and 0103–726	103
6.24	Plasma parameters for 0045–734, 0057–7226, and 0103–726	103
6.25	Spectral parameters for 0047–735	105
6.26	Spectral parameters for 0046–735	109
6.27	Spectral parameters for 0049–736	110
6.28	Spectral parameters for 0056–725	111
6.29	Spectral parameters for IKT1	112
6.30	Spectral parameters for AX J0048.2–7309	114

6.31	Spectral parameters for AX J0128.4–7329	115
7.1	Nonpulsating HMXBs and candidates in the SMC	118
8.1	Source populations in the SMC and in our Galaxy	126

Chapter 1

Introduction

Bright X-ray sources such as supernova remnants (SNRs) and binaries containing a neutron star (NS) or a black hole (BH) are “relics” of massive stars. Therefore, the number and spatial distribution of each class of X-ray source carry key information on the star forming activity, dynamics, and structure of the host galaxy. However, our knowledge of the populations of bright X-ray sources in our Galaxy is highly incomplete due to Galactic absorption in the low energy band, the large angular size that must be observed, and limited information on the distance of the relevant objects.

The Small Magellanic Cloud (SMC), a satellite of our Galaxy, is the next nearest neighbor after the Large Magellanic Cloud (LMC). The proximity (60 kpc is assumed in this paper; van den Bergh 2000), reasonable angular size ($\sim 3^\circ \times 3^\circ$), and low interstellar absorption in the direction of the SMC are all favorable for an unbiased survey of the X-ray source populations throughout the entire galaxy. Surveys of soft X-ray sources (below ~ 2 keV) have been carried out with the Einstein and ROSAT satellites. Haberl et al. (2000) presents the most complete catalogue, which contains 517 sources detected with ROSAT PSPC (Position Sensitive Proportional Counter). Sasaki, Haberl, & Pietsch (2000) used ROSAT HRI (High Resolution Imager) to determine the most accurate positions of 121 sources.

X-ray sources belonging to different classes have different properties in their spectra and temporal behaviour. X-rays from young SNRs are either due to a shock heated plasma (in shell-like SNRs) which preferentially emits soft (below ~ 2 keV) line dominated X-rays. Hard and featureless spectra are observed from Crab-like SNRs (due to release of the rotational energy of isolated NSs) and from some shell-like SNRs such as SN 1006 (due to

synchrotron emission from shock-accelerated electrons). Unlike SNRs, the other classes of X-ray sources emit time-variable X-rays. NSs with a low mass companion star (low mass X-ray binaries: LMXBs) have hard spectra and often exhibit X-ray bursts. BH binaries have bimodal behavior and show both high-soft and low-hard spectral states. NSs with a high mass stellar companion (high mass X-ray binaries: HMXBs) have even harder X-ray spectra and often exhibit long-term flux variations of a factor $\gtrsim 10$ –100. Many HMXBs also show coherent pulsations (X-ray binary pulsars: XBPs). Consequently, most bright X-ray sources emit copious hard X-rays (above ~ 2 keV). However, due mainly to a lack of imaging capability in the hard X-ray band, a systematic survey of the populations of hard X-ray sources had not previously been made. The Advanced Satellite for Cosmology and Astrophysics (ASCA: Tanaka, Inoue, & Holt 1994) is equipped with wide-band X-ray imaging instruments having a large field of view, and hence is optimized for an X-ray population study.

In this paper, we report the results from multiple observations of the SMC with ASCA. The whole SMC region including the main body and the eastern wing has been completely covered. A brief review of the SMC is given in chapter 2. The ASCA satellite and its equipment are described in chapter 3. Observation fields and the methods of data reduction are presented in chapter 4. In chapter 5, we describe the method of data analysis and present the results in catalogues. We give comments on specific sources in chapter 6. We show a source classification method using the spectral hardness ratio in chapter 7. In chapter 8, we combine our results with those of other studies to derive the source populations and the spatial distribution. Based on the results, we discuss the star forming activity of the SMC. Finally, we summarize this study in chapter 9.

Chapter 2

Review

— the Small Magellanic Cloud



Figure 2.1: Photograph of the southern hemisphere sky behind the 4-m telescope of the Cerro Tololo Inter-American Observatory. Diffuse light from three galaxies is seen in the upper left (SMC), lower left (LMC), and to the right (our Galaxy). (©Roger Smith, AURA, NOAO, NSF.)



Figure 2.2: Optical images of the LMC (left) and the SMC (right), where north is up and east is left. The “wing” is protruding out from the main body of the SMC to the east, connecting to the Magellanic Bridge. (©Anglo-Australian Observatory)

The Small and Large Magellanic Clouds (SMC and LMC) are conspicuous objects in the southern hemisphere sky, as seen in the photograph (figure 2.1). Magnified images of these clouds are shown in figure 2.2: both have a barred shape with dimensions of $\sim 2.5 \times 1^\circ$ (SMC) and $\sim 3^\circ \times 1^\circ$ (LMC).

These clouds have probably been known since ancient times, as seen in legends of many tribes of Australian Aboriginals. However, these people produced few documents which are still preserved. Therefore, it was the discovery by Ferdinand Magellan on his expedition in 1519 that brought the two clouds to the knowledge of people outside Australia. The clouds are thus named after Magellan.

In this chapter, we present a brief review of the Magellanic Clouds with particular emphasis on the SMC.

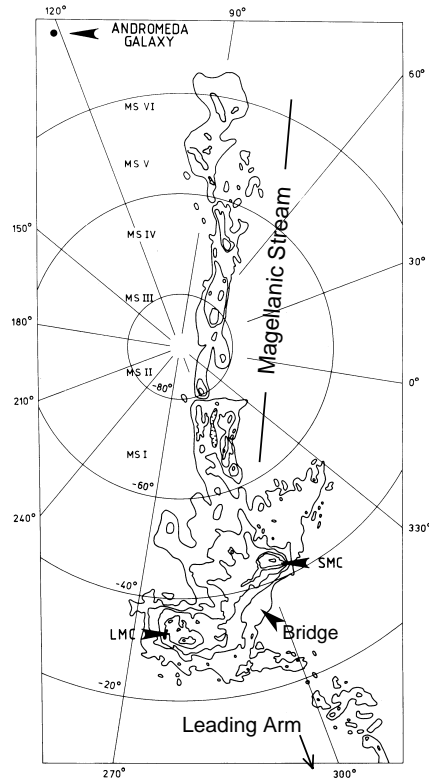


Figure 2.3: Global H I distribution in the Magellanic System, taken from Mathewson (1985). Coordinates are Galactic. The Leading Arm was discovered later (Putman et al. 1998).

2.1 The Magellanic System

The Magellanic Clouds, belonging to the local group¹, are the nearest satellite galaxies of our own. The total masses of the Magellanic Clouds are about $2 \times 10^9 M_{\odot}$ (SMC) and $2 \times 10^{10} M_{\odot}$ (LMC), which are about 1% and 10% of the mass of our Galaxy. The fraction of H I among the total mass is $\sim 30\%$ (SMC) and $< 8\%$ (LMC), both of which are larger than that of our Galaxy ($\sim 1\%$). This fact indicates that there still remains much material to produce stars, and thus the Magellanic Clouds are in a younger evolutionary phase than our Galaxy. This is also supposed from the metal-poor interstellar matter (ISM), with metal abundances of $\sim 20\%$ (SMC) and $\sim 30\%$ (LMC) of those in the solar vicinity (Russell & Dopita 1992).

¹Galaxies gravitationally bound to our Galaxy; 36 members are listed in van den Bergh (2000).

The H I distribution shown in figure 2.3 indicates a close connection between the Magellanic Clouds and our Galaxy. The Magellanic Clouds themselves are connected by the H I “Bridge” and surrounded by a common H I envelope. In addition, our Galaxy and the Magellanic Clouds are connected by two streams of H I gas, the Magellanic Stream (Mathewson, Cleary, & Murray 1974) and the Leading Arm (Putman et al. 1998). These structures are, as a whole, called the Magellanic System.

2.2 Interaction between the Magellanic Clouds and our Galaxy

There are many pieces of evidence indicating interactions between the Magellanic Clouds and our Galaxy. The existence of the eastern wing of the SMC, extending out in the direction of the LMC, and the H I Bridge is indicative of interactions between the two clouds. Stars in the Bridge and around the tip of the SMC wing were found to be as young as 10^8 yr, suggesting a common origin (Irwin, Demers, & Kunkel 1990). Vallenari et al. (1996) investigated the ages of stars outside the main body of the LMC and concluded that the stars on the western side (toward the Bridge) are the youngest ($2\text{--}3 \times 10^9$ yr) among their survey fields. The existence of young stars ($10^{8\text{--}9}$ yr) in and around the Bridge is a hint of tidal interactions which influenced star-forming activity (Vallenari et al. 1996). The Leading Arm and the Magellanic Stream indicate interactions between the clouds and our Galaxy. The former is leading the motion of the clouds while the latter is a trailing stream. The idea that both streams were torn from the clouds by tidal interactions is favored because the existence of both the leading and trailing stream is naturally expected in tidal interactions (Putman et al. 1998).

Many numerical simulations of the orbits of the clouds and our Galaxy have been performed to reproduce the Bridge and the Magellanic Stream via such tidal interactions (e.g. Murai & Fujimoto 1980; Gardiner, Sawa, & Fujimoto 1994; Gardiner & Noguchi 1996). Murai & Fujimoto (1980) showed that the Magellanic Clouds have been a binary galaxy system for a long time (~ 10 Gyr), which is consistent with the existence of the common H I envelope. They also showed that the Magellanic Stream was torn off from the SMC by tidal force and that the two clouds experienced a close encounter about 2×10^8 yr ago, which synchronizes with the ages of stars in the Bridge. Recently, two observational constraints have been obtained. One is the direct measurement of the proper motions of the SMC and

the LMC with the Hipparcos satellite (Kroupa & Bastian 1997). The proper motion in equatorial longitude and in equatorial latitude is $(1.23 \pm 0.84, -1.21 \pm 0.75)$ mas yr⁻¹ for the SMC and $(1.94 \pm 0.29, -0.14 \pm 0.36)$ mas yr⁻¹ for the LMC. The other constraint is the study of the age distribution of star clusters in the LMC by Girardi et al. (1995): the LMC experienced enhanced cluster formation about 2×10^9 yr and 1×10^8 yr ago. Turbulence of the interstellar matter triggered by two close encounters may have resulted in such bursts of cluster formation. Sawa, Fujimoto, & Kumai (1999) showed that some orbits with two close encounters 3×10^9 yr ago and 2×10^8 yr ago could reproduce the Magellanic Stream and were consistent with the Hipparcos measurement. It is open to question whether these orbits can explain other features of the Magellanic System, such as the Leading Arm.

2.3 Structure of the Small Magellanic Cloud

As seen from figure 2.2, most of the visible stars in the SMC are distributed along the northeast-southwest geometry (main body), and some are located in the eastern wing. Maragoudaki et al. (2001) carried out a wide-field ($6^\circ \times 6^\circ$) observation covering the SMC in the *U*, *V*, and *I* wavebands. They determined ages of the stars according to their color and magnitude, and derived spatial distributions of stars in seven ranges of ages (figure 2.4). They found that older stars show a rather regular distribution which is typical for a spheroidal body. On the other hand, the distribution of younger stars is highly asymmetric with a bent-barred shape (main body) and the eastern wing. The similar conclusions were drawn by Zaritsky et al. (2000) and Cioni, Habing, & Israel (2000) with observations in different wavebands. Therefore, the bar and wing of the SMC cannot originate solely from tidal effects; in other words, a scenario in which the bar and wing consist of stars extracted from the central SMC by tidal forces is rejected. Zaritsky et al. (2000) suggested that the origin of those shapes must be a relatively recent star formation triggered by a hydrodynamic interaction between gaseous components. The younger stars' distribution is qualitatively very similar to the H I distribution (figure 2.5). A large velocity gradient along the bar axis was found (Stanimirović et al. 1999), which might arise from a collision of two gaseous components along the bar.

The three-dimensional structure of the SMC can be derived by measuring distances to the member stars. Mathewson (1985) determined the distances to 161 Cepheids using the period-luminosity relation as shown in figure 2.6. The depth of the SMC was thus revealed

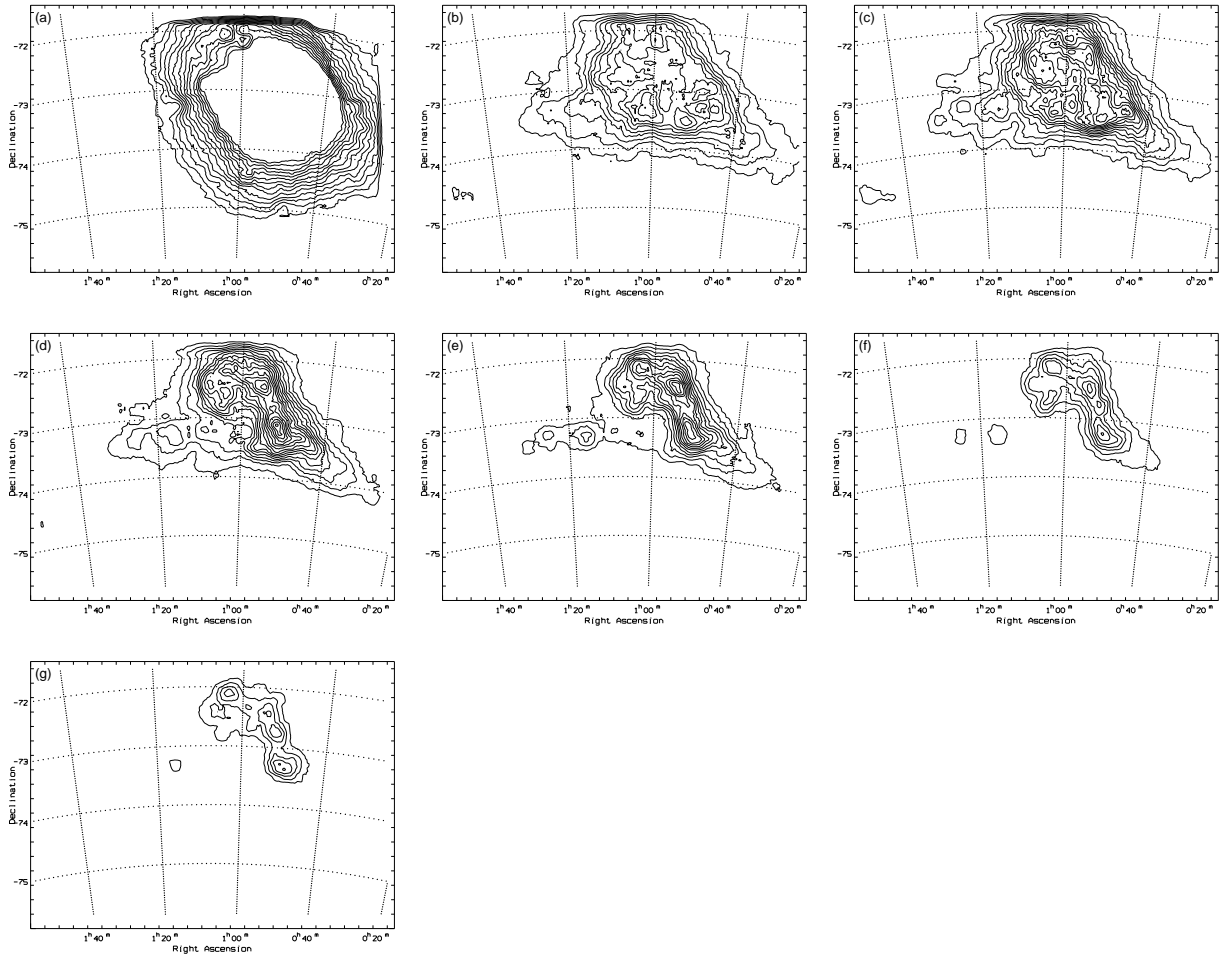


Figure 2.4: Isodensity contour maps of stars with different ages taken from Maragoudaki et al. (2001). Ranges of ages are (a) $> 2 \times 10^9$ yr, (b) $3.4\text{--}4 \times 10^8$ yr, (c) $1.7\text{--}3.4 \times 10^8$ yr, (d) $0.3\text{--}1.7 \times 10^8$ yr, (e) $1.2\text{--}3 \times 10^7$ yr, (f) $0.8\text{--}1.2 \times 10^7$ yr, and (g) $< 8 \times 10^6$ yr. The central region of (a) was masked because of the high concentration of stars. The coordinates are J2000.

to be 20–30 kpc, which is much larger than the projected size of the SMC (i.e., the SMC has a large inclination angle).

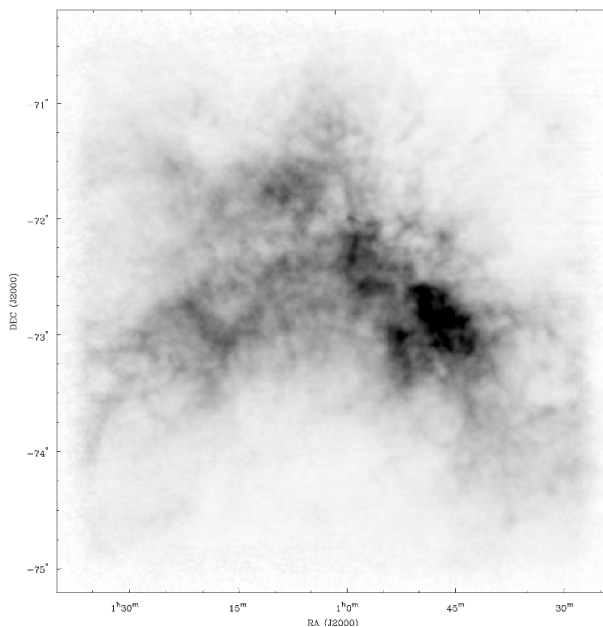


Figure 2.5: H I column density image of the SMC taken from Stanimirović et al. (1999).

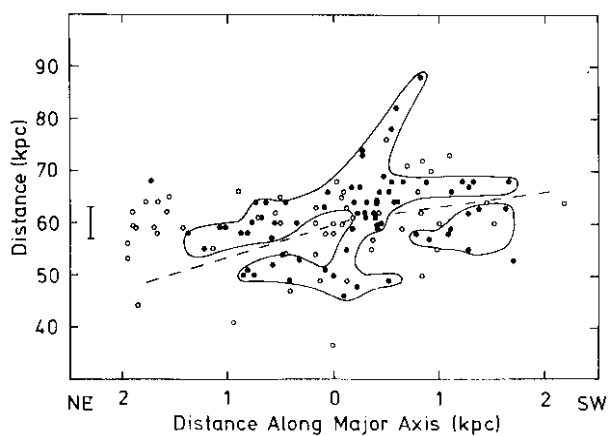


Figure 2.6: Distances to 161 Cepheids in the SMC plotted against their projected distances along the major axis of the SMC (taken from Mathewson, 1985). The filled/open circles represent Cepheids with periods longer/shorter than 10 days (or younger/older than 5×10^7 yr). The solid lines envelop the younger Cepheids. The dashed line demarcates the low velocity H I gas component (near) and high velocity component (far).

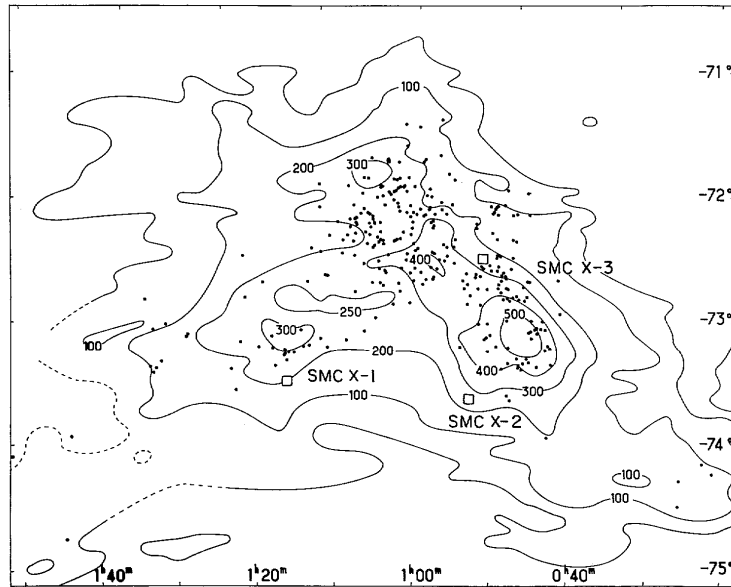


Figure 2.7: X-ray view of the SMC in late 1970's taken from Clark et al. (1978). The positions of the three X-ray sources SMC X-1, SMC X-2 and SMC X-3 are shown by squares. The equatorial coordinates (1950B) are presented. Contours and dots represent the surface brightness of the 21-cm radio emission and the positions of O-B2 stars, respectively.

2.4 Previous High Energy Observations

2.4.1 X-ray surveys

Searches for X-rays from the Magellanic Clouds have been carried out since the very beginning of the X-ray astronomy. The first attempt to detect X-rays from the SMC was made with proportional counters and scintillation counters which were launched in 1970 by a Thor missile. In a scan observation with these instruments, the first X-ray source in the SMC, known as SMC X-1 today, was discovered (Price et al. 1971). The position was subsequently localized with an error box of $\sim 7' \times 2'$ by the Uhuru satellite (Giacconi et al. 1972). X-ray pulsations with a 0.716 s period from SMC X-1 were discovered by Lucke et al. (1976). Clark et al. (1978) discovered two new transient sources, SMC X-2 and SMC X-3, with the SAS-3 satellite, which had a $12^\circ \times 12^\circ$ field of view and thus covered the whole area of the SMC. These sources are all considered to be HMXBs today. In that era, the X-ray view of the SMC was rather sparse as shown in figure 2.7.

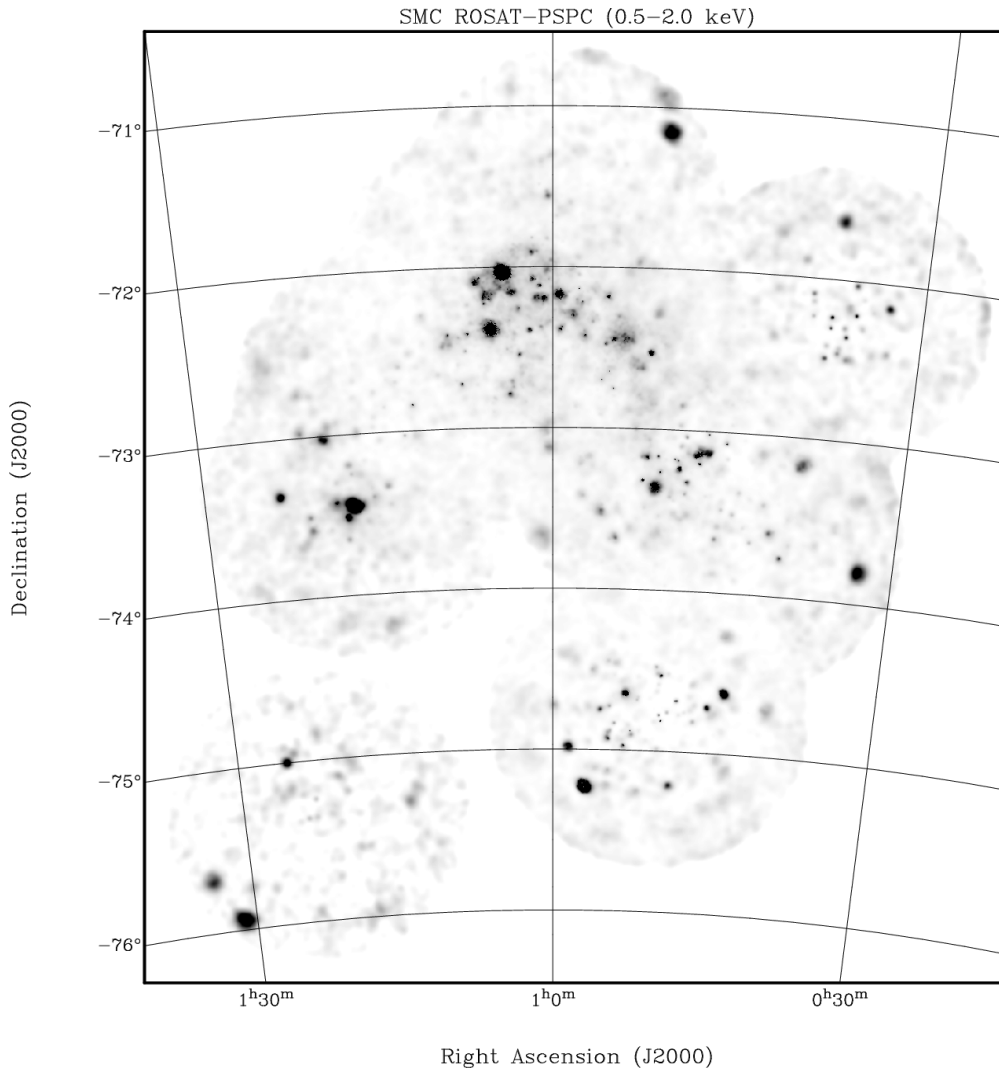


Figure 2.8: X-ray mosaic image of the SMC obtained with ROSAT PSPC, taken from Haberl et al. (2000). The equatorial coordinates (J2000) are overlaid.

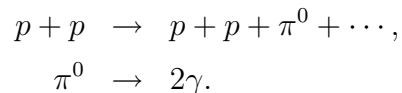
The Einstein satellite, which was sensitive to soft X-rays (below a few keV) and had a nice imaging capability, discovered a number of sources in the SMC. Wang & Wu (1992) carried out a comprehensive analysis of the Einstein data of the SMC and detected 70 sources. Some of these sources were identified with radio SNRs, H II regions, HMXBs, background AGNs, and foreground stars, while over half were left unidentified.

The ROSAT satellite greatly enhanced the number of X-ray sources in the SMC. Haberl

et al. (2000) analyzed the data from 31 ROSAT PSPC observations which cover the whole area of the SMC, and catalogued 517 discrete sources. The mosaic image (figure 2.8) indicates that many sources are concentrated in the main body and the eastern wing. A smaller area was also covered by 71 ROSAT HRI observations. Sasaki, Haberl, & Pietsch (2000) used those data and catalogued 121 sources with a good positional accuracy of $\sim 1''$ – $10''$. Cowley et al. (1997) and Schmidtke et al. (1999) found five Be/X-ray binaries based on the positional coincidence of the ROSAT HRI sources with Be stars. Haberl & Sasaki (2000) found that many of the known Be/X-ray binaries have an H α emission line object (Meyssonnier & Azzopardi 1993) as a counterpart. This fact indicates that X-ray sources correlated with an emission line object are candidates for Be/X-ray binaries. Thus they made a cross-correlation of the 517 ROSAT PSPC sources and a few other sources with the catalogue of Meyssonnier & Azzopardi (1993) and found ~ 30 new candidates for Be/X-ray binaries. X-ray binaries were also identified from the flux variability of the ROSAT sources (Kahabka & Pietsch 1996). Supersoft X-ray sources (SSSs) have a very soft spectrum with a blackbody temperature of 15–80 eV (Kahabka & van den Heuvel 1997); thus, interstellar absorption severely reduces the flux of SSSs. Therefore, the Magellanic Clouds, which are located at high Galactic latitude are suitable sites for studies of SSSs. Five SSSs were discovered in the SMC, whose spectral and temporal properties are presented by Kahabka, Pietsch, & Hasinger (1994).

2.4.2 GeV and TeV γ -ray observations

GeV γ -ray observations were carried out with CGRO EGRET (Sreekumar et al. 1993). The result was negative, giving an upper limit of 0.5×10^{-7} photon $\text{cm}^{-2} \text{s}^{-1}$ in the > 100 MeV range. GeV γ -rays are produced via the interaction between cosmic ray nucleons and the interstellar matter as follows:



Sreekumar & Fichtel (1991) calculated the γ -ray emission from the SMC based on the H I measurement, non-thermal (synchrotron) radio observations and assumptions of the dynamical state. They derived the cosmic ray density from the radio data, and then calculated the γ -ray emission via the interaction between cosmic rays and the H I interstellar matter. The flux above 100 MeV thus derived was $\sim 10^{-8}$ photon $\text{cm}^{-2} \text{s}^{-1}$. This is consistent

with the EGRET result (flux $< 0.5 \times 10^{-7}$ photon $\text{cm}^{-2} \text{s}^{-1}$). The amount of cosmic rays per unit mass of the interstellar matter was found to be several times smaller than that in our Galaxy. Sreekumar & Fichtel (1991) concluded that this could be attributed to the dynamical state of the SMC: the interstellar matter in the SMC is not dynamically stable and rather leaky for cosmic rays.

TeV γ -ray observations of the SMC were carried out with a Cerencov telescope (Allen et al. 1993). The intensity of γ -rays in the direction of SMC X-1 showed positive excess, although it was not statistically significant. They gave upper limits of γ -ray flux above 30 TeV from SMC X-1 and the whole SMC as 2.6×10^{-13} photon $\text{cm}^{-2} \text{s}^{-1}$ and 19.3×10^{-13} photon $\text{cm}^{-2} \text{s}^{-1} \text{msr}^{-1}$, respectively.

Chapter 3

Instruments

3.1 Overview of the ASCA Satellite

ASCA (Advanced Satellite for Cosmology and Astrophysics: Tanaka, Inoue, & Holt 1994) was the 4th Japanese satellite for X-ray astronomy, and was launched on Feb. 20, 1993. After operating for eight years, ASCA re-entered the atmosphere on March 2, 2001¹.

ASCA had four X-ray telescopes (XRTs, Serlemitsos et al. 1995) and four instruments at the focal planes: two Gas Imaging Spectrometers (GISs, Ohashi et al. 1996) and two Solidstate Imaging Spectrometers (SISs, Burke et al. 1994). This equipment made it possible to simultaneously obtain X-ray images and spectra in the 0.5–10.0 keV band.

3.2 XRT: X-ray Telescope

X-rays can be totally reflected if their incident angle is smaller than a critical value on the order of $\sim 1^\circ$. The critical value is smaller for higher energy X-rays. Mirrors of X-ray telescopes which utilize this mechanism are usually placed in a Wolter type-I configuration: a combination of parabolic and hyperbolic shells. Incident X-rays are reflected in series by each of the shells, and focused on the focal plane (see figure 3.2). The effective area can be increased by nesting the shells so that they have a common focus. The previous X-ray

¹Surprisingly, this is just one day after Prof. Minoru Oda passed away.

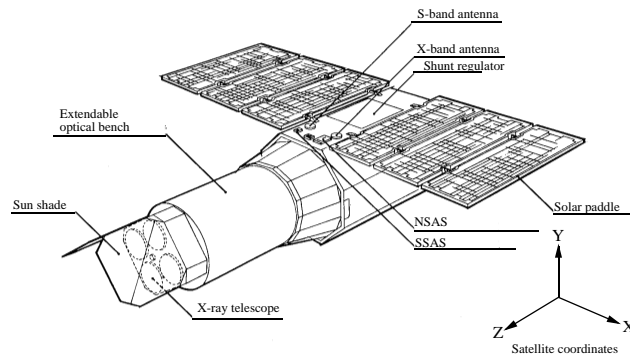


Figure 3.1: Schematic view of ASCA in orbit.

satellites Einstein and ROSAT had this type of X-ray mirror configuration and provided high resolution images up to a few keV.

However, since this type of mirror is heavy, a telescope with a large effective area cannot be launched. Therefore an approximation of the Wolter type-I configuration, which consists of two conical foils, was adopted for the XRTs of ASCA. To get a large effective area for higher energy X-rays, the incident angle of each foil must be smaller, which results in a smaller projected area. Nesting a large number of foils compensates for this. According to this concept, each foil of the ASCA XRTs was made thin ($125 \mu\text{m}$) and 120 such foils were nested in a coaxial configuration into one quadrant. As a result, the field of view (FOV) is $18' - 24'$ (FWHM) and the effective area of each XRT is $\sim 300 \text{ cm}^2$ below 2 keV and $\sim 50 \text{ cm}^2$ at 10 keV. The sum of the effective areas of the four XRTs is about 5 times larger than that of Einstein, or 2 times larger than that of ROSAT, at $\sim 1 \text{ keV}$. Plots of the effective area of a single XRT vs. incident X-ray energy and off-axis angle are shown in figure 3.3 and figure 3.4, respectively.

However, utilizing an approximation of the Wolter type-I configuration and very thin foils resulted in a poorer focusing ability. Figure 3.5 shows the point spread function (PSF) at several incident positions. The apparent butterfly-like structure is due to the junctions between the four quadrants of each XRT. The half power diameter (HPD) is $\sim 3'$, and 80% of the incident energy is encircled in a $6'$ diameter for an on-axis source. Two point sources can be distinguished if the separation is over $\sim 30''$.

Stray light (photons from outside of the FOV) is another weak point of the ASCA XRTs. It is caused by irregular manners of reflection, such as a single reflection or more than three

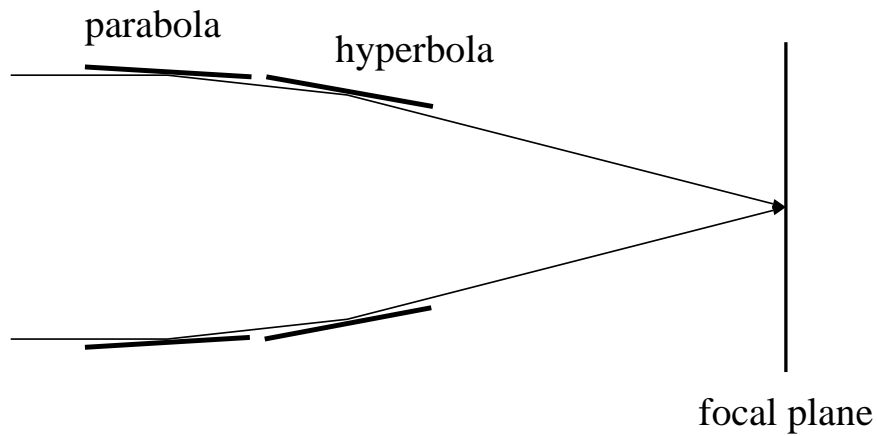


Figure 3.2: Mechanism of an X-ray telescope which utilizes Wolter type-I optics.

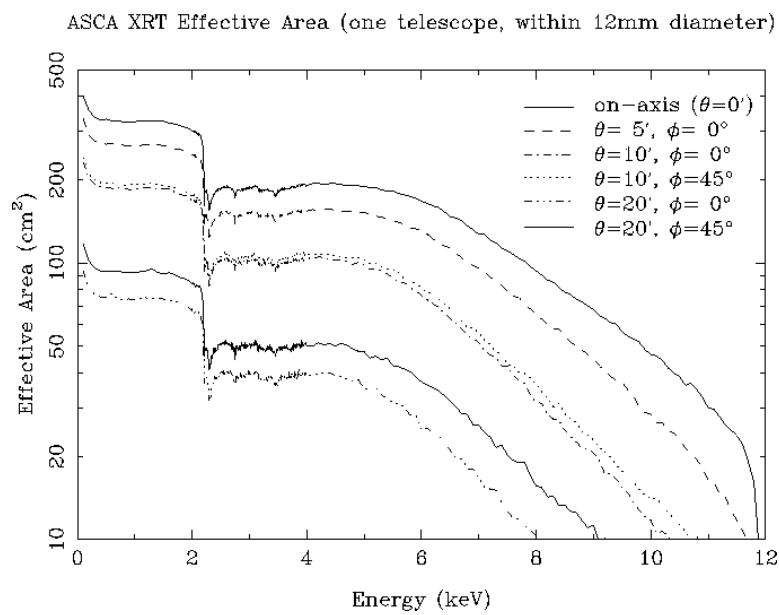


Figure 3.3: Effective area of a single XRT as a function of the energy of the incident X-ray. Dependence on the off-axis angle θ and azimuthal angle ϕ is also shown.

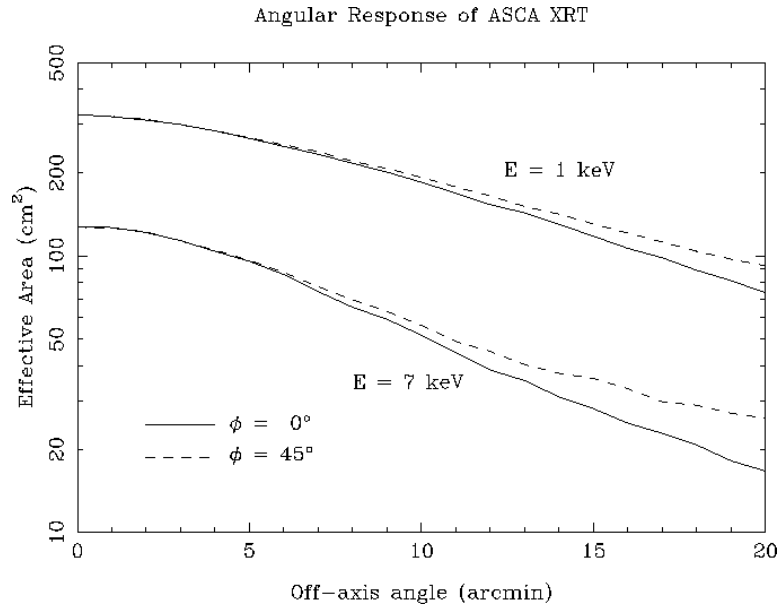


Figure 3.4: Effective area of a single XRT as a function of the off-axis angle. The data for incident X-rays of 1.0 and 7.0 keV are shown.

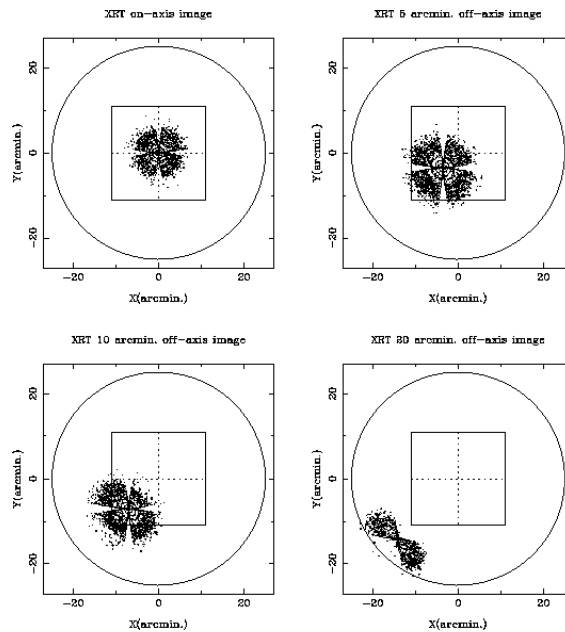


Figure 3.5: Point spread function of the ASCA XRT.

reflections, or reflections at the back side of the foils. Figure 3.6 shows a GIS image of stray light from the Crab nebula, which is located 1° away from the center of the GIS.

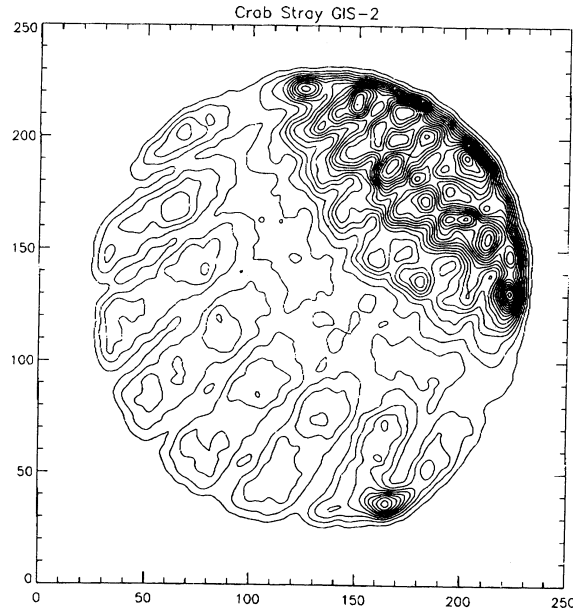


Figure 3.6: Stray light image obtained with GIS2. The Crab nebula is 1° from the center of the GIS.

3.3 GIS: Gas Imaging Spectrometer

GISs (GIS2 and GIS3) are gas scintillation proportional counters which are placed on the focal planes of XRTs. Compared to SIS, the characteristics of GIS are a larger FOV, higher sensitivity in the hard X-ray band, and better timing resolution (see table 3.1 for basic properties of GIS).

Figure 3.7 shows the operating mechanism of GIS. An incident X-ray photon is detected by a gas mixture of Xe (96%) and He (4%), and a cloud of photo electrons is produced in the drift region. The cloud is made to drift by a weak electric field and enters the scintillation region. It is then accelerated by a strong electric field there, but the Xe atoms

Table 3.1: Basic properties of GIS.

Size of one pixel	0.5 mm ($\simeq 0'.5$)
FOV (diameter)	50'
Energy band	0.7–10.0 keV
Energy resolution	8% at 5.9 keV (FWHM)
Timing resolution	62.5 ms for usual PH mode

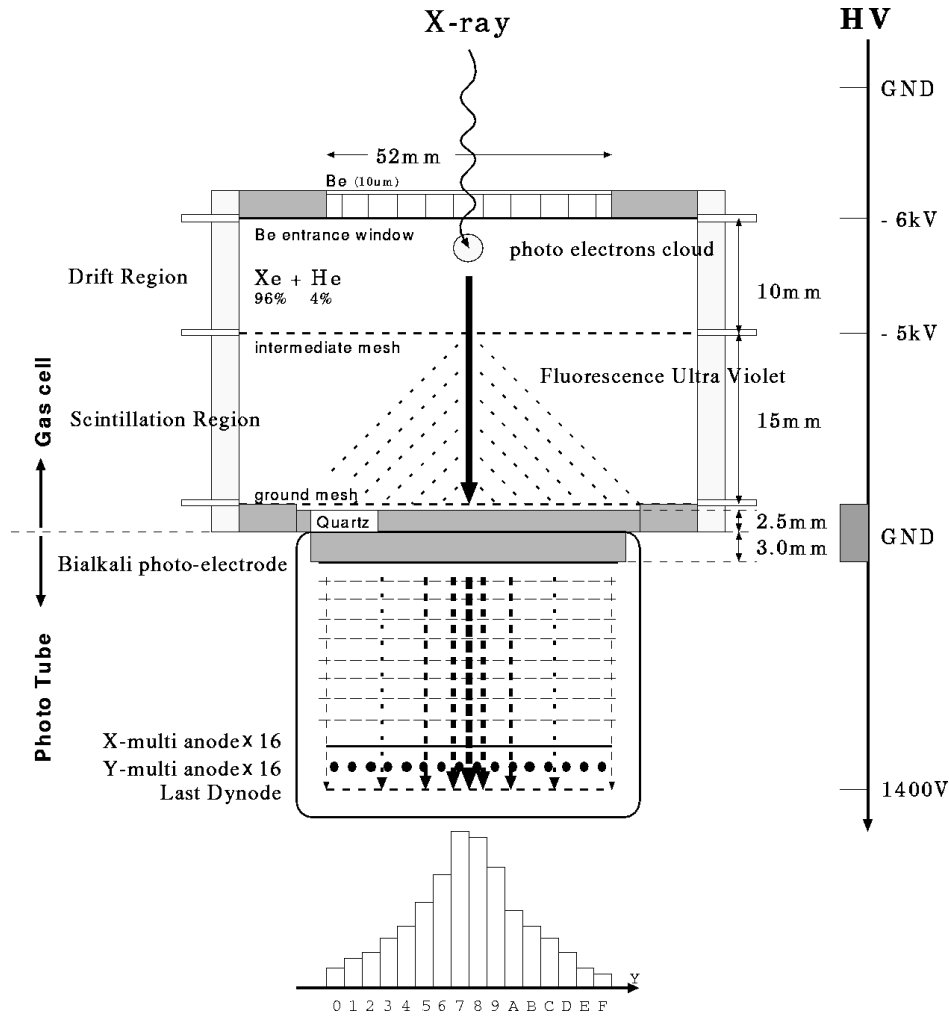


Figure 3.7: Schematic view of the operating mechanism of GIS.

are not ionized as in a gas proportional counter. Instead, they are excited by electrons with sufficient energy, and when they de-excite, UV photons are emitted. Therefore the number of UV photons is proportional to the number of electrons in the cloud, hence to the energy of the incident photon. Finally the UV photons are detected by an imaging phototube. The energy resolution is proportional to $E^{-0.5}$ (here E is the incident X-ray energy) and is $\sim 8\%$ (FWHM) at 5.9keV. The effective area of a single GIS combined with an XRT is shown in figure 3.8.

GIS has two observation modes: pulse height (PH) mode and multi-channel pulse count (MPC) mode. Normally PH mode is used. In this mode, 31 bits are assigned to the pulse height (PH), X position (RAWX), Y position (RAWY), rise-time (RT), spread of UV photons

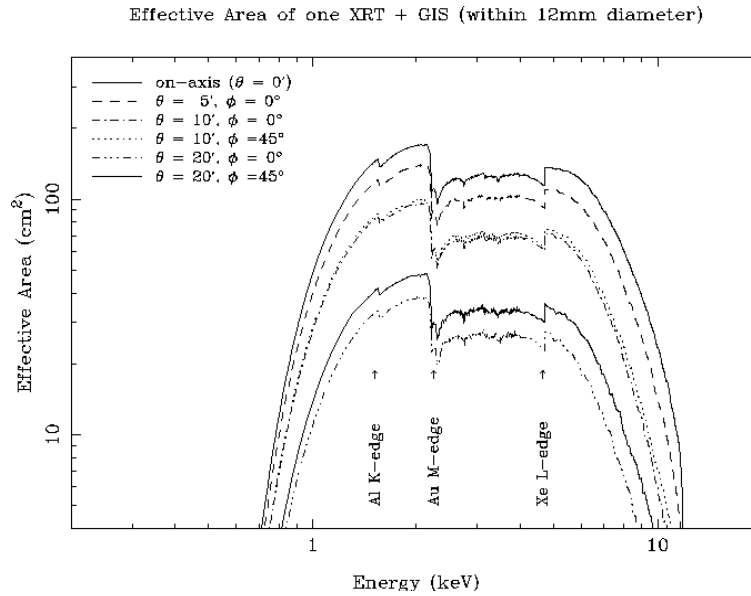


Figure 3.8: Dependence of the effective area of a single GIS combined with an XRT. Dependence on the off-axis angle θ and azimuthal angle ϕ is also shown.

Table 3.2: Freedom of bit assignment for PH mode of GIS.

	Possible number of bits assigned
PH	6, 8, 10*
RAWX	6, 8*
RAWY	6, 8*
RT	0, 5*, 6, 8
SP	0*, 8
Timing bit	0*–10
Total	31

*: Default assignments.

(SP) and event time (“timing bit”); usually 10, 8, 8, 5, 0, and 0 bits, respectively. We can adjust the bit assignment within a limited degree of freedom as shown in table 3.2. MPC mode, which has been rarely used, is for bright sources. In this mode, positional information is not recorded. The timing resolution and maximum source intensity for various recording rates are summarized in table 3.3. The gain is always monitored with a radio isotope ^{55}Fe attached to each GIS, which emits monochromatic X-rays with an energy of 5.89 keV.

Table 3.3: Timing resolution and maximum source intensity of GIS.

Mode	Bit rate	Timing resolution (sec)	Maximum source intensity
PH	H	0.0625*	256 count/sec
	M	0.5*	32 count/sec
	L	2.0*	8 count/sec
MPC	H	0.5	128 Crab [†]
	M	4.0	16 Crab [†]
	L	16.0	4 Crab [†]

[†]: 1 Crab corresponds to ~ 1000 count/sec.

*: For the case when the timing bit is 0.

3.4 SIS: Solidstate Imaging Spectrometer

SISs (SIS0 and SIS1) are the first CCD cameras used for X-ray astronomy. As shown in figure 3.9, each SIS consists of four chips, called S0C0 (chip0 of SIS0), S0C1 (chip1 of SIS0), and so on to S1C3 (chip3 of SIS1). Compared to GIS, the characteristics of SIS are a higher energy resolution, higher sensitivity in the soft X-ray band, and better position resolution. The basic properties of SIS are given in table 3.4. The effective area of a single SIS combined with an XRT is shown in figure 3.10.

SIS has three observation modes: Faint, Bright and Fast mode. In the Faint mode, positional information of the center pixel² and the pulse-height of each 9 (3×3) pixels surrounding the center pixel are recorded as one event. In the Bright mode, each event is classified into eight grades (grades 0–7, see figure 3.11). The pulse heights are summed up according to the determined grade. The sum of the pulse heights, the positional information of the center pixel, and the grade are then recorded as one event. Events of grade 0, 2, 3 and 4 are usually regarded as X-ray events. In these two modes, we can use 1, 2 or 4 chips of each SIS according to the scientific goal of the observation³. The timing resolution is determined by the time necessary to read out all the chips being used: 4 s per chip (see table 3.5). The Fast mode is for very bright sources and is operated using only one chip of

²The center pixel is the pixel where the pulse-height distribution is a maximum among the surrounding 3×3 pixels.

³We use the terms like “1-CCD Faint mode” or “4-CCD Bright mode.”

Figure 3.9: SIS chip configuration.

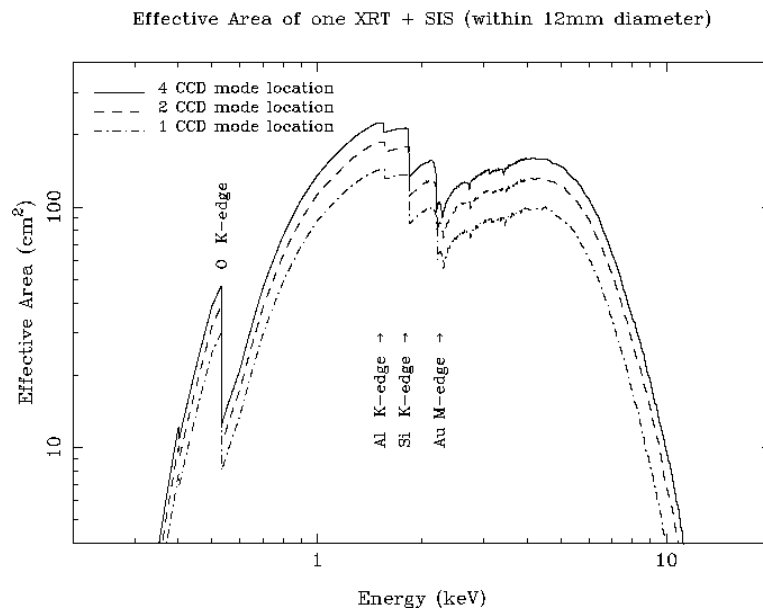


Figure 3.10: Dependence on energy of the effective area of a single SIS combined with an XRT. Dependence on the source locations is also shown.

Table 3.4: Basic properties of SIS.

Size of one pixel	0.027 mm ($\simeq 0'027$)
FOV	$11' \times 11'$ per one chip
Energy band	0.5–10.0 keV
Energy resolution	2% at 5.9 keV (FWHM)
Timing resolution	4/8/16 s for 1/2/4-CCD mode

Table 3.5: Timing resolution and maximum source intensity of SIS.

Mode	Bit rate	Timing resolution (sec)	Maximum source intensity (count/sec)
Faint	H	4/8/16*	128
	M	4/8/16*	16
	L	4/8/16*	4
Bright	H	4/8/16*	512
	M	4/8/16*	64
	L	4/8/16*	16
Fast	H	0.016	1024
	M	0.016	128
	L	0.016	32

*: For 1/2/4-CCD modes, respectively.

each SIS. In this mode, a better timing resolution of 16 ms is obtained at the expense of positional information.

The correction sequence of pixel dark levels is as follows. In orbit, the dark level averaged over each 16×16 pixels (“dark frame”) is estimated by the onboard CPU and subtracted from the PH of each pixel. The Dark Frame Error (DFE) is the difference between the real average dark level and the dark frame. On the ground, the DFE averaged over the whole chip is estimated using the PH values of the corner pixels⁴, and is subtracted again.

Only the “average” dark level is taken into account in these correction methods. Therefore, a difference between the dark level of each pixel and the DFE-corrected PH value still exists. This is called Residual Dark Distribution (RDD). RDD is corrected by the RDD

⁴Corner pixels are the pixels on the corners of each array of 3×3 pixels around the center pixel.

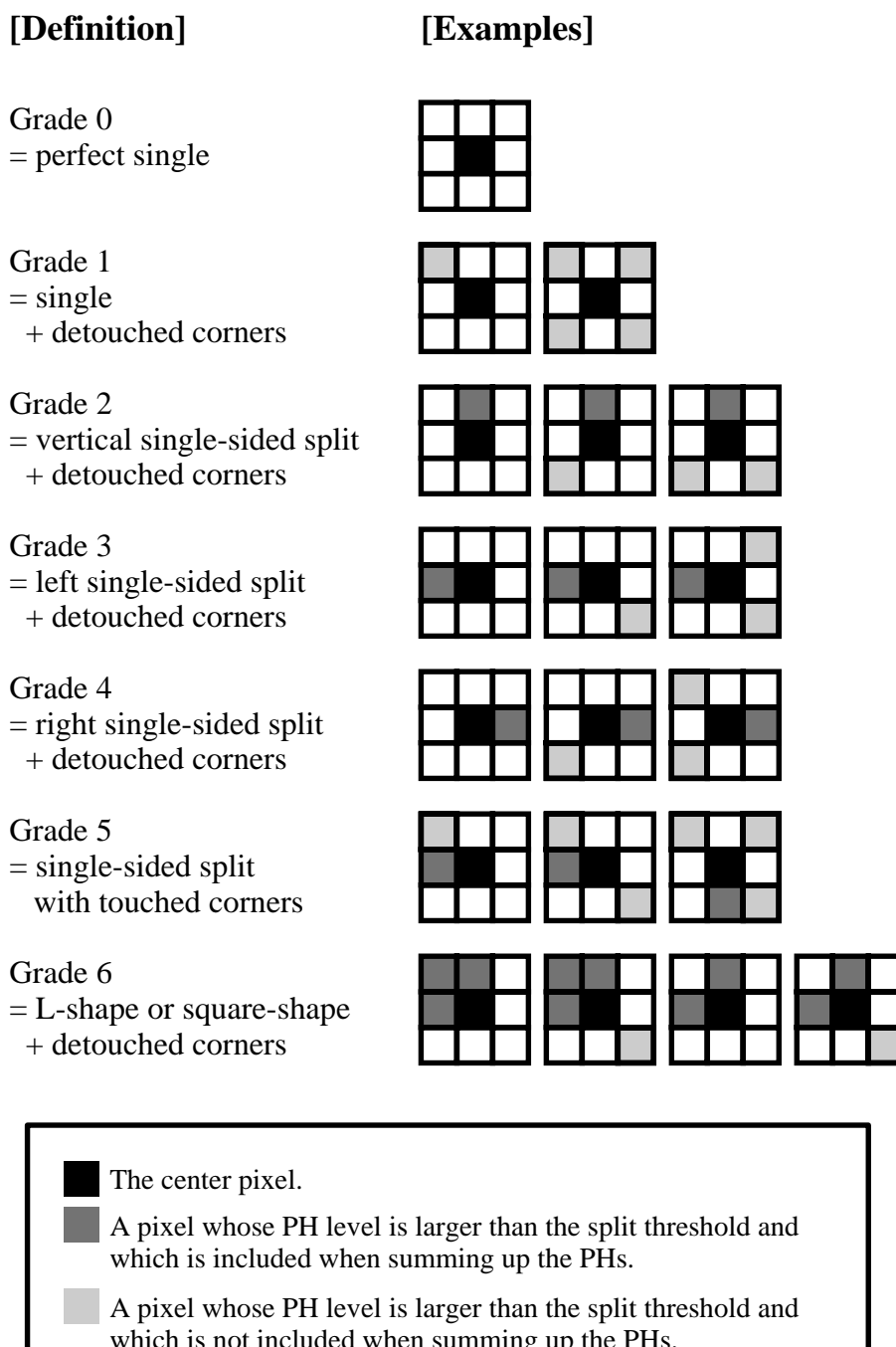


Figure 3.11: Grade definitions (0–6) for one event of SIS. All the other patterns are classified as grade 7.

map, which contains information on the dark level of each pixel.

Pixels damaged by charged particles show various values of dark currents, according to the degree of damage. This fact is the main cause of RDD. Therefore, data taken in 4-CCD mode are more affected than data taken in 2/1-CCD mode because of the longer exposure time. In addition, later observations are more affected than earlier ones because the degree of damage gradually increases from the time of the launch.

Chapter 4

Observations and Data Reduction

4.1 Observation Fields

ASCA had observed the SMC region 22 times by the end of the mission, as summarized in table 4.1. Although the observations made before 1999 had aimed at specific objects such as SNRs, X-ray pulsars, and a supersoft X-ray source, the assembly of these observations had already covered most of the main body and the eastern wing of the SMC. In order to cover all the blank area, the survey project (SMC 1–10 in table 4.1) including long exposure observations (SMC SW N1 and N2 in table 4.1) were performed. These observations have covered most of the SMC region as shown in figure 4.1. In this study, we used all of these observation data and carried out various analyses in a coherent manner.

4.2 Data Reduction

In each observation, X-ray photons were collected with four XRTs and detected separately with two GISs and two SISs. We rejected any data obtained in the South Atlantic Anomaly, or when the cut-off rigidity was lower than 4 GV, or when the elevation angle was lower than 5° . Particle events in the GIS data were removed by a rise-time discrimination method. SIS data obtained when the elevation angle from the bright earth was lower than 25° , or with hot and/or flickering pixels, were also rejected. The effects of RDD (Residual Dark Distribution) on the SIS data were corrected with the method given in Dotani et al. (1997)

Table 4.1: SMC fields observed with ASCA.

ID	Observation Date (UT)		Target Name	Pointed Direction (J2000)		Expos. (ksec) GIS/SIS
	Start	End		R.A.	Dec.	
A	1993/04/26 22:23	04/27 23:41	SMC X-1	1 ^h 17 ^m 04 ^s	-73°26'34"	4/—
B	1993/05/12 08:01	05/13 12:26	E0102-72.2	1 ^h 04 ^m 02 ^s	-72°01'55"	35/31*
C	1995/10/18 18:32	10/19 21:31	SMC X-1	1 ^h 17 ^m 04 ^s	-73°26'35"	41/—
D	1996/05/21 02:25	05/23 06:31	0103-72.6	1 ^h 04 ^m 52 ^s	-72°23'11"	78/61*
E	1997/05/21 13:01	05/22 01:31	1E 0035.4-7230	0 ^h 37 ^m 20 ^s	-72°14'14"	23/—
F	1997/11/13 03:58	11/14 06:51	N19	0 ^h 47 ^m 16 ^s	-73°08'30"	43/38†
G	1997/11/14 06:51	11/15 08:22	N66	0 ^h 59 ^m 25 ^s	-72°10'12"	39/34†
H	1997/12/12 11:05	12/12 23:55	SMC X-3	0 ^h 52 ^m 06 ^s	-72°26'06"	20/—
I	1998/11/18 17:37	11/19 15:11	XTE J0111.2-7317	1 ^h 11 ^m 26 ^s	-73°25'07"	26/—
J	1998/11/24 09:39	11/25 10:51	SMC Center	0 ^h 56 ^m 05 ^s	-72°52'12"	27‡/—
K	1999/05/10 10:31	05/11 14:00	SMC 1	0 ^h 42 ^m 06 ^s	-73°43'53"	40/—
L	1999/05/11 13:59	05/12 16:46	SMC 2	0 ^h 54 ^m 44 ^s	-73°30'00"	32/—
M	1999/05/12 23:11	05/14 00:35	SMC 3	1 ^h 03 ^m 33 ^s	-73°00'00"	30/—
N	1999/05/14 00:35	05/15 01:56	SMC 4	1 ^h 12 ^m 08 ^s	-72°47'47"	41/—
O	1999/05/28 13:24	05/29 15:11	SMC 5	1 ^h 28 ^m 36 ^s	-73°30'03"	29‡/—
P	2000/04/04 00:09	04/07 01:30	SMC SW N1	0 ^h 42 ^m 35 ^s	-73°40'30"	93/—
Q	2000/04/11 18:50	04/17 12:11	SMC SW N2	0 ^h 47 ^m 30 ^s	-73°09'13"	177/96†
R	2000/04/25 12:09	04/26 14:21	SMC 9	0 ^h 58 ^m 20 ^s	-73°35'00"	27/—
S	2000/04/26 14:20	04/27 16:40	SMC 6	0 ^h 33 ^m 00 ^s	-73°45'00"	45/—
T	2000/04/27 16:40	04/28 19:01	SMC 7	0 ^h 53 ^m 30 ^s	-71°54'00"	44/—
U	2000/04/28 19:01	04/29 21:31	SMC 8	1 ^h 00 ^m 00 ^s	-71°20'00"	45/—
V	2000/04/29 21:30	05/01 00:01	SMC 10	1 ^h 20 ^m 00 ^s	-72°50'00"	38/—

†: SIS was operated in 1-CCD mode () or 2-CCD mode (†).

‡: In these observations, GIS was operated with a special bit assignment of 8-6-6-5-6 (J) or 8-8-8-5-2 (O), in which the time resolution was increased by a factor of 64 (J) or 4 (O), at the sacrifice of a reduction of energy resolution by a factor of 4 (J and O) a reduction of spatial resolution by a factor of 4 (J).

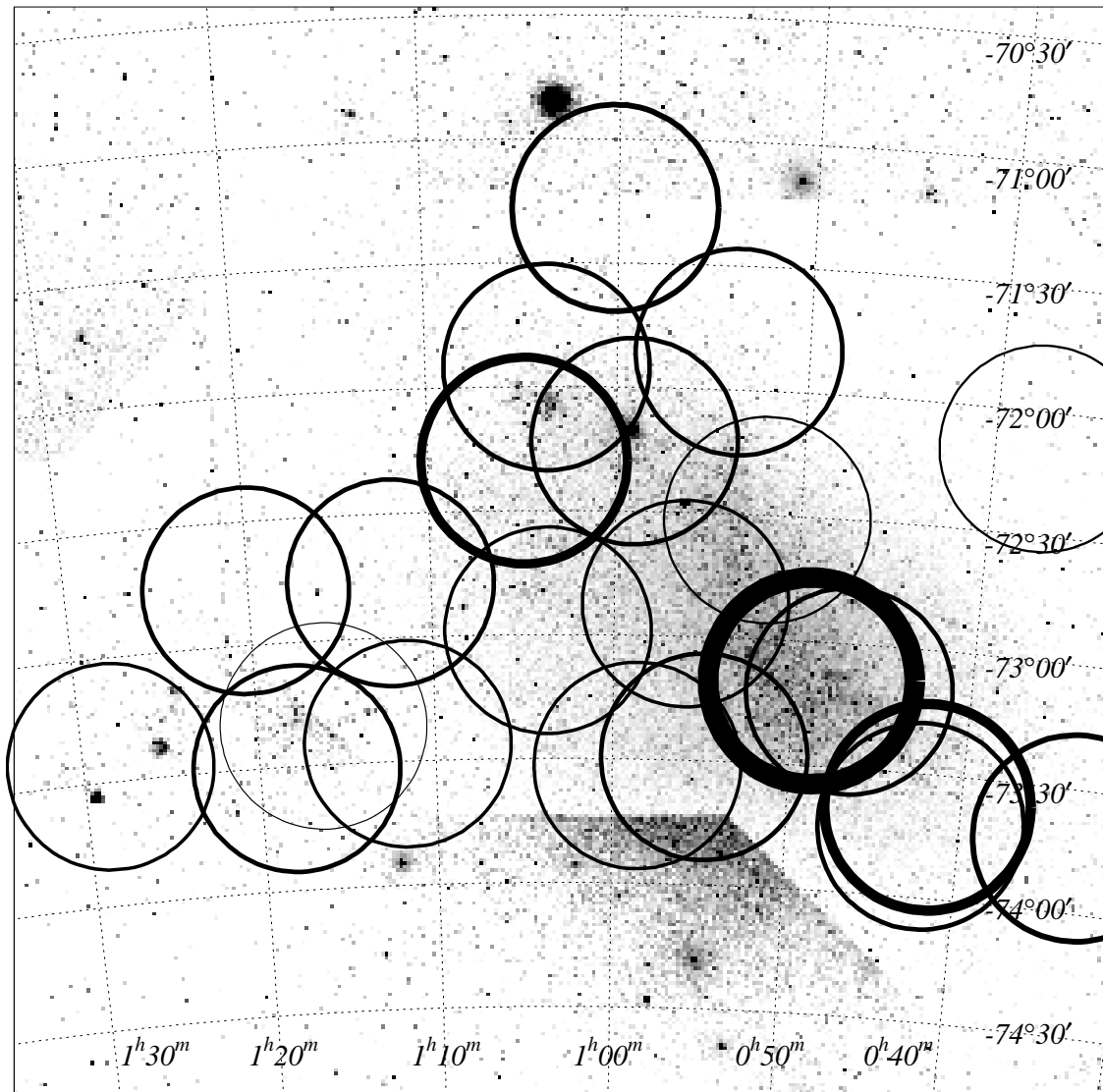


Figure 4.1: All observation fields with ASCA GIS superimposed on the optical image of the SMC region from the Digitized Sky Survey (DSS). Equatorial coordinates with an equinox of 2000 are also shown. Each observation field is represented by a $\sim 50'$ -diameter circle, the thickness of which is proportional to the exposure time. The discontinuity seen in the DSS image is an artifact.

for observations carried out later than 1996. After the screening, the total available exposure time for two GISs was ~ 2000 ks.

In order to study X-ray source populations in a coherent manner, the GIS is more suitable than the SIS because of its larger field of view, larger effective area at high energy, and better time resolution. Therefore, we mainly used the GIS data in this study, while the SIS data were used for peculiar objects which need a fine energy resolution and/or a better spatial resolution.

Chapter 5

Systematic Analyses on Discrete Sources

5.1 X-Ray Images

5.1.1 Images in the sky/detector coordinate systems

Images in each observation were constructed in the sky and detector coordinate systems (hereafter “sky images” and “detector images”, respectively), with the XSELECT package. In a detector image, the positions of photons are recorded using the coordinates peculiar to the detector, and are converted to sky coordinates via the average attitude of the satellite during the observation. In a sky image, on the other hand, the position of each photon is determined based on the satellite attitude at the incident time of the photon. Therefore, a strong advantage of sky images is that blurring of the image due to attitude fluctuation is corrected. On the other hand, the advantage of a detector image (only for the GIS) is its larger FOV with a radius of $\sim 25'$, compared to $\sim 20'$ for a sky image.

We thus used sky images for sources within the central $\sim 20'$ radius of the GIS (hereafter “inner circle”) and detector images for the concentric region of $\sim 20'$ – $25'$ (hereafter “outer ring”). Although the outer ring region suffers higher background, larger calibration uncertainty, and larger distortion of the PSF than the inner circle region, it was still useful for studies of source populations which need a large FOV. For SIS analyses, we always used sky images.

5.1.2 Source extraction

For each observation, X-ray sources were identified from images in the soft (0.7–2.0 keV), hard (2.0–7.0 keV), and total (0.7–7.0 keV) bands. We smoothed the images with a Gaussian filter ($\sigma = 30''$), and examined the significance of each local peak. Photons were extracted from a circle of $3'$ radius centered on the peak, in which 90% of incident photons were contained (Serlemitsos et al. 1995), or from an ellipse at larger off-axis angles because of the distortion of the PSF. In several cases, a smaller circle/ellipse was used to avoid contamination from nearby peaks. For obs. J, a larger circle was used, because in this observation the spatial resolution was reduced by a factor of 4 and thus the images were blurred. These photon events were also used in the subsequent analyses described in the following sections. Background regions were selected from the sky near each peak. We then derived the S/N ratio defined as

$$\frac{S}{N} \equiv \frac{n(P) - n(B)}{\sqrt{n(B)}}, \quad (5.1)$$

where $n(P)$ and $n(B)$ represent the photon counts in the circle/ellipse at the peak and in the background region, respectively. The local peak was identified as an X-ray source if the S/N ratio exceeded 5 in at least one of the soft-, hard-, or total-band images. Several sources were detected in multiple observations as described in section 5.2.2. In all, 106 sources were detected as catalogued in tables 5.3, 5.4, and 5.5.

In obs. Q, No. 26 and No. 27 were resolved only in the SIS image with a separation of $\sim 1'.3$. No. 85 was detected only in the hard band because of severe contamination from No. 81 in the soft band. No. 88 and No. 89 are located near the calibration isotope of GIS3, thus we used only GIS2 to estimate the significance. Since No. 88 and No. 89 are separated by only $\sim 1'.5$, which caused severe mutual contamination, we used very small circles to estimate their S/N ratio. We found that the S/N of No. 89 well exceeds 5, while that of No. 88 is slightly less than 5. However, a local peak at No. 88 was evidently also found in GIS3 (although no quantitative estimation is possible), thus we regard No. 88 as an X-ray source.

5.1.3 Construction of mosaic images

Figure 5.1 and 5.2 show the mosaic images in the soft and hard bands, that were created from images in each pointing observation. The method of creating a mosaic image from ASCA GIS images was developed by Sakano (2000), and thus we only give a brief summary

here.

1. We created images in the soft and hard bands for each observation, and cut off outer regions where non-X-ray background (NXB), contamination from the calibration isotope, and calibration uncertainty are large, according to the “GIS good mask” supplied by the GIS team (Ueda 1996).
2. The GIS night-earth image provided by NASA/GSFC was used as the NXB image, for which the same cut-off was applied. The intensity of the NXB image was adjusted according to the observation date, in consideration of the increasing rate of the NXB reported by Ishisaki et al. (1997).
3. An effective exposure map was created for each observation. Differences in the detection efficiency at different points on the GIS, which were caused by the vignetting of the XRT, the supporting grid structure of the GIS, and other factors, are included in this map.
4. The images, the NXB map, and the effective exposure map were smoothed with a Gaussian filter of $\sigma = 2.5$ pixels.
5. The smoothed NXB map was subtracted from the smoothed image.
6. The NXB-subtracted smoothed images from all the observations were put together into a mosaic image, according to the pointing direction and the roll angle of each observation.
7. Finally, the mosaic image was divided by the smoothed exposure map. The exposure-corrected mosaic images thus obtained in two energy bands are given in figures 5.1 and 5.2. These images are combined into a two color image and presented in figure A.1.

5.2 Position Determination

We first determined the position of each source simply by the coordinates of the peak pixel in the smoothed GIS images, and then performed a correction developed by Gotthelf et al. (2000). This correction compensates for the positional uncertainty caused by the ASCA attitude error, which depends on the temperature of the base-plate of the star-tracker and

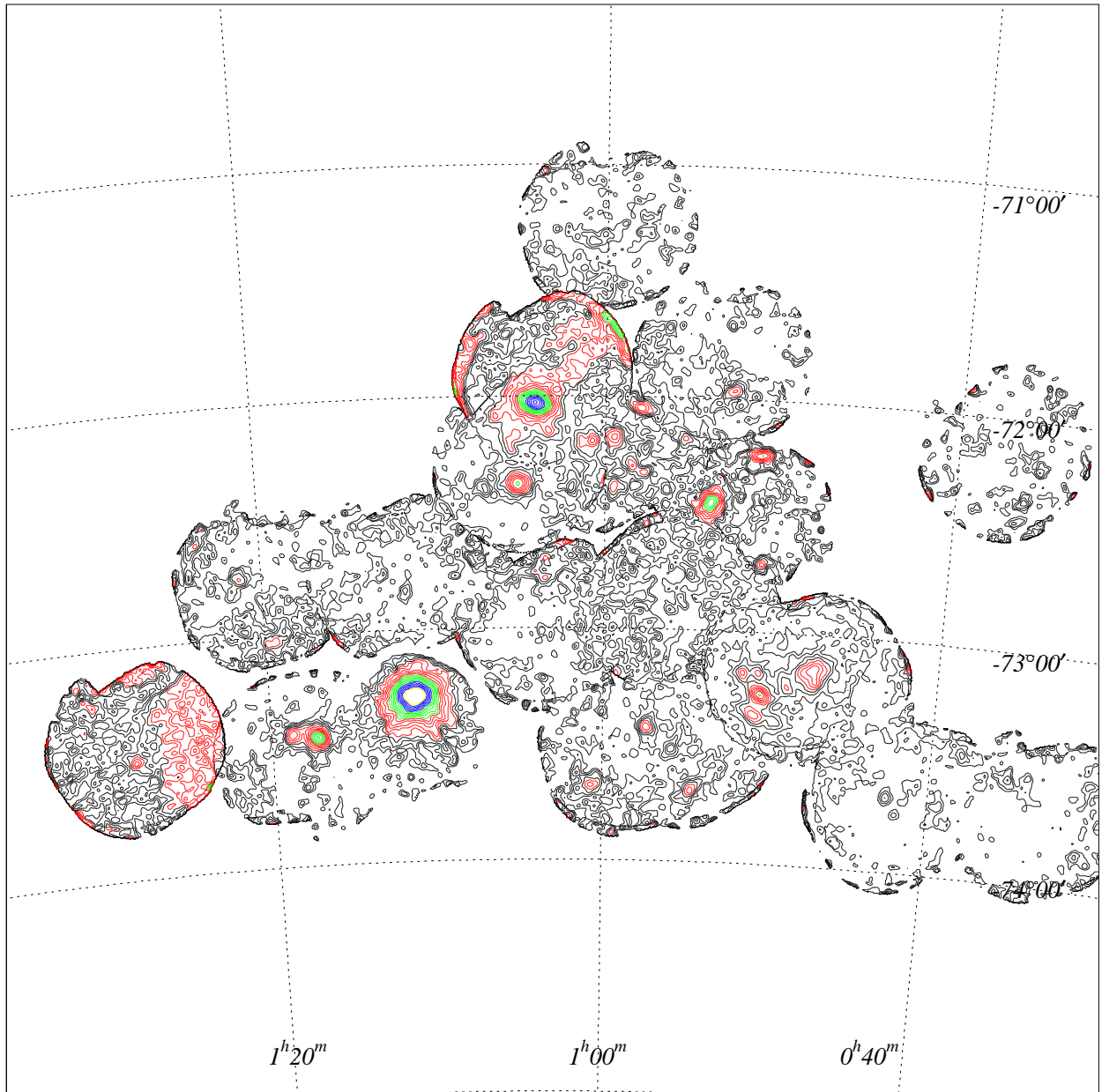


Figure 5.1: Mosaic image of the SMC obtained with ASCA GIS in the soft band (0.7–2.0 keV), overlaid with equatorial coordinates (J2000). The effects of non-X-ray background, telescope vignetting, and difference of exposure time between observations were corrected as described in the text. Contour levels are linearly spaced. Of the two observations centered on SMC X-1 (obs. A and C), only obs. C was used, in which SMC X-1 was much fainter.

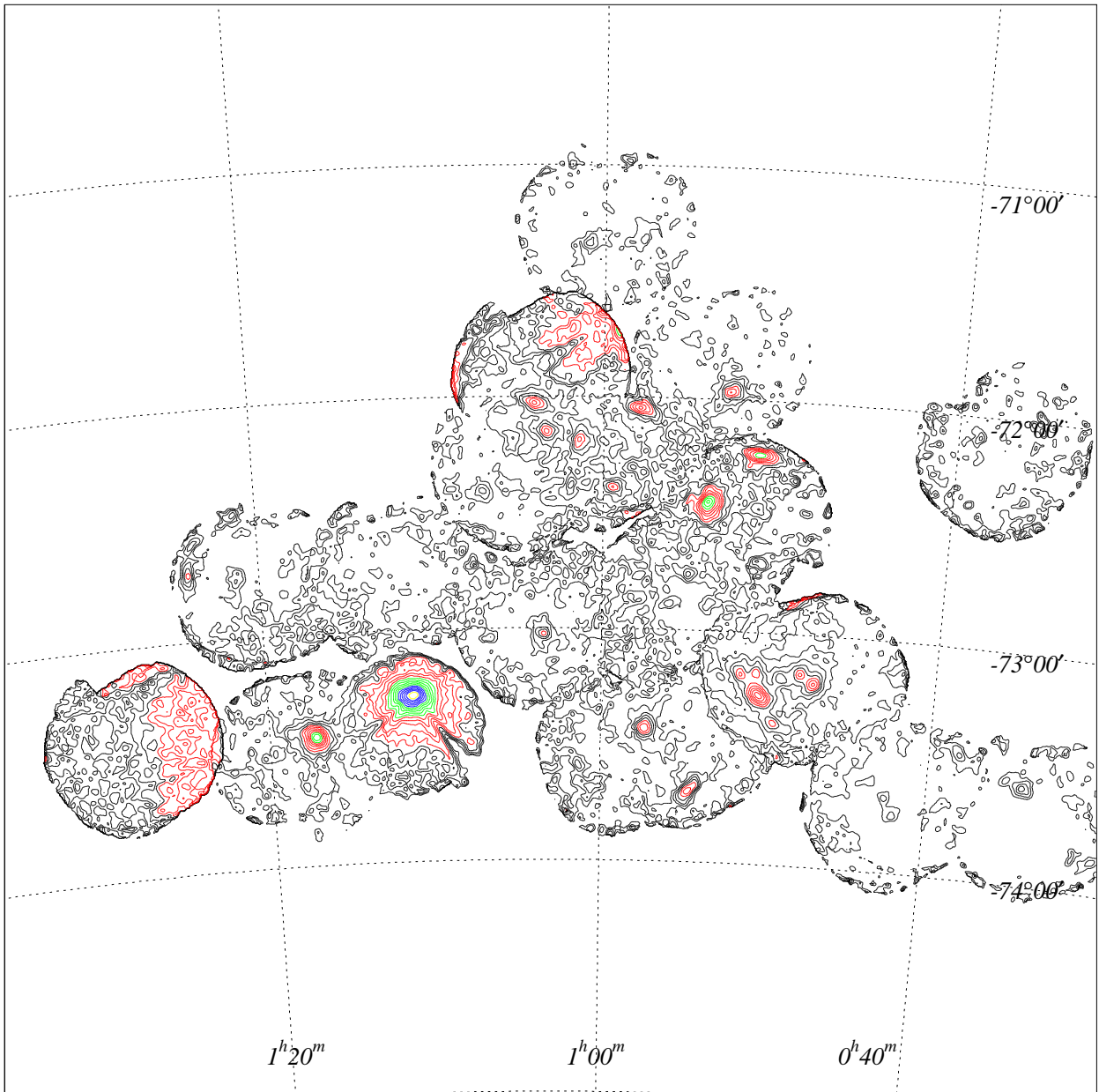


Figure 5.2: The same as figure 5.1, but for the hard band (2.0–7.0 keV).

the geometry of the solar illumination. SIS images were used only for resolving No. 26 and No. 27 in obs. Q.

According to this correction, the coordinates of some X-ray pulsars with an “AX J” name (which have been included in previous publications) are now inconsistent with the source name; for example, the coordinates of AX J0051.6–7311 (No. 40; Yokogawa et al. 2000b) are now ($00^{\text{h}}51^{\text{m}}44.5, -73^{\circ}10'34''$). In this paper, we do not rename these sources to avoid name confusion, and adopt the names used in the first publications for each pulsar.

5.2.1 Absolute accuracy of the position

The correction developed by Gotthelf et al. (2000) reduces the systematic positional uncertainty to $24''$ (90% error radius) for sources detected in the central $10'$ radius of the GIS. However, additional errors from the photon statistics and the method of position determination, and errors for the sources located out of the central $10'$ radius, are unknown. Therefore, we examined the “practical” errors for sources detected anywhere in the GIS as follows.

So far the ROSAT HRI catalogue (Sasaki, Haberl, & Pietsch 2000) presents the most accurate positions for the SMC X-ray sources, with an error radius of $\sim 1\text{--}10''$. Several sources in the ROSAT PSPC catalogue (Haberl et al. 2000) also have a small error radius of $\lesssim 10''$. Therefore, we investigated the separation angles between the ROSAT sources and their ASCA counterparts, which would represent the “practical” errors for the ASCA sources.

We primarily selected ASCA counterparts for ROSAT sources that were within $90''$ of each ROSAT source. In order to reject accidental coincidences and ambiguous counterparts, we further added rather conservative criteria:

1. For sources catalogued in both the PSPC and HRI catalogues, only HRI sources were used, which provide more accurate positions.
2. Only ROSAT sources with an error radius smaller than $7''$ were used. Since the error radii for ASCA sources are $> 24''$, the additional error from the ROSAT sources is $< 1''$ when we take a root sum square of all the errors.
3. For a ROSAT source with a Be star or a supergiant companion, the ASCA counterpart should exhibit coherent pulsations with a period of $\gtrsim 1$ s. The procedure for pulse

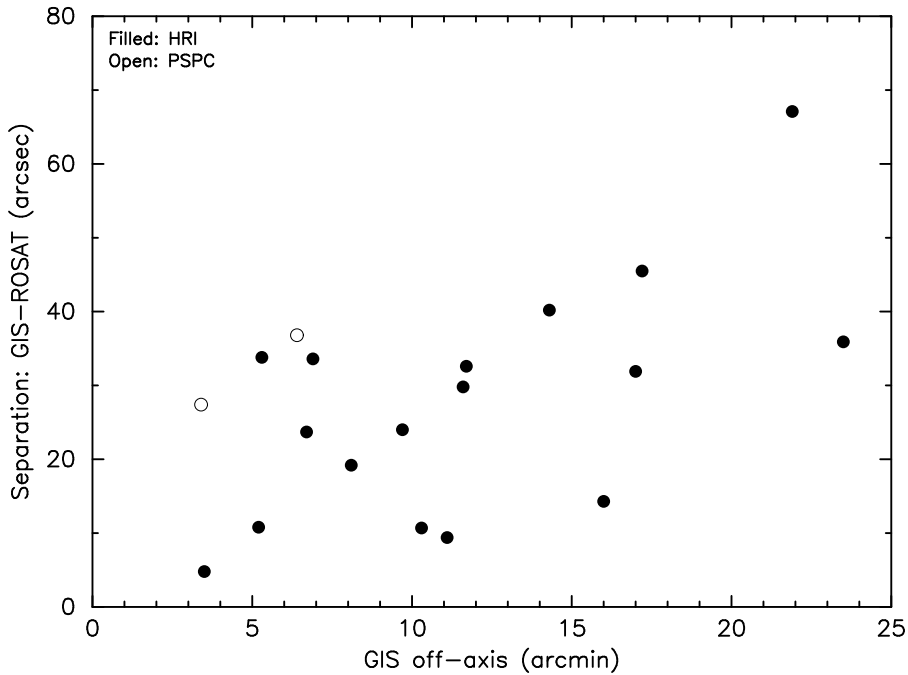


Figure 5.3: Plot of the separation angles between the ROSAT–ASCA counterparts as a function of the off-axis angle of the ASCA sources (see table 5.1). Filled and open circles indicate the sources detected with ROSAT HRI and PSPC, respectively.

detection is described in section 5.3. This criterion selects well-established X-ray binary pulsars (hereafter, XBPs). Although ASCA source No. 94 in obs. C exhibited no significant pulsations, it entered an eclipse phase as the ephemeris predicts for SMC X-1 (Wojdowski et al. 1998), thus we regard No. 94 in obs. C as SMC X-1.

4. For a ROSAT source at the position of a radio SNR, the ASCA counterpart should exhibit a soft spectrum with emission lines from ionized atoms. The method used to detect emission lines is described in section 5.4.3. This criterion selects bright thermal SNRs.

According to these criteria, we selected 19 pairs of ASCA–ROSAT counterparts as summarized in table 5.1. Although No. 67 is certainly the counterpart for RX J0059.2–7138 (see section 6.1.16), this pair is not included in table 5.1 because No. 67 is detected at the very edge of the GIS (or may be slightly outside of the GIS) and so the position determination is not reliable. We show the separation angles as a function of the off-axis angle of the ASCA

Table 5.1: ASCA counterparts for ROSAT sources selected with the conservative criteria (see text).

— ROSAT* —		— ASCA† —				Remarks
No.	Error (")	No.	Obs. ID	Off-axis (')	Sep‡ (")	
34	1.8	32	F	17.0	31.9	Be-XBP AX J0051–733 ($P = 323$ s)
34	1.8	32	Q	9.7	24.0	Be-XBP AX J0051–733 ($P = 321$ s)
37	2.6	37	H	17.2	45.5	Be-XBP AX J0051–722 ($P = 91$ s)
38	2.7	36	Q	14.3	40.2	SNR 0049–736
41	1.5	40	Q	11.7	32.6	Be-XBP AX J0051.6–7311 ($P = 172$ s)
46	3.0	44	T	8.1	19.2	Be-XBP XTE J0054–720 ($P = 167$ s)
51	2.4	47	H	10.3	10.7	Be-XBP 1WGA J0053.8–7226 ($P = 46$ s)
58	2.6	51	G	21.9¶	67.1	Be-XBP XTE J0055–724 ($P = 58$ s)
73	6.4	61	G	11.6	29.8	Be-XBP? AX J0058–7203 ($P = 280$ s)
82	4.0	66	G	3.5	4.8	SNR 0057–7226
101	3.8	78	D	9.4	11.1	Be-XBP 1SAX J0103.2–7209 ($P = 348$ s)
107	3.3	81	B	6.7	23.7	SNR 0102–723
107	3.3	81	D	16.0	14.3	SNR 0102–723
109	3.6	82	D	5.2	10.8	SNR 0103–726
118	0.7	94	A	6.9	33.6	XBP (supergiant) SMC X-1 ($P = 0.70$ s)
118	0.7	94	C	5.3	33.8	XBP (supergiant) SMC X-1 (eclipse)
118	0.7	94	I	23.5¶	35.9	XBP (supergiant) SMC X-1 ($P = 0.70$ s)
413§	6.8§	21	F	3.4	27.4§	SNR 0045–734
413§	6.8§	21	Q	6.4	36.8§	SNR 0045–734

Note — “Be-XBP” indicates an XBP with a Be star counterpart.

*: Source number and error radius of the ROSAT source presented by Sasaki, Haberl, & Pietsch (2000; HRI catalogue). The last two lines are from Haberl et al. (2000; PSPC catalogue).

†: Source number, observation ID, and off-axis angle of the ASCA counterpart (table 5.3).

‡: Separation angle between the ROSAT and ASCA sources.

§: The position of the ROSAT source was assumed to be the central point of No. 413 and No. 419 in Haberl et al. (2000), because SNR 0045–734 is catalogued as those two sources due to its extended X-ray emission. The error radius of the ROSAT source was taken from No. 413, while that for No. 419 is smaller, $4''7$.

¶: Detected in the outer ring of the GIS.

source in figure 5.3. No clear correlation between the separation angle and the off-axis angle could be found. Out of 17 ASCA sources detected in the inner circle (off-axis $< 20'$), 15 sources have separation angles less than $40''$. Therefore, we tentatively conclude that the “practical” error radius for GIS sources detected in the inner circle is $40''$ at 90% confidence level, although the statistics are rather limited. This is similar to the result obtained from the more elaborate analysis by Ueda et al. (1999). For sources detected in the outer ring, no constraint could be applied due to the small number of sources.

From the ROSAT and Einstein catalogues (Haberl et al. 2000; Sasaki, Haberl, & Pietsch 2000; Wang & Wu 1992), we selected the counterpart for each ASCA source within a circle of a radius $\sim 60''$ for sources detected in the inner circle, or within a circle of a radius $\sim 70''$ for sources detected in the the outer ring. Radii larger than the 90% error radius ($40''$) were used in order to simply avoid missing identification.

5.2.2 Identification of sources detected in multiple ASCA observations

As shown in figure 4.1, neighbouring ASCA observation fields more or less overlap each other. Therefore, a pair of sources detected in two observations within the overlapped region may be the same source. In order to examine whether those pairs are the same source or not, we primarily selected pairs of sources within $90''$ of each other, and classified them into four grades as follows:

Grade A Both of the sources exhibit coherent pulsations with nearly the same period, or exhibit emission lines from the same elements and have the same radio SNR as a counterpart (see sections 5.3 and 5.4.3 for the relevant analyses).

Grade B Both of the sources have soft spectra and have the same radio SNR as a counterpart. Pairs of No. 94 in obs. A and C and that in obs. I and C (SMC X-1) are also included in this grade. Grades A and B surely consist of pairs of XBPs and thermal SNRs.

Grade C Both of the sources are located near the same pulsar and their spectral parameters are consistent with those of the pulsar. Sources of grade C are likely to be X-ray pulsars.

Grade D The remainder.

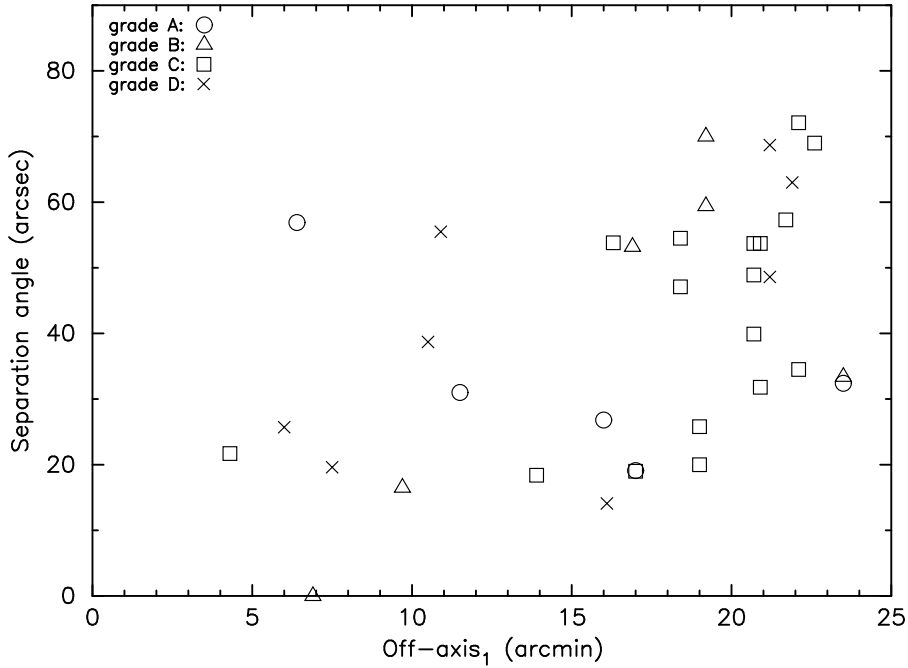


Figure 5.4: Plot of the separation angles as a function of the larger off-axis angle (off-axis₁ in table 5.2) of ASCA sources detected multiple times.

We regarded pairs of grade A–C as the same source, i.e., sources detected in multiple observations, and thus labeled them with the same source number in the ASCA catalogues (table 5.3, 5.4, and 5.5). We summarize the separation angle and the off-axis angles of the two sources in each pair in table 5.2, while in figure 5.4 we give a plot of the separation angle vs. the larger off-axis angle. We found that the separation angle is $\lesssim 60''$ if both of the two sources are detected in the inner circle, or $\lesssim 70''$ ($73''$) if at least one of the two is detected in the outer ring. Therefore, we regard pairs of grade D to be the same source if they satisfy the above condition, and labeled them the same source number. Pairs thus selected are also summarized in table 5.2 and plotted in figure 5.4. After this selection, we concluded that ASCA detected 106 sources with no double count.

Table 5.2: ASCA sources detected in multiple observations.

No.	Obs. ID ₁	Off- axis ₁ (')	Obs. ID ₂	Off- axis ₂ (')	Sep (")	Grade	Remarks
21	Q	6.4	F	3.4	56.9	A	SNR 0045–734
32	F	17.0	Q	9.7	19.1	A	Be-XBP AX J0051–733
56	L	11.5	R	7.3	31.0	A	XBP AX J0057.4–7325
81	D	16.0	B	6.7	26.8	A	SNR 0102–723
94	I	23.5*	A	6.9	32.4	A	XBP (supergiant) SMC X-1
25	F	9.7	Q	4.2	16.5	B	SNR 0047–735
36	F	19.2*	L	16.9	70.0	B	SNR 0049–736
36	F	19.2*	Q	14.2	59.4	B	SNR 0049–736
36	L	16.9	Q	14.2	53.2	B	SNR 0049–736
94	I	23.5*	C	5.3	33.4	B	XBP (supergiant) SMC X-1
94	A	6.9	C	5.3	1.0	B	XBP (supergiant) SMC X-1
17	P	4.3	K	2.7	21.7	C	Pulsar AX J0043–737
24	F	22.1*	H	21.7*	72.1	C	Be-XBP AX J0049–729
24	F	22.1*	Q	17.4	34.5	C	Be-XBP AX J0049–729
24	H	21.7*	Q	17.4	57.3	C	Be-XBP AX J0049–729
30	L	20.7*	F	16.3	48.9	C	Be-XBP? AX J0049.5–7323
30	F	16.3	Q	13.7	53.8	C	Be-XBP? AX J0049.5–7323
30	L	20.7*	Q	13.7	39.9	C	Be-XBP? AX J0049.5–7323
40	F	20.9*	L	20.7*	31.8	C	Be-XBP AX J0051.6–7311
40	F	20.9*	Q	11.7	53.7	C	Be-XBP AX J0051.6–7311
40	L	20.7*	Q	11.7	53.7	C	Be-XBP AX J0051.6–7311
61	T	22.6*	G	11.6	69.0	C	Be-XBP? AX J0058–7203
74	B	18.4	D	17.0	47.1	C	Be-XBP RX J0101.3–7211
74	D	17.0	G	10.4	19.0	C	Be-XBP RX J0101.3–7211
74	B	18.4	G	10.4	54.5	C	Be-XBP RX J0101.3–7211
78	B	13.9	D	11.1	18.4	C	Be-XBP 1SAX J0103.2–7209
78	G	19.0	D	11.1	20.0	C	Be-XBP 1SAX J0103.2–7209
78	G	19.0	B	13.9	25.8	C	Be-XBP 1SAX J0103.2–7209
20	Q	7.5	F	2.7	19.6	D	
22	F	6.0	Q	3.3	25.7	D	
26	F	10.5	Q	2.6 [†]	38.7	D	
28	L	21.2*	F	21.0*	48.6	D	
28	L	21.2*	Q	20.9*	68.7	D	
52	T	21.9*	G	15.6	63.0	D	
53	R	10.9	L	4.7	55.5	D	
76	G	16.1	D	14.3	14.1	D	

Note — Columns 1–6 show the source number, the observation IDs and off-axis angles for multiple detections, and the separation angle between the positions in the two observations. Off-axis angles are sorted so that off-axis₁ is larger than off-axis₂. “Be-XBP” indicates an XBP with a Be star counterpart.

*: Detected in the outer ring of the GIS.

†: Detected with the SIS.

5.3 Timing Analyses

We performed a Fast Fourier Transform (FFT) analysis on all of the sources to search for coherent pulsations. For sources with high count rates, we used only high-bit rate data in order to utilize the maximum time resolution (up to 62.5 ms). Otherwise we used high-bit and medium-bit data simultaneously to achieve better statistics at the sacrifice of a reduction in time resolution to 0.5 s (7.8125 ms for obs. J and 125 ms for obs. O; see the caption of table 4.1). We detected coherent pulsations from 17 sources, eight of which are new discoveries from this study. We show the power spectrum densities (PSDs) obtained from No. 94 (SMC X-1; in obs. A) and No. 56 (AX J0057.4–7325; in obs. R) in figure 5.5 (a) and (b) as examples of unambiguous detection. No. 83 (AX J0105–722) exhibits rather weak signs of pulsations as shown in figure 5.5 (c). Detection of pulses from AX J0105–722 and No. 26 (AX J0049–732) was not straightforward because of contamination from nearby sources. Details are described in section 6.1.19 and section 6.1.4, respectively.

In any observation, photon events are originally counted with a time spacing of 1/16 of the nominal resolution and stored in the temporary memory. The events are then collectively sent to the telemetry with a time spacing equal to the nominal resolution. Therefore, if the event rate is so low as not to fill the memory, the time resolution could be 1/16 of the nominal value (Hirayama et al. 1996). For this reason, we carried out FFT analysis on several faint sources with a time resolution of 31.25 ms, using the high- and medium-bit data. The 87 ms pulsations from AX J0043–737 were thus discovered (see section 6.1.2 for further details).

In order to determine the pulse period precisely, we performed an epoch folding search for the 17 sources from which pulsations were detected by FFT analysis. The orbital Doppler effect was corrected only for SMC X-1, using the ephemeris presented by Wojdowski et al. (1998). Since the eccentricity is near zero (< 0.00004), the intrinsic period P_0 was derived as

$$P_0 = \frac{P}{1 - 2\pi a \sin i \sin \Phi / cP_{\text{orb}}}, \quad (5.2)$$

where P , a , i , Φ , and P_{orb} are the pulse period determined by the epoch folding search, orbital radius, inclination angle, orbital phase at the midst of the observation, and orbital period, respectively. The derived pulse periods are presented in table 6.1.

We detected no pulsations by FFT analysis from three sources which are positionally coincident with known pulsars: No. 43 (RX J0052.1–7319), No. 51 (XTE J0055–724), and No. 94 in obs. C (SMC X-1). Therefore, we performed the epoch folding search around the

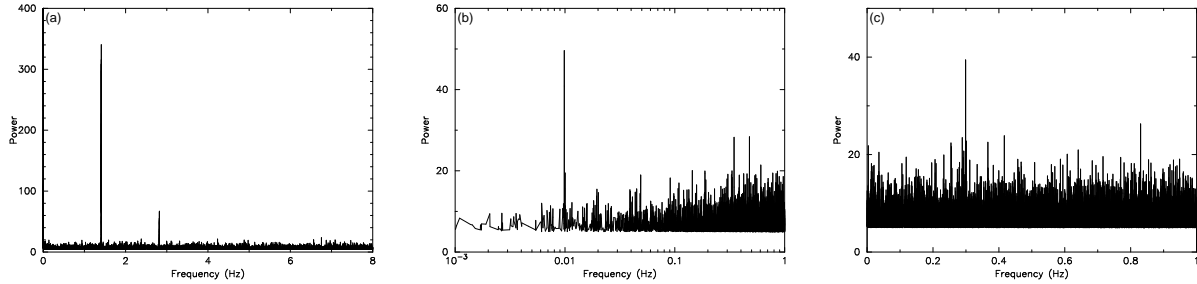


Figure 5.5: Examples of the PSDs from (a) SMC X-1, (b) AX J0057.4–7325, and (c) AX J0105–722. Data points with a power less than 5 are not plotted. Pulsations were detected unambiguously from most pulsars like (a) or (b), while AX J0105–722 exhibits rather weak evidence as seen in (c).

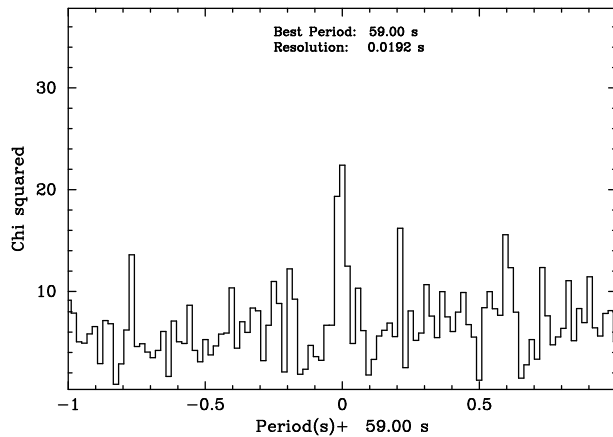


Figure 5.6: Periodogram for XTE J0055–724 around the known period of ~ 59 s.

known periods. Since SMC X-1 was in the 0.6-day eclipse phase during obs. C, we only used the data from noneclipse times. Consequently, we detected a weak peak only from No. 51 at the known period of ~ 59 s (figure 5.6), which is the evidence that No. 51 and XTE J0055–724 are the same source. This period is, however, not presented in table 6.1 because of the low significance of the pulse detection.

We also searched for burst-like activities by using light curves binned with various time scales from ~ 1 s to ~ 1 hr. Although no source exhibited the bursts typical of LMXBs, No. 20 (IKT1, in obs. Q) showed a flare with a decay time of $\sim 2 \times 10^4$ s. Details are given in section 6.5.1.

5.4 Spectral Analyses

5.4.1 Overview

We analyzed the spectrum of each source and derived various parameters as given in table 5.5: the hardness ratio (HR), photon index (Γ), temperature (kT), column density (N_{H}), flux (F_{X}), and absorption-corrected luminosity (L_{X}).

The analyses were not performed for Nos. 85, 88, and 89 because of severe contamination of these sources (see section 5.1.2). Spectra from GIS2 and GIS3 were co-added to increase the statistics, except for sources detected near the calibration isotope of either GIS and sources detected in only a single GIS¹. SIS spectra (SIS0 + SIS1) were used for No. 26 and No. 27 in obs. Q in order to spatially resolve these sources, and for SNRs 0045–734 (No. 21), 0047–735 (No. 25), 0057–7226 (No. 66), 0102–723 (No. 81), and 0103–726 (No. 82) to perform high resolution spectroscopy².

The parameters were derived from fitting the spectra with spectral models: different models were used according to the nature of each source, as described in the subsequent sections. For sources detected in multiple observations (table 5.2), we first fitted the spectrum from each observation separately. Except for SMC X-1, the spectral parameters (except flux) in each observation were found to be consistent with each other. We thus simultaneously fitted all the spectra with parameters linked between the observations, in order to apply more stringent constraints. However, the flux was not linked in the simultaneous fitting, in order to examine the flux variability; note that there could be $\lesssim 10\text{--}20\%$ error in the flux of most sources. Hardness ratios for those sources were derived after adding the spectra from all observations.

5.4.2 Hardness ratio

Spectral hardness ratio (HR) was derived by the definition

$$\text{HR} \equiv \frac{H - S}{H + S}, \quad (5.3)$$

¹Since the FOVs of the two GISs are pointed toward slightly different directions, it is possible for a source to be located at the very edge of one GIS and outside of the other GIS.

²For 0047–735, the SIS spectrum in obs. F was not used because the statistics were too poor.

where H and S represent background-subtracted GIS count rates in 2.0–7.0 keV and 0.7–2.0 keV, respectively. HR is not given for No. 27 in table 5.5 because this source was only resolved with SIS in obs. Q. For the same reason, HR of No. 26 was derived only from the data of obs. F.

5.4.3 SNRs

X-rays were detected from eight SNRs³, 0045–734 (No. 21), 0047–735 (No. 25), 0057–7226 (No. 66), 0102–723 (No. 81), 0103–726 (No. 82), 0046–735 (No. 23), 0049–736 (No. 36), and 0056–725 (No. 64). The former five were detected with SIS and the latter three were only detected with GIS. Before fitting the overall spectra, we distinguished thermal SNRs from the others. Direct evidence for a thermal spectrum is the presence of emission lines from highly ionized atoms. The brightest SNR, 0102–723, has been known to exhibit a thermal spectrum (e.g., Hayashi et al. 1994), thus we looked for the existence of emission lines in the spectra of the remaining seven SNRs as follows. We fitted the spectra in a narrow energy band (~ 1.1 –3 keV) with a bremsstrahlung continuum and three narrow Gaussian lines centered at 1.34 keV, 1.85 keV, and 2.46 keV ($K\alpha$ lines from He-like Mg, Si, and S, respectively). If the line intensity I and its 90% error δI satisfied $I - \delta I > 0$ for at least one line, we regarded the SNR as a thermal SNR. As a result, 0045–734, 0057–7226, 0102–723, 0103–726, and 0049–736 were regarded as thermal SNRs. We therefore fitted their spectra with thin-thermal plasma models as described in section 6.3. For the other SNRs, we first fitted the spectra with both a power-law model and a thin-thermal model in a collisional ionization equilibrium (CIE) state (Raymond & Smith 1977), and finally adopted a power-law for 0056–725 and the CIE thermal model for 0047–735 and 0046–735, for reasons described in section 6.3. When fitting with thermal models, the metal abundances were primarily fixed at 0.2 solar, which is the mean value for the SMC ISM (Russell & Dopita 1992; hereafter “SMC mean value”), unless otherwise mentioned.

³No. 83 (AX J0105–722) was once identified with SNR DEM S128 (Yokogawa et al. 2000e), but now the identification is questionable due to the improved position of the ASCA source and the high resolution ROSAT study (Filipović, Pietsch, & Haberl 2000). See also section 6.1.19.

5.4.4 X-ray pulsars and HMXBs

The spectra of X-ray pulsars (regardless of whether they are accretion-powered or rotation-powered) are generally described by a power-law in the ASCA bandpass. Therefore, we adopted a power-law model for the 20 detected pulsars (summarized in table 6.1) and also for No. 63 (a Be/X-ray binary, RX J0058.2–7231).

Several sources exhibited systematic deviation from the simple power-law. Since No. 49 (SMC X-2) and No. 90 (XTE J0111.2–7317) showed bump-like residuals around 6–7 keV, we added a narrow Gaussian line to the model. For No. 67 (RX J0059.2–7138), the power-law model exceeded the data at $\gtrsim 7$ keV, thus we included a high-energy cutoff in the model. The brightest pulsars (RX J0059.2–7138, XTE J0111.2–7317, and SMC X-1) all exhibited large data excess over the power-law at $\lesssim 2$ keV, thus we added a blackbody component to describe the soft excess. Details of the analyses and comments are given for each source in section 6.1.

5.4.5 Remaining sources

Although the nature of X-ray emission from the remaining sources is unclear at this moment, we basically adopted a power-law model in the spectral fitting. Since No. 22 (AX J0048.2–7309) showed weak evidence for an emission line at around 6–7 keV, we added a Gaussian line to the model (see section 6.5.2). For No. 2 and No. 13, no constraint on the spectral parameters could be obtained due to highly limited statistics, thus we do not present the parameters in table 5.5. For No. 39, the best-fit model ($\Gamma = 10$ and $N_{\text{H}} = 1.4 \times 10^{23} \text{ cm}^{-2}$) yielded a very high luminosity of $L_{\text{X}} \sim 3 \times 10^{39} \text{ erg s}^{-1}$. Such a high luminosity is unrealistic and is probably an artifact caused by the large Γ and N_{H} , thus we do not present L_{X} in table 5.5. For very soft sources (No. 6 and No. 45), we present the results both from a power-law model and a CIE thermal model.

5.5 Catalogue of Discrete X-Ray Sources in the SMC Region

We present a catalogue of the 106 X-ray sources in the SMC region detected with ASCA. The sources are presented separately in tables 5.3, 5.4, and 5.5. This catalogue is an upgraded version of that presented by Yokogawa et al. (2000e), including such improvements as enhanced observation fields, better positional accuracy, and the source flux for each observation.

5.5.1 Catalogue – I. Source identification

Legend for each column of table 5.3 —

- 1 Source number in the catalogue.
- 2–3 Source position in equatorial coordinates (J2000).
- 4 Indication whether the source was detected within the inner circle of the GIS (i) or in the outer ring region (o). The error radius for the source position is $\sim 40''$ for “i” sources and $\sim 70''$ for “o” sources (see section 5.2).
- 5 IDs for observations in which the source was detected. For sources detected multiple times, the first ID in this column was used to determine its position.
- 6 IDs for observations in which the source was not detected, although it was covered by the FOV of the GIS.
*: In these observations, nearby sources No. 32 and No. 94 were too bright, thus detection of No. 34 and No. 95 was hampered.
- 7–9 Identification with sources in other X-ray catalogues, including ROSAT PSPC (Haberl et al. 2000), ROSAT HRI (Sasaki, Haberl, & Pietsch 2000), and Einstein IPC (Wang & Wu 1992). Parentheses indicate the separation angle from the ASCA source in arcseconds.
‡: The separation angle from the central point of No. 413 and 419 in Haberl et al. (2000).
- 10 Source class defined in section 7.1 and section 7.2.3.
TS: Thermal SNRs. TSc is a candidate for TS.
RS: Radio SNRs which are not classified as TS.
BP: X-ray binary pulsars. BPc is a candidate for BP.
P: Pulsars which are not classified as BP.
NH: Non-pulsating HMXBs.
FS: Sources coincident with a foreground star.
AGN: Sources coincident with a background AGN.
UN: Unclassified sources.

Table 5.3: Final ASCA catalogue of discrete X-ray sources in the SMC region
 – I. Source identification.

No.	Coordinates (J2000)		i/o	Obs. ID		— ROSAT —		Einstein IPC (sep'')	Class
	R.A.	Dec.		Det.	N.D.	PSPC (sep'')	HRI (sep'')		
1	00 ^h 33 ^m 44 ^s .3	−73°21′41''	i	S		462 (14.0)			UN
2	00 ^h 34 ^m 05 ^s .4	−73°31′30''	i	S					UN
3	00 ^h 34 ^m 19 ^s .4	−73°33′57''	i	S					UN
4	00 ^h 35 ^m 18 ^s .3	−73°32′42''	i	S		518 (42.6)			UN
5	00 ^h 35 ^m 28 ^s .0	−72°12′43''	i	E		167 (30.6)	2 (30.7)		UN
6	00 ^h 36 ^m 09 ^s .2	−72°21′05''	i	E		211 (33.9)	4 (34.4)		TSc
7	00 ^h 38 ^m 09 ^s .9	−73°27′54''	i	P	K				UN
8	00 ^h 38 ^m 56 ^s .5	−72°04′53''	i	E		127 (47.4)	9 (44.8)		UN
9	00 ^h 39 ^m 03 ^s .1	−72°07′49''	i	E					UN
10	00 ^h 39 ^m 27 ^s .3	−73°41′58''	i	P	K				UN
11	00 ^h 39 ^m 52 ^s .0	−73°41′36''	i	K	P				UN
12	00 ^h 40 ^m 46 ^s .4	−73°36′58''	i	P	K				UN
13	00 ^h 41 ^m 29 ^s .9	−73°36′37''	i	P	K				UN
14	00 ^h 41 ^m 37 ^s .0	−73°26′47''	i	P	K	481 (30.2)			BPc
15	00 ^h 41 ^m 57 ^s .9	−73°43′22''	i	K	P				UN
16	00 ^h 42 ^m 04 ^s .8	−73°44′58''	i	P	K		11 (15.8)		BPc
17	00 ^h 42 ^m 39 ^s .9	−73°40′25''	i	KP		546 (16.7)	12 (17.8)		P
18	00 ^h 44 ^m 06 ^s .6	−73°37′03''	i	P	K				UN
19	00 ^h 45 ^m 25 ^s .6	−73°53′55''	o	P	K				UN
20	00 ^h 47 ^m 22 ^s .9	−73°12′06''	i	QF		434 (17.6)		18 (55.3)	NHc,BPc
21	00 ^h 47 ^m 30 ^s .0	−73°08′25''	i	QF		413(†36.8)		16 (37.9)	TS
22	00 ^h 48 ^m 14 ^s .0	−73°09′39''	i	QF				20 (46.5)	NHc,BPc
23	00 ^h 48 ^m 37 ^s .6	−73°18′59''	i	Q	F	454 (60.4)		21 (49.4)	RS,TSc
24	00 ^h 49 ^m 01 ^s .6	−72°51′46''	o	FQH		351 (54.1)			BP
25	00 ^h 49 ^m 08 ^s .3	−73°13′21''	i	QF		437 (44.8)		22 (46.7)	RS,TSc
26	00 ^h 49 ^m 18 ^s .5	−73°12′01''	i	FQ		430 (33.2)			P
27	00 ^h 49 ^m 26 ^s .3	−73°10′51''	i	Q	F	427 (49.6)			UN
28	00 ^h 49 ^m 32 ^s .0	−73°30′17''	o	LFQ		511 (67.6)	28 (52.4)		NHc,BPc
29	00 ^h 49 ^m 35 ^s .2	−73°02′47''	i	Q	F				BPc
30	00 ^h 49 ^m 42 ^s .8	−73°22′40''	i	QFL		468 (22.2)			BP
31	00 ^h 50 ^m 28 ^s .8	−72°58′35''	i	Q	F				UN
32	00 ^h 50 ^m 40 ^s .5	−73°15′46''	i	QF	L	444 (20.1)	34 (24.0)		BP
33	00 ^h 50 ^m 45 ^s .4	−72°41′57''	i	H			35 (17.9)		FS
34	00 ^h 50 ^m 50 ^s .7	−73°17′16''	o	L	F*Q*				UN
35	00 ^h 50 ^m 53 ^s .5	−73°10′07''	i	Q	F	421 (13.2)	36 (16.1)		NHc,BPc
36	00 ^h 50 ^m 58 ^s .1	−73°20′55''	i	QFL		461 (50.4)	38 (40.2)	24 (43.0)	TS
37	00 ^h 51 ^m 06 ^s .4	−72°13′58''	i	H			37 (45.5)		BP
38	00 ^h 51 ^m 25 ^s .4	−72°27′29''	i	H					BPc
39	00 ^h 51 ^m 39 ^s .9	−73°02′58''	i	Q	F				BPc
40	00 ^h 51 ^m 44 ^s .5	−73°10′34''	i	QFL		424 (30.6)	41 (32.6)	25 (31.4)	BP
41	00 ^h 51 ^m 55 ^s .7	−72°56′49''	i	Q					UN
42	00 ^h 51 ^m 56 ^s .2	−73°19′39''	i	Q	L			29 (46.5)	UN
43	00 ^h 52 ^m 22 ^s .1	−73°19′05''	o	F	LQ	453 (36.1)	44 (37.5)	29 (70.9)	BP
44	00 ^h 52 ^m 58 ^s .4	−71°57′54''	i	T		94 (19.3)	46 (19.2)	32 (47.5)	BP
45	00 ^h 53 ^m 29 ^s .2	−73°36′40''	i	L	R				TSc
46	00 ^h 53 ^m 42 ^s .1	−72°52′12''	i	J					UN
47	00 ^h 53 ^m 55 ^s .2	−72°26′42''	i	H		242 (20.9)	51 (10.7)	34 (15.0)	BP

(Continuing to the next page.)

Table 5.3: Final ASCA catalogue of discrete X-ray sources in the SMC region
 – I. Source identification (continued from the previous page).

No.	Coordinates (J2000)		i/o	Obs. ID		— ROSAT —		Einstein IPC (sep'')	Class
	R.A.	Dec.		Det.	N.D.	PSPC (sep'')	HRI (sep'')		
48	00 ^h 54 ^m 25 ^s .1	−73°30'32''	i	L	R				UN
49	00 ^h 54 ^m 36 ^s .2	−73°40'35''	i	R	L	547 (30.5)			BP
50	00 ^h 54 ^m 49 ^s .4	−72°44'23''	i	J		324 (50.4)	57 (52.1)		NHc,BPc
51	00 ^h 55 ^m 01 ^s .6	−72°25'49''	o	G		241 (63.5)	58 (67.1)	35 (43.0)	BP
52	00 ^h 55 ^m 36 ^s .1	−72°10'56''	i	GT		157 (40.9)	59 (34.0)	36 (19.6)	AGN
53	00 ^h 55 ^m 51 ^s .6	−73°30'32''	i	LR		508 (32.8)	65 (34.5)		UN
54	00 ^h 55 ^m 55 ^s .5	−72°52'15''	i	J			66 (31.1)		UN
55	00 ^h 57 ^m 27 ^s .2	−72°25'01''	i	G		234 (47.6)		39 (51.3)	UN
56	00 ^h 57 ^m 28 ^s .6	−73°25'29''	i	RL		476 (28.1)	70 (13.6)		BP
57	00 ^h 57 ^m 28 ^s .7	−72°50'17''	i	J					UN
58	00 ^h 57 ^m 29 ^s .3	−72°58'08''	i	J					UN
59	00 ^h 57 ^m 37 ^s .4	−72°19'07''	i	G					UN
60	00 ^h 57 ^m 54 ^s .2	−71°18'04''	i	U		14 (28.3)			UN
61	00 ^h 57 ^m 54 ^s .7	−72°02'26''	i	GT		114 (33.3)	73 (29.8)	41 (50.1)	BP
62	00 ^h 57 ^m 57 ^s .3	−73°08'55''	i	J					BPc
63	00 ^h 58 ^m 15 ^s .8	−72°30'26''	i	G		258 (32.7)	76 (28.0)		NH
64	00 ^h 58 ^m 19 ^s .5	−72°17'40''	i	G		194 (28.8)	77 (28.9)	42 (17.4)	RS,BPc
65	00 ^h 59 ^m 24 ^s .2	−72°22'35''	i	G		218 (44.0)	81 (46.8)		BPc
66	00 ^h 59 ^m 27 ^s .2	−72°10'03''	i	G		148 (10.6)	82 (4.8)	44 (10.5)	TS
67	00 ^h 59 ^m 35 ^s .3	−71°38'02''	o	B		53(121.5)			BP
68	01 ^h 00 ^m 09 ^s .0	−71°17'37''	i	U		13 (39.4)			UN
69	01 ^h 00 ^m 09 ^s .6	−72°57'36''	i	M			84 (10.1)		UN
70	01 ^h 00 ^m 12 ^s .1	−71°10'15''	i	U					BPc
71	01 ^h 00 ^m 32 ^s .8	−73°40'12''	i	R					UN
72	01 ^h 00 ^m 41 ^s .1	−72°11'16''	i	G		162 (18.5)	90 (18.1)	45 (38.4)	AGN
73	01 ^h 00 ^m 58 ^s .1	−71°20'04''	i	U		18 (21.2)			BPc
74	01 ^h 01 ^m 19 ^s .6	−72°10'59''	i	GDB		159 (22.0)	95 (18.6)		BP
75	01 ^h 01 ^m 27 ^s .8	−73°35'00''	i	R					BPc
76	01 ^h 01 ^m 53 ^s .0	−72°23'01''	i	DG		220 (26.9)	97 (34.3)		NHc
77	01 ^h 02 ^m 14 ^s .6	−71°17'20''	i	U					UN
78	01 ^h 03 ^m 15 ^s .3	−72°09'19''	i	DBG		143 (6.7)	101 (9.4)	50 (22.7)	BP
79	01 ^h 03 ^m 27 ^s .3	−73°01'24''	i	M		384 (8.8)			UN
80	01 ^h 03 ^m 27 ^s .5	−72°46'55''	i	M		334 (34.4)	104 (32.8)		AGN
81	01 ^h 04 ^m 01 ^s .7	−72°01'40''	i	BD		107 (7.9)	107 (23.7)	51 (18.7)	TS
82	01 ^h 05 ^m 01 ^s .2	−72°23'06''	i	D		217 (14.3)	109 (10.8)	52 (42.0)	TS
83	01 ^h 05 ^m 07 ^s .6	−72°10'34''	i	D	B				RS,P
84	01 ^h 05 ^m 30 ^s .1	−72°12'47''	i	D	B	172 (45.5)	112 (45.4)		AGN
85	01 ^h 05 ^m 52 ^s .1	−72°03'41''	i	D	B	120 (17.9)			NHc
86	01 ^h 06 ^m 48 ^s .5	−72°24'32''	i	D		230 (41.4)	116 (44.2)	55 (65.7)	UN
87	01 ^h 07 ^m 13 ^s .5	−72°34'39''	o	D		279 (58.3)		56 (46.0)	NHc
88	01 ^h 07 ^m 27 ^s .2	−72°43'26''	o	N		313 (9.1)			UN
89	01 ^h 07 ^m 39 ^s .5	−72°42'15''	o	N		307 (71.6)			UN
90	01 ^h 11 ^m 10 ^s .1	−73°16'32''	i	I	A	446 (40.7)			BP
91	01 ^h 11 ^m 45 ^s .8	−72°49'52''	i	N		348 (42.2)			AGN
92	01 ^h 12 ^m 38 ^s .7	−72°36'51''	i	N		283 (55.2)			AGN
93	01 ^h 13 ^m 05 ^s .5	−72°46'25''	i	N		330 (25.8)			BPc
94	01 ^h 17 ^m 08 ^s .5	−73°26'07''	i	ACI		482 (28.4)	118 (33.6)	63 (13.4)	BP

(Continuing to the next page.)

Table 5.3: Final ASCA catalogue of discrete X-ray sources in the SMC region
 – I. Source identification (continued from the previous page).

No.	Coordinates (J2000)		i/o	Obs. ID		— ROSAT —		Einstein IPC (sep'')	Class
	R.A.	Dec.		Det.	N.D.	PSPC (sep'')	HRI (sep'')		
95	01 ^h 18 ^m 37 ^s .9	−73°25'22''	i	C	A*	478 (4.0)	120 (5.0)	65 (13.0)	FS
96	01 ^h 19 ^m 27 ^s .3	−73°00'51''	i	V		385 (38.6)		66 (19.6)	UN
97	01 ^h 20 ^m 01 ^s .0	−72°51'46''	i	V					BPc
98	01 ^h 20 ^m 44 ^s .5	−72°55'13''	i	V					BPc
99	01 ^h 21 ^m 16 ^s .2	−72°27'42''	i	V					UN
100	01 ^h 21 ^m 23 ^s .9	−72°44'53''	i	V		316 (54.6)			UN
101	01 ^h 23 ^m 44 ^s .6	−72°34'26''	i	V		275 (43.7)			UN
102	01 ^h 24 ^m 15 ^s .7	−72°42'32''	i	V					UN
103	01 ^h 26 ^m 44 ^s .2	−73°04'20''	o	O					UN
104	01 ^h 27 ^m 48 ^s .0	−73°07'39''	i	O					BPc
105	01 ^h 28 ^m 28 ^s .6	−73°29'46''	i	O				67 (35.3)	UN
106	01 ^h 31 ^m 12 ^s .0	−73°13'44''	i	O					UN

5.5.2 Catalogue – II. Names and comments

Legend for each column of table 5.4 —

- 1 Source number in the catalogue.
- 2 Source names usually used in the literature. References for the abbreviations are Davies, Elliot, & Meaburn (1976) for DEM's, Inoue, Koyama, & Tanaka (1983) for IKT's, Henize (1956) for N's, and Mathewson et al. (1983, 1984) for SNR's.
- 3 Comments such as periods and companion stars of pulsars, and spectral information for peculiar sources. “Be/X?” indicates that the ROSAT counterpart has an emission line object in the error circle (Haberl & Sasaki 2000; here HS00). Excerpts of comments in ROSAT catalogues (Haberl et al. 2000 and Sasaki, Haberl, & Pietsch 2000; here HFP00 and SHP00, respectively) are also included.

Table 5.4: Final ASCA catalogue of discrete X-ray sources in the SMC region
 – II. Names and comments.

No.	Names	Comments
1		
2		
3		
4		
5		
6		fg star (HFP00); AGN? (SHP00)
7		
8		
9		
10		
11		
12		
13		
14		
15		
16		
17	AX J0043–737	$P = 87\text{ms?}$ (obs. K); XB? or AGN? (SHP00)
18		
19		
20	RX J0047.3–7312; IKT1	Be/X? (HS00); flare (obs. Q)
21	SNR 0045–734; N19; DEM S32; IKT2	old, ejecta-dominated, center-filled
22	AX J0048.2–7309	Be/X? (section 6.5.2); Fe line? (obs. Q; EW=240eV)
23	SNR 0046–735; N22; DEM S37; IKT4	
24	AX J0049–729; RX J0049.1–7250	$P = 74\text{s}$; Be/X
25	SNR 0047–735; DEM S49; IKT5	
26	AX J0049–732; RX J0049.0–7314	$P = 9.13\text{s}$
27	RX J0049.4–7310	Be/X? (HS00); pos. and spec. are from SIS
28	RX J0049.5–7331	Be/X? (HS00)
29		
30	AX J0049.5–7323; RX J0049.7–7323	$P = 755\text{s}$; Be/X? (HS00)
31		
32	AX J0051–733; RX J0050.8–7316	$P = 323\text{s}$; Be/X; flux increased gradually (obs. Q)
33		fg star SkKM 62 (SHP00)
34		
35	RX J0050.9–7310	Be/X? (HS00)
36	SNR 0049–736; IKT6	
37	AX J0051–722	$P = 91\text{s}$; Be/X
38		
39		
40	AX J0051.6–7311; RX J0051.9–7311; IKT7	$P = 172\text{s}$; Be/X
41		
42		
43	RX J0052.1–7319; IKT8	$P = 15\text{s}$ (not detected in this work); Be/X
44	XTE J0054–720; AX J0052.9–7157; RX J0052.9–7158; IKT9	$P = 167\text{s}$; Be/X
45		
46		
47	1WGA J0053.8–7226; XTE J0053–724; IKT10	$P = 46\text{s}$; Be/X
48		

(Continuing to the next page.)

Table 5.4: Final ASCA catalogue of discrete X-ray sources in the SMC region
– II. Names and comments (continued from the previous page).

No.	Names	Comments
49	SMC X-2	$P = 2.37\text{s}$; Be/X; Fe line (EW=400eV)
50	RX J0054.9–7245	Be/X? (HS00)
51	XTE J0055–724; 1SAX J0054.9–7226; IKT11	$P = 58\text{s}$; Be/X
52		AGN? (HFP00)
53		
54		
55	IKT14	
56	AX J0057.4–7325	$P = 101\text{s}$; probably an XBP
57		
58		
59		
60		
61	AX J0058–7203	$P = 280\text{s}$; Be/X? (HS00)
62		
63	RX J0058.2–7231	Be/X (HS00)
64	SNR 0056–725; IKT16	hard spectrum
65		XB? (SHP00)
66	SNR 0057–7226; N66; DEM S103; IKT18	old, ISM-dominated, center-filled
67	RX J0059.2–7138	$P = 2.76\text{s}$; Be/X; at the very edge of the GIS
68		
69		
70		
71		
72	IKT19	[hard] (HFP00); AGN? (SHP00)
73		
74	RX J0101.3–7211	$P = 455\text{s}$ (not detected in this work); Be/X
75		
76	RX J0101.8–7223	Be/X? (HS00)
77		
78	1SAX J0103.2–7209; SNR 0101–724; IKT21	$P = 348\text{s}$; Be/X
79		
80		AGN? (SHP00)
81	SNR 0102–723; N76; DEM S124; IKT22	
82	SNR 0103–726; DEM S125; IKT23	old, ejecta-dominated, center-filled + faint shell
83	AX J0105–722	$P = 3.34\text{s}?$; resolved into multiple sources by ROSAT
84		[nonstar] (HFP00); AGN? (SHP00)
85	RX J0105.9–7203	Be/X? (HS00); severe contamination from No. 81
86	DEM S134	[hard] (HFP00)
87	RX J0107.1–7235	Be/X? (HS00)
88		[nonstar] (HFP00); contamination from No. 89
89		contamination from No. 88
90	XTE J0111.2–7317	$P = 30\text{s}$; Be/X; Fe line (EW=50eV)
91		AGN $z = 0.197$ (HFP00)
92		AGN $z = 1.376$ (HFP00)
93		
94	SMC X-1	$P = 0.70\text{s}$; supergiant HMXB (B0I, Sk160)
95		fg star G5V, HD 8191

(Continuing to the next page.)

Table 5.4: Final ASCA catalogue of discrete X-ray sources in the SMC region
 – II. Names and comments (continued from the previous page).

No.	Names	Comments
96		cluster $z = 0.0656$ (HFP00)
97		
98		
99		
100		
101		
102		
103		in stray light
104		in stray light
105	AX J0128.4–7329	at the center of a supergiant shell, SMC-1
106		

5.5.3 Catalogue – III. Spectral parameters

Legend for each column of table 5.5 —

- 1 Source number in the catalogue.
- 2 Spectral hardness ratio (HR) defined as $\text{HR} \equiv (H - S)/(H + S)$, where H and S represent background-subtracted GIS count rates in 2.0–7.0 keV and 0.7–2.0 keV, respectively. For sources detected multiple times, spectra from all observations were added to derive the HR (except No. 94).
- 3 Error in the HR.
- 4 Observation ID. Flux and luminosity are given for each ID (in columns 8–10).
- 5–7 Photon index, temperature (keV), and column density (10^{21} cm^{-2}) derived in the spectral fitting (section 5.4). Parentheses indicate 90% confidence limits. For sources showing soft excess (Nos. 67, 90, and 94), a two-component model consisting of a power-law plus a blackbody was used; thus the temperature in the table is for the blackbody component. For No. 67, a power-law with a high-energy exponential cutoff was used. The cutoff and e -fold energies, E_{cut} and E_{fold} , are presented in table 6.16.
- 8–10 Flux ($10^{-12} \text{ erg s}^{-1} \text{ cm}^{-2}$), observed luminosity ($10^{36} \text{ erg s}^{-1}$), and absorption-corrected luminosity ($10^{36} \text{ erg s}^{-1}$). Observed luminosity is defined as

$$L_{\text{obs}} = F_{\text{X}} \times 4\pi d^2,$$

where $d = 60 \text{ kpc}$ is the distance to the SMC. We also adopted $d = 60 \text{ kpc}$ for sources coincident with background AGNs or foreground stars.

*: The best-fit model yielded an unusually high luminosity of $\sim 3 \times 10^{39} \text{ erg s}^{-1}$. This is probably an artifact due to the large values of Γ and N_{H} , thus we omitted it from the table.

†: The intrinsic intensity would be much higher (see section 6.1.21).

Table 5.5: Final ASCA catalogue of discrete X-ray sources in the SMC region
 – III. Spectral parameters.

No.	HR	HRerr	Obs. ID	Γ	kT	N_{H}	F_{X}	L_{obs}	L_{X}
1	-0.27	0.14	S	2.5 (1.7-4.6)		2 (<15)	0.53	0.23	0.29
2	-1.00	2.00	S
3	0.64	0.09	S	1.8 (1.0-3.0)		47 (17-100)	0.72	0.31	0.65
4	-0.13	0.18	S	1.9 (1.2-3.7)		0 (<7)	0.21	0.091	0.091
5	-0.27	0.24	E	2.1 (1.0-5.3)		3 (<22)	0.28	0.12	0.15
6	-0.79	0.35	E	3.6 (>2.2)		2 (<37)	0.25	0.11	0.16
6	-0.79	0.35	E		1.1 (0.1-2.5)	0 (<20)	0.23	0.099	0.099
7	0.02	0.12	P	1.4 (1.0-2.0)		0 (<0.5)	0.52	0.22	0.22
8	0.16	0.23	E	1.8 (0.7-4.2)		7 (<46)	0.19	0.082	0.11
9	-0.16	0.25	E	2.2 (1.3-5.2)		0 (<20)	0.12	0.052	0.052
10	-0.02	0.20	P	1.2 (0.5-5.1)		0 (<69)	0.20	0.086	0.086
11	-0.15	0.16	K	2.0 (1.4-3.5)		0 (<6)	0.24	0.10	0.10
12	-0.09	0.24	P	2.1 (1.3-4.4)		0 (<31)	0.066	0.029	0.029
13	-1.00	1.15	P
14	0.22	0.23	P	2.1 (0.8-4.2)		9 (<31)	0.13	0.056	0.086
15	0.86	0.25	K	3.9 (2.2-7.0)		57 (23-120)	0.16	0.069	1.2
16	0.43	0.10	P	1.8 (0.9-2.9)		18 (0.7-39)	0.31	0.13	0.22
17	-0.16	0.15	K	1.7 (1.3-2.4)		0 (<4)	0.20	0.086	0.086
17			P				0.11	0.048	0.048
18	0.15	0.10	P	2.2 (1.3-3.6)		11 (0.6-28)	0.27	0.12	0.20
19	0.13	0.15	P	1.5 (0.9-2.5)		0 (<6)	0.48	0.21	0.21
20	0.39	0.03	F	1.0 (0.9-1.2)		4 (1-7)	0.67	0.29	0.32
20			Q				1.4	0.60	0.65
21	-0.86	0.06	F		0.37 (0.32-0.47)	10 (8-11)	0.29	0.13	1.3
21			Q				0.29	0.13	1.3
22	0.59	0.05	F	0.8 (0.6-1.1)		9 (3-17)	0.20	0.086	0.099
22			Q				1.1	0.48	0.52
23	-0.62	0.36	Q		0.9 (0.1-1.8)	0 (<15)	0.058	0.025	0.025
24	0.36	0.03	F	1.0 (0.8-1.1)		3 (2-5)	12	5.2	5.5
24			H				1.6	0.69	0.76
24			Q				0.71	0.31	0.33
25	-1.00	1.38	F		0.86 (0.82-0.90)	0 (<0.4)	0.14	0.060	0.060
25			Q				0.11	0.048	0.048
26	0.85	0.20	F	0.9 (0.3-1.6)		15 (6-28)	0.64	0.28	0.33
26			Q				0.37	0.16	0.19
27	Q	1.7 (0.8-2.9)		27 (11-58)	0.23	0.099	0.17
28	0.58	0.12	F	0.9 (0.3-1.7)		6 (<20)	0.82	0.35	0.39
28			L				1.1	0.48	0.51
28			Q				0.84	0.36	0.40
29	0.25	0.18	Q	1.0 (0.3-1.7)		0 (<19)	0.10	0.043	0.043
30	0.31	0.06	F	0.8 (0.7-1.0)		0 (<3)	1.1	0.48	0.48
30			L				1.5	0.65	0.65
30			Q				1.7	0.73	0.73
31	0.08	0.31	Q	1.3 (-0.1-4.5)		0 (<30)	0.077	0.033	0.033
32	0.43	0.01	F	0.76 (0.69-0.83)		2.2 (1.2-3.3)	2.9	1.3	1.3
32			Q				6.8	2.9	3.0
33	-0.16	0.16	H	2.2 (1.5-3.6)		2 (<11)	0.39	0.17	0.20

(Continuing to the next page.)

Table 5.5: Final ASCA catalogue of discrete X-ray sources in the SMC region
 – III. Spectral parameters (continued from the previous page).

No.	HR	HRerr	Obs. ID	Γ	kT	N_{H}	F_{X}	L_{obs}	L_{X}
34	0.09	0.20	L	0.6 (–0.4-1.6)		0 (<11)	1.3	0.56	0.56
35	0.42	0.04	Q	1.0 (0.8-1.3)		4 (0.9-8)	0.92	0.40	0.43
36	–0.92	0.07	F		0.23 (0.18-0.47)	6 (2-7)	0.64	0.28	1.8
36			L				0.65	0.28	1.8
36			Q				0.74	0.32	2.0
37	0.55	0.04	H	1.0 (0.7-1.3)		10 (5-16)	9.5	4.1	4.8
38	0.58	0.20	H	0.1 (–1.0-1.3)		0 (<21)	0.58	0.25	0.25
39	0.53	0.38	Q	10 (>2.7)		140 (95-200)	0.038	0.016	...*
40	0.33	0.04	F	0.9 (0.8-1.0)		0 (<0.8)	0.68	0.29	0.29
40			L				1.5	0.65	0.65
40			Q				1.3	0.56	0.56
41	0.05	0.32	Q	1.8 (0.5-5.5)		0 (<43)	0.10	0.043	0.043
42	0.67	0.29	Q	3.3 (1.2-7.1)		6 (1-16)	0.19	0.082	0.78
43	0.83	0.36	F	2.9 (...)		53 (<290)	0.68	0.29	1.6
44	0.42	0.05	T	0.7 (0.5-1.0)		0.7 (<5)	2.0	0.86	0.88
45	–0.97	0.51	L	5.1 (>2.4)		9 (<45)	0.093	0.040	0.29
45	–0.97	0.51	L		0.6 (0.2-2.1)	10 (<31)	0.096	0.041	0.41
46	–0.06	0.18	J	4.0 (1.8-8.9)		27 (0.7-92)	0.21	0.091	0.86
47	0.37	0.02	H	0.8 (0.7-0.9)		1 (<2)	12	5.2	5.2
48	–0.06	0.27	L	1.3 (0.2-4.1)		0 (<14)	0.12	0.052	0.052
49	0.36	0.03	R	0.7 (0.5-0.9)		0 (<1)	9.1	3.9	3.9
50	0.20	0.11	J	1.8 (1.1-2.8)		6 (<19)	0.49	0.21	0.28
51	0.51	0.10	G	0.4 (0.1-1.0)		0.02 (<10)	2.7	1.2	1.2
52	–0.05	0.09	G	1.5 (1.2-1.8)		0 (<2)	0.44	0.19	0.19
52			T				1.4	0.60	0.60
53	–0.01	0.11	L	2.1 (1.6-2.7)		0 (<2)	0.21	0.091	0.091
53			R				0.24	0.10	0.10
54	0.11	0.17	J	2.4 (1.3-4.1)		11 (<36)	0.18	0.078	0.15
55	–0.06	0.31	G	5.3 (>2.1)		35 (5-110)	0.13	0.056	2.6
56	0.48	0.05	L	1.1 (0.9-1.4)		8 (4-14)	1.1	0.48	0.56
56			R				2.2	0.95	1.1
57	0.17	0.14	J	1.4 (0.9-2.4)		2 (<13)	0.47	0.20	0.22
58	–0.02	0.17	J	1.7 (1.2-3.2)		0 (<17)	0.35	0.15	0.15
59	0.15	0.12	G	1.6 (0.9-2.6)		4 (<15)	0.42	0.18	0.21
60	–0.09	0.18	U	2.2 (1.5-3.5)		0 (<10)	0.20	0.086	0.086
61	0.36	0.04	G	0.8 (0.6-1.0)		0.7 (<4)	2.5	1.1	1.1
61			T				4.4	1.9	1.9
62	0.24	0.20	J	1.8 (0.7-4.1)		7 (<37)	0.62	0.27	0.36
63	1.00	0.29	G	2.6 (0.2-6.0)		89 (29-230)	0.70	0.30	1.4
64	0.20	0.12	G	1.5 (1.0-2.3)		2 (<12)	0.34	0.15	0.16
65	0.25	0.09	G	1.0 (0.7-1.5)		0 (<5)	0.75	0.32	0.32
66	–0.68	0.10	G		0.9 (0.6-1.7)	1 (<3)	0.30	0.13	0.17
67	0.34	0.01	B	0.51 (0.46-0.56)	0.15 (0.14-0.17)	0 (<1)	240	100	100
68	0.07	0.20	U	1.7 (0.9-3.7)		0.02 (<12)	0.13	0.056	0.056
69	1.00	0.77	M	1.4 (>–0.6)		28 (<910)	0.42	0.18	0.27
70	0.44	0.29	U	0.8 (–0.1-3.4)		0 (<64)	0.15	0.065	0.065
71	–0.09	0.10	R	1.6 (1.3-2.1)		0 (<3)	0.84	0.36	0.36

(Continuing to the next page.)

Table 5.5: Final ASCA catalogue of discrete X-ray sources in the SMC region
 – III. Spectral parameters (continued from the previous page).

No.	HR	HRerr	Obs. ID	Γ	kT	N_{H}	F_{X}	L_{obs}	L_{X}
72	-0.37	0.12	G	3.2 (2.4-4.7)		3 (<11)	0.36	0.16	0.23
73	0.32	0.11	U	1.4 (0.9-2.1)		2 (<11)	0.37	0.16	0.17
74	0.43	0.05	B	0.7 (0.5-0.9)		0.4 (<4)	1.5	0.65	0.65
74			D				1.6	0.69	0.69
74			G				1.7	0.73	0.73
75	0.34	0.32	R	0.4 (-1.1-2.5)		2 (<62)	0.52	0.22	0.23
76	0.19	0.13	D	1.9 (1.2-2.7)		9 (2-19)	0.46	0.20	0.28
76			G				0.36	0.16	0.22
77	0.14	0.39	U	1.4 (0.0-5.4)		3 (<740)	0.12	0.052	0.056
78	0.36	0.06	B	0.8 (0.6-1.0)		0 (<4)	1.3	0.56	0.56
78			D				1.1	0.48	0.48
78			G				0.79	0.34	0.34
79	0.66	0.11	M	2.4 (0.5-4.4)		110 (13-210)	0.67	0.29	1.3
80	-0.37	0.13	M	2.6 (2.0-4.4)		0.4 (<9)	0.59	0.25	0.27
81	-0.86	0.01	B		— see section 6.3.4 —		14	6.0	7.3
82	-0.88	0.04	D		1.0 (0.8-1.5)	0 (<0.3)	1.0	0.43	0.43
83	-0.20	0.08	D	2.2 (1.9-2.6)		0 (<2)	0.30	0.13	0.13
84	-0.28	0.12	D	2.6 (2.1-3.5)		0 (<3)	0.16	0.069	0.069
85	D
86	0.16	0.11	D	1.3 (0.9-2.0)		0.3 (<8)	0.38	0.16	0.16
87	0.68	0.35	D	4.2 (1.5-9.7)		51 (12-150)	0.19	0.082	1.8
88	N
89	N
90	0.33	0.003	I	0.79 (0.76-0.82)	0.144 (0.137-0.150)	2.3 (1.6-3.0)	370	160	170
91	0.31	0.26	N	2.0 (>1.0)		2 (<160)	0.11	0.048	0.052
92	-0.08	0.21	N	1.4 (0.6-2.7)		0 (<8)	0.23	0.099	0.099
93	0.36	0.23	N	1.3 (0.6-3.1)		0 (<20)	0.17	0.073	0.073
94	0.43	0.01	A	0.69 (0.61-0.76)	0.13 (0.11-0.15)	4 (2-6)	220	95	110
94	0.40	0.02	C	0.45 (0.35-0.53)	0.20 (0.13-0.29)	0 (<2)	8.9 [†]	3.8 [†]	3.8 [†]
94	0.44	0.01	I	0.35 (0.27-0.44)	0.16 (0.13-0.19)	2 (<4)	150	65	67
95	-0.43	0.09	C	3.3 (2.8-3.9)		0 (<1)	0.38	0.16	0.16
96	-0.36	0.13	V	2.6 (2.0-4.0)		1 (<10)	0.68	0.29	0.34
97	0.24	0.18	V	0.6 (-0.1-1.2)		0 (<12)	0.35	0.15	0.15
98	0.41	0.20	V	1.2 (0.5-2.5)		3 (<21)	0.37	0.16	0.18
99	1.00	0.74	V	5.2 (>1.9)		110 (29-290)	0.44	0.19	31
100	0.11	0.07	V	2.4 (1.8-3.1)		8 (3-16)	0.41	0.18	0.30
101	-0.22	0.18	V	2.1 (1.3-4.3)		1 (<14)	0.45	0.19	0.21
102	0.63	0.17	V	1.9 (0.8-3.6)		24 (5-59)	0.99	0.43	0.78
103	0.18	0.11	O	1.2 (0.9-1.6)		0 (<4)	1.8	0.78	0.78
104	0.20	0.10	O	1.1 (0.8-1.8)		0 (<8)	1.7	0.73	0.73
105	-0.06	0.12	O	2.8 (1.7-4.8)		7 (<20)	0.34	0.15	0.29
106	-0.21	0.31	O	6.6 (>1.8)		29 (<88)	0.14	0.060	6.5

Chapter 6

Comments on Specific Sources and Pulsar Statistics

6.1 X-Ray Pulsars

6.1.1 Overview

Figure 6.1 shows the history of discoveries of X-ray pulsars in the SMC. As is easily recognized, there have recently been a rush of pulsar discoveries, and the total number has already exceeded 20. The contribution from this study to the discoveries and position determination of pulsars (stars and circles in figure 6.1) is rather large, thanks to the high sensitivity in the high energy band, fine time resolution, and imaging capability of ASCA.

Here we give brief comments on all the pulsars, including their spectra, pulse profiles, optical counterparts, and flux variability. Pulse profiles are shown in 0.7–2.0 keV and 2.0–7.0 keV for most sources, while for the remainder different energy bands are chosen for purposes peculiar to each source. We regard a pulsar as an XBP if the pulsar has a long pulse period (~ 1 –1000 s), hard spectrum ($\Gamma \sim 1$), flux variability, and/or an optical counterpart. We ultimately classified at least 22 out of the 25 pulsars as XBPs¹. Basic properties are summarized in table 6.1. In this section, pulse periods are designated with the error for the last digit in parentheses. The significance of pulse detection with FFT analysis is defined by

¹AX J0043–737, AX J0049–732, and AX J0105–722 are not included in the 22 because further confirmation is needed for them.

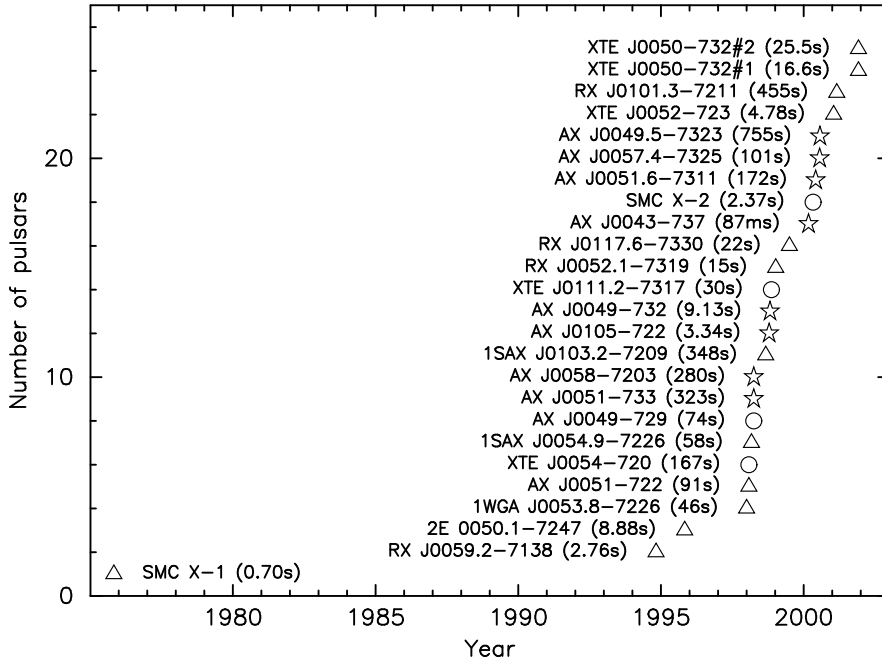


Figure 6.1: History of discoveries of X-ray pulsars in the SMC as of December, 2001. The symbols represent the pulsars discovered in this study (stars), the pulsars for which only the positions were determined in this study (circles), and the remainder (triangles).

$1 - P_{\text{RND}}$, where P_{RND} is the probability that the maximum power is attributed to randomly distributed events. For the maximum power P_{max} obtained in a PSD, P_{RND} is calculated by

$$P_{\text{RND}} = N \int_{P_{\text{max}}}^{\infty} p_2(\chi^2) d\chi^2, \quad (6.1)$$

where N and $p_2(\chi^2)$ represent the number of frequencies in the PSD and the χ^2 probability density for 2 degrees of freedom, respectively (e.g., Leahy et al. 1983).

6.1.2 No. 17 — AX J0043-737

Coherent pulsations of a 87.58073(4) ms period from No. 17 (AX J0043-737) were discovered by Yokogawa & Koyama (2000) in obs. K, using a timing resolution of 31.25 ms (1/16 of the nominal value) as described in section 5.3. The PSD derived from the events in 0.5-7.7 keV is shown in figure 6.2 (a). The maximum power of 47.3 indicates that the significance of the pulse detection is at a marginal level, $\sim 99.98\%$. The pulse profile in the same energy band

Table 6.1: X-ray pulsars in the SMC.

No.	Name	Period (s)*	Optical Identification	References
17	AX J0043–737 [†]	0.08758073(4)	...	1
24	AX J0049–729	74.68(2)	Be	2, 3, 4, 5
26	AX J0049–732	9.1320(4)	... [‡]	6, 7, 8
30	AX J0049.5–7323	755.5(6)	Be?	9, 10, 11
...	XTE J0050–732#1	[16.6]	...	12
...	XTE J0050–732#2	[25.5]	...	12
32	AX J0051–733	323.2(5) - obs. F 321.0(1) - obs. Q	Be	5, 13, 14, 15
37	AX J0051–722	91.12(5)	Be	2, 4, 16
40	AX J0051.6–7311	172.40(3)	Be	15, 17, 18
...	2E 0050.1–7247	[8.8816(2)]	Be	4, 19
...	XTE J0052–723	[4.782(1)]	...	20
43	RX J0052.1–7319	[15.3(1)]	Be	21, 22, 23
44	XTE J0054–720	167.8(2)	Be	15, 24, 25
47	1WGA J0053.8–7226	46.63(4)	Be	2, 26
49	SMC X-2	2.37230(4)	Be	27, 28, 29, 30
51	XTE J0055–724	[58.963(3)]	Be	4, 5, 31, 32, 33
56	AX J0057.4–7325	101.45(7) - obs. R 101.47(6) - obs. L	...	28, 34
61	AX J0058–7203	280.4(4)	Be?	11, 13, 35
67	RX J0059.2–7138	2.763221(4) [§]	Be	36, 37, 38
74	RX J0101.3–7211	[455(2)]	Be	39
78	1SAX J0103.2–7209	348.9(3)	Be	5, 40, 41, 42
83	AX J0105–722 [†]	3.34300(3)	... [‡]	43, 44
90	XTE J0111.2–7317	30.9497(4)	Be	22, 45, 46, 47
94	SMC X-1	0.70865(6) - obs. A 0.7065(5) - obs. I	B (SG) [¶]	48, 49
...	RX J0117.6–7330	[22.0669(1)]	Be	50, 51

Note — Pulsars in this table are mostly regarded as XBPs, except for AX J0043–737, AX J0049–732, and AX J0105–722 (see text).

References — (1) Yokogawa & Koyama 2000; (2) Corbet et al. 1998; (3) Yokogawa et al. 1999; (4) Stevens, Coe, & Buckley 1999; (5) Coe & Orosz 2000; (6) Imanishi, Yokogawa, & Koyama 1998; (7) Ueno et al. 2000a; (8) Filipović, Pietsch, & Haberl 2000; (9) Ueno et al. 2000b; (10) Yokogawa et al. 2000a; (11) Haberl & Sasaki 2000; (12) Lamb et al. 2001; (13) Yokogawa & Koyama 1998a; (14) Imanishi et al. 1999; (15) Cowley et al. 1997; (16) Ozaki et al. 2000; (17) Torii et al. 2000a; (18) Yokogawa et al. 2000b; (19) Israel et al. 1997; (20) Corbet, Marshall, & Markwardt 2001; (21) Lamb et al. 1999; (22) Israel et al. 1999; (23) Kahabka 2000; (24) Lochner et al. 1998; (25) Yokogawa et al. 2001a; (26) Buckley et al. 2001; (27) Corbet et al. 2001; (28) Torii et al. 2000b; (29) Yokogawa et al. 2001b; (30) Murdin et al. 1979; (31) Marshall & Lochner 1998; (32) Santangelo et al. 1998; (33) Israel et al. 1998b; (34) Yokogawa et al. 2000c; (35) Tsujimoto et al. 1999; (36) Hughes 1994; (37) Kohno, Yokogawa, & Koyama 2000; (38) Southwell & Charles 1996; (39) Sasaki et al. 2001; (40) Israel et al. 2000; (41) Hughes & Smith 1994; (42) Ye et al. 1995; (43) Yokogawa & Koyama 1998b; (44) Filipović et al. 2000; (45) Chakrabarty et al. 1998a; Wilson & Finger 1998; (46) Yokogawa et al. 2000d; (47) Coe, Haigh, & Reig 2000; (48) Lucke et al. 1976; (49) Petro, Feldman, & Hiltner 1973; (50) Coe et al. 1998; (51) Macomb et al. 1999

*: The periods determined in this work are presented with the error for the last digit in parentheses. Correction for the orbital Doppler effect was carried out only for SMC X-1. Periods in square brackets were determined by others and not detected in this work.

†: Care must be taken for these pulsars. See section 6.1.2 and section 6.1.19.

‡: AX J0049–732 and AX J0105–722 were once respectively identified with ROSAT sources RX J0049.4–7310 and RX J0105.1–7211 (Filipović, Pietsch, & Haberl 2000; Filipović et al. 2000). Since these ROSAT sources have emission line objects as counterparts, it was previously proposed that AX J0049–732 and AX J0105–722 were Be/X-ray binaries. However, according to the improved positions determined in this study, the identification with the ROSAT sources is now a little questionable (see table 5.3, section 6.1.4, and section 6.1.19).

§: Determined by a detailed pulse phase analysis (Kohno, Yokogawa, & Koyama 2000).

¶: A supergiant (B0I), Sk160.

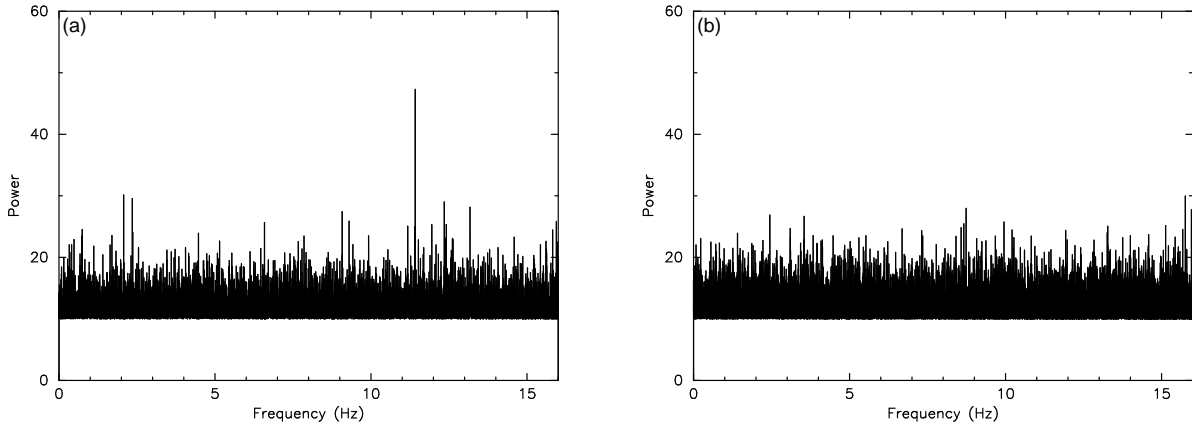


Figure 6.2: PSDs of AX J0043–737 in (a) obs. K and (b) obs. P, obtained from the events in 0.5–7.7 keV. Data points with a power less than 10 are not plotted. The peak detected in (a) is not found in (b).

is shown in figure 6.3. AX J0043–737 was also detected in a follow-up observation with a longer exposure time (obs. P). We performed the FFT on the events in the same energy band. However, as shown in figure 6.2 (b), no significant peak was found as in the previous observation. Although events in different energy bands were also used for the FFT analysis, we again detected no significant peak in the PSDs.

The count rate, total count (without background), and background level in 0.5–7.7 keV are 2.5×10^{-3} cnt s $^{-1}$, 200 cnt, and 64% in obs. K, and 1.0×10^{-3} cnt s $^{-1}$, 186 cnt, and 84% in obs. P. Although the total count is nearly identical in these two observations, the smaller count rate and larger background level in obs. P may have caused the pulsations to be hidden in the background. Therefore, confirmation of the pulsations by observations with a much higher S/N ratio is still needed.

The spectral shape (Γ and N_{H}) is consistent between the two observations, while F_{X} shows a slight decline (table 6.2). The photon index is softer than those for usual XBPs ($\Gamma \sim 1$; e.g., Nagase 1989). A short pulse period, soft spectrum, and luminosity far smaller than the Eddington limit for a neutron star are also detected from SAX J0635+0533, which has a Be star counterpart ($P = 33.8$ ms and $\Gamma = 1.50$; Kaaret et al. 1999; Cusumano et al. 2000). Cusumano et al. (2000) argue that SAX J0635+0533 may be an accretion-powered Be/X-ray binary, and if so, the magnetic field should be weaker than 2×10^9 G for the

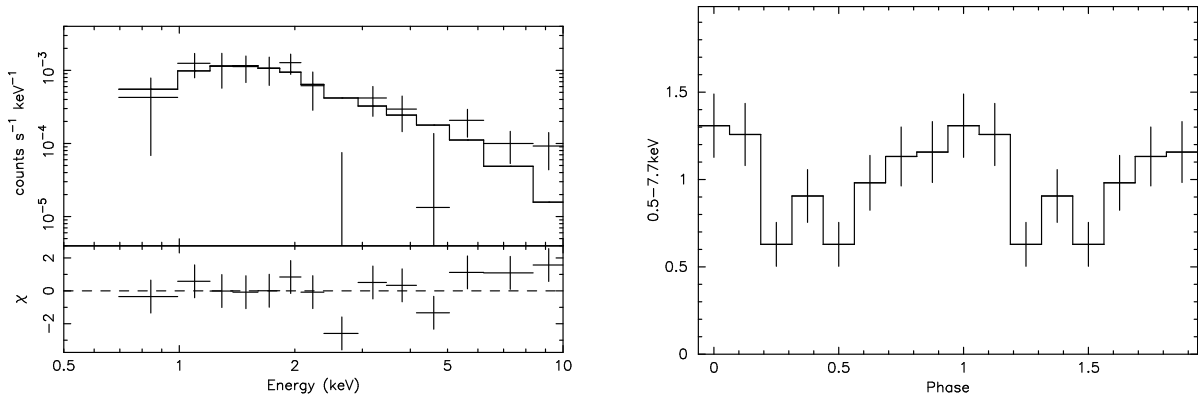


Figure 6.3: GIS spectrum (left) and pulse profile (right) of AX J0043–737. (Left) The crosses are data points obtained in obs. K, while the solid line represents the best-fit model derived from the simultaneous fitting. (Right) Pulse profile in obs. K obtained from 0.5–7.7 keV.

Table 6.2: Spectral parameters for AX J0043–737 taken from table 5.5.

HR	HRerr	Obs. ID	Γ	N_{H}	F_{X}	L_{X}
-0.16	0.15	K	1.7 (1.3–2.4)	0 (< 4)	0.20	0.086
		P			0.11	0.048

Note — See page 55 for legends.

accretion to occur against the centrifugal force at the magnetosphere.

Since no optical counterpart has been reported for AX J0043–737, we investigated the catalogues of emission line objects (potential candidates for Be stars) by Meyssonier & Azzopardi (1993) and Murphy & Bessell (2000), but no counterpart was found. Therefore, a search for the optical counterpart is needed, in addition to confirmation of the 87-ms pulsations.

6.1.3 No. 24 — AX J0049–729

Coherent pulsations with a 74.8(4) s period were first discovered with RXTE (Corbet et al. 1998) in the direction of SMC X-3. However, the very large positional uncertainty (\sim

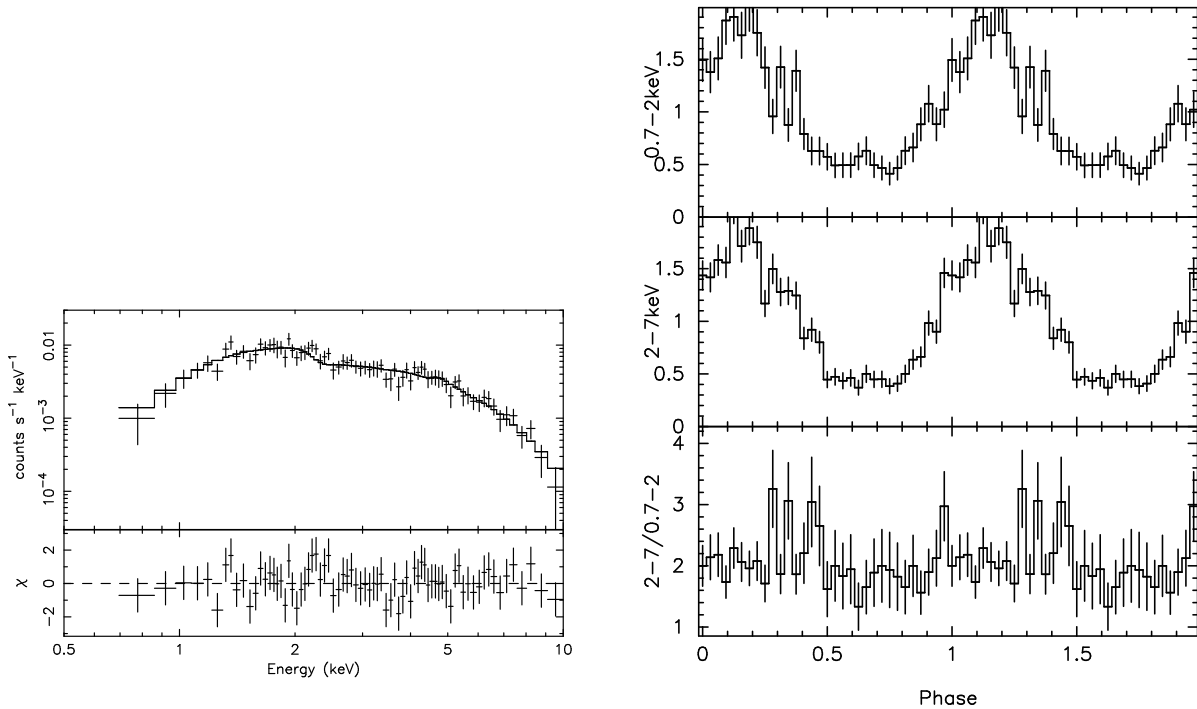


Figure 6.4: GIS spectrum (left) and pulse profiles (right) of AX J0049–729. (Left) The crosses are data points obtained in obs. F, while the solid line represents the best-fit model derived from the simultaneous fitting. (Right) Pulse profiles in obs. F obtained from 0.7–2.0 keV and 2.0–7.0 keV, and their ratio.

Table 6.3: Spectral parameters for AX J0049–729 taken from table 5.5.

HR	HRerr	Obs. ID	Γ	N_{H}	F_{X}	L_{X}
0.36	0.03	F	1.0 (0.8–1.1)	3 (2–5)	12	5.5
		H			1.6	0.76
		Q			0.71	0.33

Note — See page 55 for legends.

2°) hampered identification with other sources. During this study, we found that No. 24 (AX J0049–729) was pulsating with a 74.68(2) s period in obs. F (Yokogawa et al. 1999) and so determined its position much more accurately. The ROSAT counterpart of this pulsar, RX J0049.1–7250, provides the most accurate position with a $\pm 13''$ error circle (Kahabka &

Pietsch 1998), in which one Be star has been discovered (Stevens, Coe, & Buckley 1999). This pulsar has been included in 11 observation fields of Einstein, ROSAT, and ASCA. Yokogawa et al. (1999) found a large flux variability of a factor $\gtrsim 100$ during those observations. From all the information, we conclude that AX J0049–729 is an XBP with a Be star companion (hereafter, a Be-XBP).

6.1.4 No. 26 — AX J0049–732

Coherent pulsations with a 9.1320(4) s period from No. 26 (AX J0049–732) were first detected during this study in the following manner. Using the data of obs. F, we performed an FFT on the events in 1.0–5.1 keV collected from a 3′-radius circle centered on AX J0049–732, and discovered the coherent pulsations with 99.99% confidence (Imanishi, Yokogawa, & Koyama 1998; Ueno et al. 2000a). However, since AX J0049–732 is detected at only $\sim 1'.8$ from No. 25 (SNR 0047–735), mutual contamination was not negligible due to the poor resolution of the ASCA XRT. Therefore, we also performed an FFT on the events in a 3′-radius circle centered on SNR 0047–735, and detected no pulsations. These analyses clearly indicate that the 9.13-s pulsations are attributable to AX J0049–732.

AX J0049–732 was also detected in obs. Q. However, in this observation another source, No. 27, was detected at $\sim 1'.3$ from AX J0049–732, in addition to SNR 0047–735 at $\sim 1'.8$. The SIS data were used to resolve these sources and determine the spectral parameters, but were not used for an FFT analysis because the timing resolution (8 s) is insufficient to detect the ~ 9 -s pulsations. We therefore used the GIS data for an FFT analysis, although No. 27 and AX J0049–732 were not resolved. We collected photons from a 3′-radius circle centered on AX J0049–732 and performed the FFT analysis, but no significant pulsations were detected. This is probably due to the poor statistics caused by the reduced flux of AX J0049–732 and large contamination from No. 27, which has the same flux level as AX J0049–732 (see table 5.5). Therefore, a follow-up observation with better spatial resolution is needed to confirm the pulsations from AX J0049–732.

Filipović, Pietsch, & Haberl (2000) found two ROSAT sources near AX J0049–732, RX J0049.2–7311 and RX J0049.5–7310 (No. 430 and No. 427 in Haberl et al. 2000, respectively). Since RX J0049.2–7311 has an emission line object as a counterpart while RX J0049.5–7310 does not, Filipović, Pietsch, & Haberl (2000) suggest that RX J0049.2–7311 is likely to be the counterpart for AX J0049–732. However, according to the updated po-

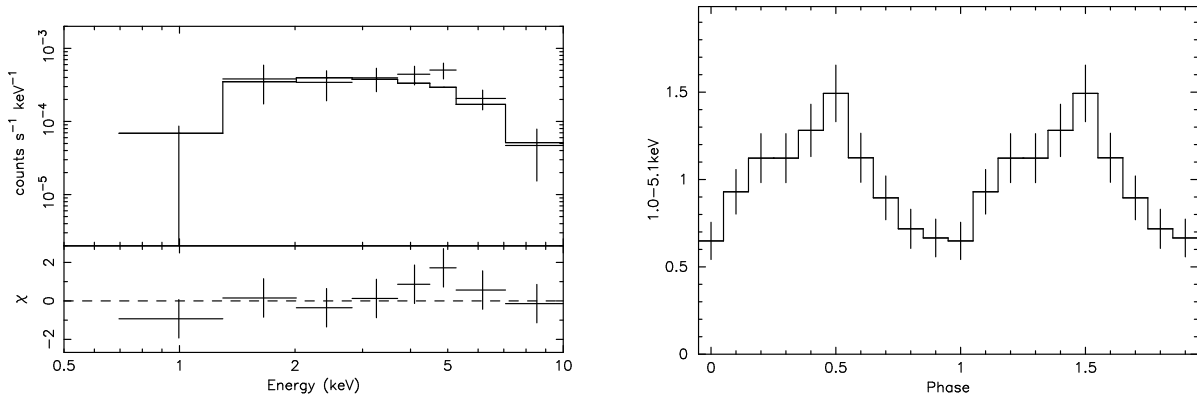


Figure 6.5: GIS spectrum (left) and pulse profile (right) of AX J0049–732. (Left) The crosses are data points obtained in obs. F, while the solid line represents the best-fit model derived from the simultaneous fitting. (Right) Pulse profile in obs. F obtained from 1.0–5.1 keV.

Table 6.4: Spectral parameters for AX J0049–732 taken from table 5.5.

HR	HRerr	Obs. ID	Γ	N_{H}	F_{X}	L_{X}
0.85	0.20	F	0.9 (0.3–1.6)	15 (6–28)	0.64	0.33
		Q			0.37	0.19

Note — See page 55 for legends.

sition of the ASCA source, the separation between AX J0049–732 and RX J0049.2–7311 is $\sim 80''$, which is much larger than the improved positional accuracy for ASCA sources (see section 5.2.1). Therefore, the identification made by Filipović, Pietsch, & Haberl (2000) is now questionable. On the other hand, the separation between RX J0049.5–7310 and AX J0049–732 is $\sim 33''$, thus we regard this source as the counterpart.

6.1.5 No. 30 — AX J0049.5–7323

Coherent pulsations with a 755.5(6) s period from No. 30 (AX J0049.5–7323) were first discovered during this study from the data of obs. Q (Ueno et al. 2000b; Yokogawa et al. 2000a). The energy resolved pulse profiles are shown in figure 6.6. The pulse shape is rather spiky in 1.2–2.0 keV and nearly sinusoidal in 2.0–5.5 keV, while photons above 5.5 keV do

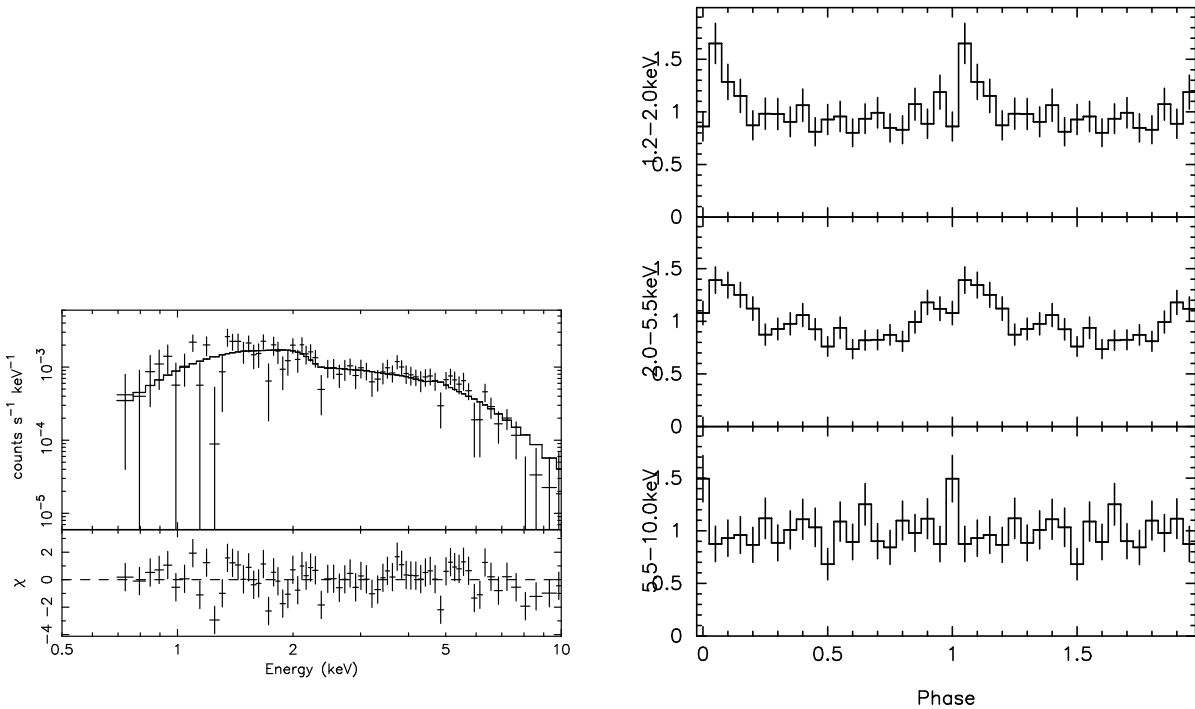


Figure 6.6: GIS spectrum (left) and pulse profiles (right) of AX J0049.5–7323. (Left) The crosses are data points obtained in obs. Q, while the solid line represents the best-fit model derived from the simultaneous fitting. (Right) Pulse profiles in obs. Q obtained from 1.2–2.0 keV, 2.0–5.5 keV, and 5.5–10.0 keV.

Table 6.5: Spectral parameters for AX J0049.5–7323 taken from table 5.5.

HR	HRerr	Obs. ID	Γ	N_{H}	F_{X}	L_{X}
0.31	0.06	F	0.8 (0.7–1.0)	0 (< 3)	1.1	0.48
		L			1.5	0.65
		Q			1.7	0.73

Note — See page 55 for legends.

not exhibit definite pulsations. The smaller pulsed fraction at higher energy is also seen in RX J0101.3–7211 (section 6.1.17).

AX J0049.5–7323 was also detected in obs. F and obs. L with nearly the same flux level

(see table 6.5), but the pulsations were not detected in those observations. It may be due to the much better statistics of the data in obs. Q, which has a much longer exposure time (177 ks) than obs. F and obs. L (~ 40 ks; see table 4.1). Otherwise, it may imply a smaller pulsed fraction in obs. F and obs. L. To examine the former possibility, we divided the obs. Q data into four segments with equal exposure times (~ 44 ks), and performed an FFT analysis and epoch folding on each segment. Since no significant pulsations were detected from any of the segments, we conclude that the very long exposure time was essential for the pulse detection.

AX J0049.5–7323 has been covered by 19 observations of ROSAT and Einstein. Yokogawa et al. (2000a) investigated these archival data and found that AX J0049.5–7323 has shown a flux variation with a factor of at least ~ 10 . All the information indicates that AX J0049.5–7323 is an XBP. In addition, it has been proposed that the ROSAT counterpart, RX J0049.7–7323, is a Be/X-ray binary because an emission line object exists in the error circle of $\sim 15''$ -radius (Haberl & Sasaki 2000). An optical spectroscopy of the emission line object is encouraged to examine whether it is a Be star or not.

6.1.6 No. 32 — AX J0051–733

Coherent pulsations with a 323.2(5) s period from No. 32 (AX J0051–733) were first discovered during this study from the data of obs. F. and reported by Yokogawa & Koyama (1998a) and Imanishi et al. (1999). New results were obtained from a long follow-up observation (obs. Q): AX J0051–733 was detected at a larger flux (see table 6.6) and the pulsations were detected again with a shorter period of 321.0(1) s. The GIS spectra may show a soft excess below ~ 1 keV (figure 6.7). A blackbody model with a temperature of ~ 0.1 keV could describe the excess, although the blackbody component is not necessary from a statistical point of view.

Table 6.6: Spectral parameters for AX J0051–733 taken from table 5.5.

HR	HRerr	Obs. ID	Γ	N_{H}	F_{X}	L_{X}
0.43	0.01	F	0.76 (0.69–0.83)	2.2 (1.2–3.3)	2.9	1.3
		Q			6.8	3.0

Note — See page 55 for legends.

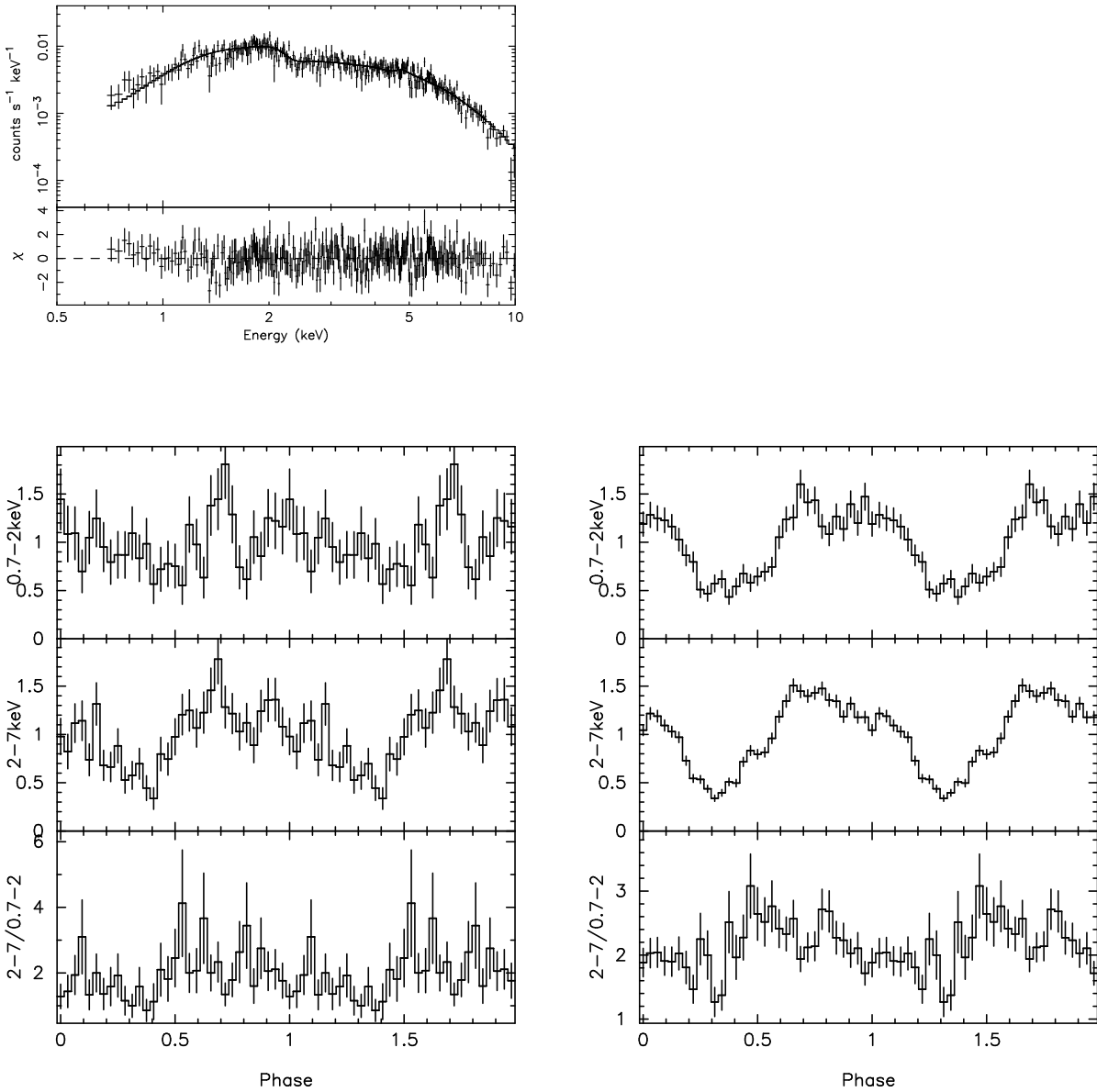


Figure 6.7: GIS spectrum (top) and pulse profiles (bottom) of AX J0051–733. (Top left) The crosses are data points obtained in obs. Q, while the solid line represents the best-fit model derived from the simultaneous fitting. (Bottom) Pulse profiles in obs. F (left) and obs. Q (right) obtained from 0.7–2.0 keV and 2.0–7.0 keV, and their ratio.

Imanishi et al. (1999) investigated 16 observations of ROSAT and Einstein by which AX J0051–733 was covered, and found a flux variability of a factor $\gtrsim 10$. In addition,

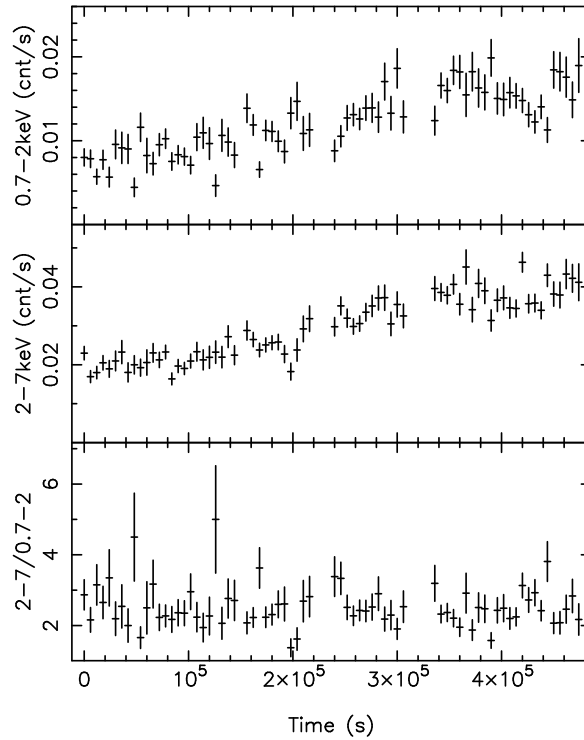


Figure 6.8: Light curves of AX J0051–733 in obs. Q with a bin time of 3000 s. The upper and middle panels present the light curves in the soft (0.7–2.0 keV) and hard (2.0–7.0 keV) bands, respectively. The lower panel shows the ratio of the two bands.

gradual flux increase with a factor of ~ 2 was found during obs. Q, as shown in figure 6.7. No change was found in the spectral hardness. The ROSAT counterpart, RX J0050.8–7316, has a Be star in its error circle (Cowley et al. 1997). All the information indicates that AX J0051–733 is a Be-XBP.

From the empirical relation between the pulse and orbital periods of Be-XBPs (Corbet 1984), the orbital period is predicted to be ~ 185 days for AX J0051–733. In fact, Imanishi et al. (1999) found weak evidence for a periodicity of ~ 185 days in the long-term X-ray flux history which could be interpreted as the orbital period. On the other hand, Coe & Orosz (2000) clearly detected a 0.708 day period from the I band data of the companion Be star. They showed that the orbital period would be 1.416 days in order for the Be star to fit within the Roche lobe. The large discrepancy between Corbet’s empirical law and the periodicity in the I band is rather problematic, and must be solved by future works.

6.1.7 No. 37 — AX J0051–722

Coherent pulsations with a ~ 92 s period were first discovered in the direction of SMC X-3 during an RXTE observation on November 15, 1997 (Marshall, Lochner, & Takeshima 1997). A TOO (Target Of Opportunity) observation with ASCA on December 12 (obs. H) revealed that there were two new pulsars, No. 37 (AX J0051–722) and No. 47 (1WGA J0053.8–7226),

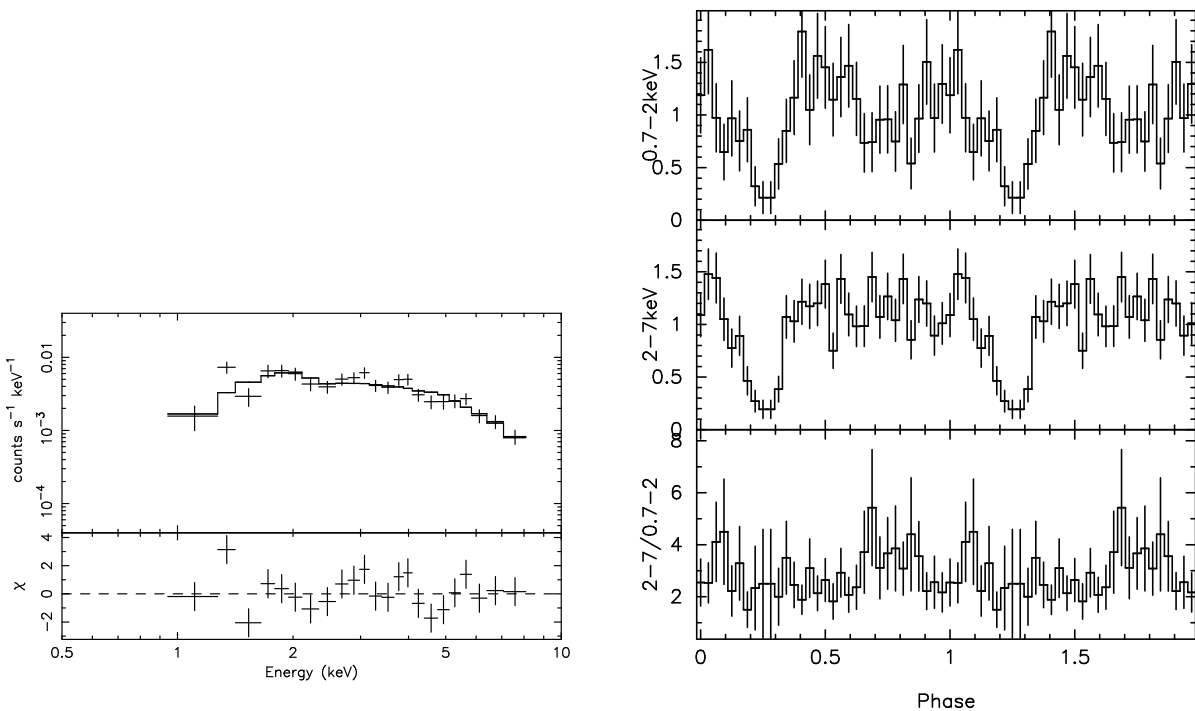


Figure 6.9: GIS spectrum (left) and pulse profiles (right) of AX J0051–722. (Left) The crosses are data points obtained in obs. H, while the solid line represents the best-fit model. (Right) Pulse profiles in obs. H obtained from 0.7–2.0 keV and 2.0–7.0 keV, and their ratio.

Table 6.7: Spectral parameters for AX J0051–722 taken from table 5.5.

HR	HRerr	Obs. ID	Γ	N_{H}	F_{X}	L_{X}
0.55	0.04	H	1.0 (0.7–1.3)	10 (5–16)	9.5	4.8

Note — See page 55 for legends.

with periods of 91.12(5) s and 46.63(4) s, respectively (Corbet et al. 1998). At first, AX J0051–722 steadily faded after its discovery, and then was found to rebrighten at the ends of March and July in 1998 (Lochner et al. 1998; Lochner 1998; Israel et al. 1998a). The spacing of these two flares and the initial outburst on 1997 November is ~ 120 days.

Stevens, Coe, & Buckley (1999) carried out optical spectroscopic observations and discovered a Be star counterpart for AX J0051–722. Thus, AX J0051–722 is classified as a Be-XBP. Therefore, the ~ 120 day spacing of X-ray flares could be interpreted as the orbital period of the neutron star in this system (Israel et al. 1998a), which is supported by the empirical law between the pulse and orbital periods (Corbet 1984).

6.1.8 No. 40 — AX J0051.6–7311

Coherent pulsations with a 172.40(3) s period from No. 40 (AX J0051.6–7311) were first discovered during this study from the data of obs. Q (Torii et al. 2000a; Yokogawa et al. 2000b). The energy resolved pulse profiles shown in figure 6.10 exhibit the energy dependence: the higher energy photons are mostly responsible for the pulsations. The GIS spectra may show a soft excess below ~ 1 keV (figure 6.10). A blackbody model with a temperature of ~ 0.18 keV compensates for the excess, although the blackbody component is not necessary from a statistical point of view.

AX J0051.6–7311 was also detected in obs. F and obs. L with a slightly different flux (see table 6.8), but the pulsations were not detected. As we did for AX J0049.5–7323 (see section 6.1.5), we divided the obs. Q data into four segments and performed an FFT analysis and epoch folding on each segment, resulting in no detection of pulsations. Therefore, we again conclude that the very long exposure time was essential for the pulse detection.

AX J0051.6–7311 has been covered by 17 observations of ROSAT and Einstein. Yokogawa et al. (2000b) investigated these archival data and found a flux variation with a factor of $\gtrsim 20$. In addition, the ROSAT counterpart, RX J0051.9–7311, has been identified with a Be star (Cowley et al. 1997). Therefore, all the information indicates that AX J0051.6–7311 is a Be-XBP.

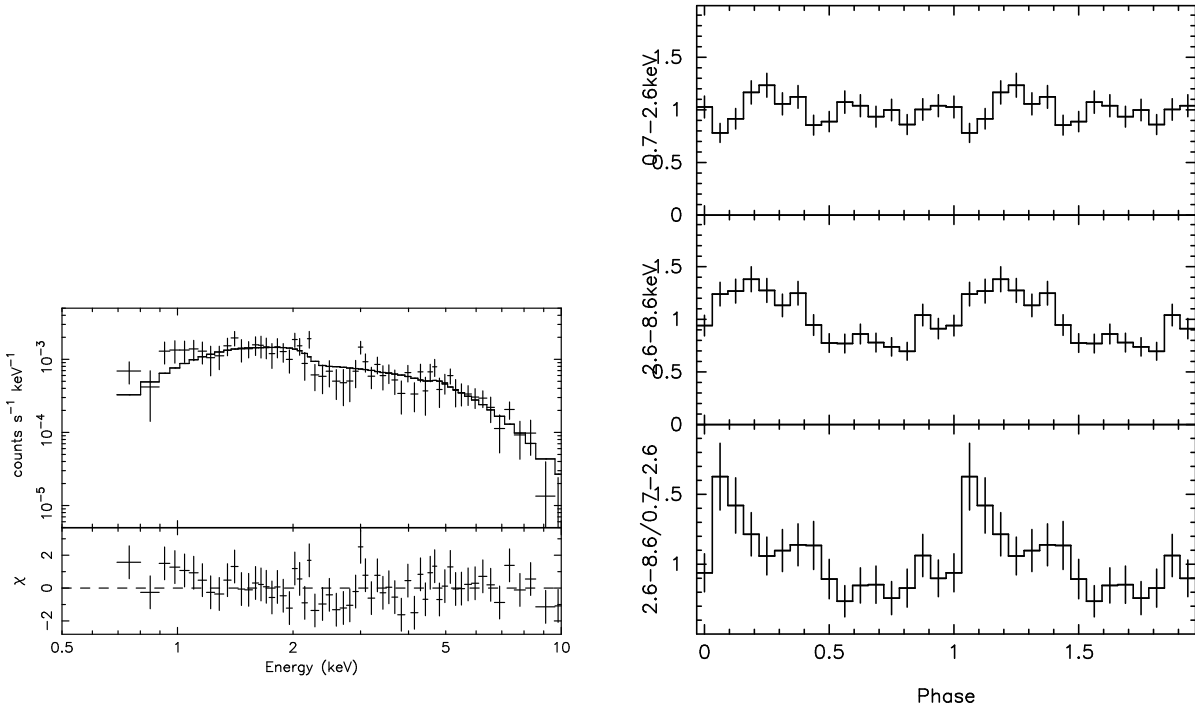


Figure 6.10: GIS spectrum (left) and pulse profiles (right) of AX J0051.6–7311. (Left) The crosses are data points obtained in obs. Q, while the solid line represents the best-fit model derived from the simultaneous fitting. (Right) Pulse profiles in obs. Q obtained from 0.7–2.6 keV and 2.6–8.6 keV, and their ratio.

Table 6.8: Spectral parameters for AX J0051.6–7311 taken from table 5.5.

HR	HRerr	Obs. ID	Γ	N_{H}	F_{X}	L_{X}
0.33	0.04	F	0.9 (0.8–1.0)	0 (< 0.8)	0.68	0.29
		L			1.5	0.65
		Q			1.3	0.56

Note — See page 55 for legends.

6.1.9 No. 43 — RX J0052.1–7319?

Coherent pulsations with a 15.3 s period from RX J0052.1–7319 were discovered in contemporaneous ROSAT and CGRO observations in 1996 (Lamb et al. 1999). Kahabka (2000)

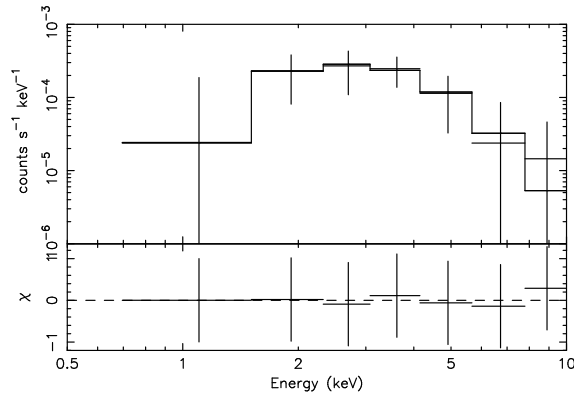


Figure 6.11: GIS spectrum of No. 43 (= RX J0052.1–7319?). The crosses are data points obtained in obs. F, while the solid line represents the best-fit model.

Table 6.9: Spectral parameters for No. 43 (= RX J0052.1–7319?) taken from table 5.5.

HR	HRerr	Obs. ID	Γ	N_{H}	F_{X}	L_{X}
0.83	0.36	F	2.9 (...)	53 (< 290)	0.68	1.6

Note — See page 55 for legends.

investigated the data of two ROSAT HRI observations in 1995 and 1996 and found a large change of flux with a factor of ~ 200 . The unabsorbed luminosities in the ROSAT band were determined to be $2.6 \times 10^{35} \text{ erg s}^{-1}$ and $5.2 \times 10^{37} \text{ erg s}^{-1}$ (in 0.1–2.4 keV; P. Kahabka 2001, private communication), assuming a photon index of 1.0 and a column density of $3 \times 10^{21} \text{ cm}^{-2}$. Israel et al. (1999) searched for an optical counterpart in the $10''$ error circle and discovered a Be star, in addition to a fainter object with an unknown spectral type. From all the information, RX J0052.1–7319 is thought to be a Be-XBP.

A faint ASCA source, No. 43, is positionally coincident with RX J0052.1–7319. The ASCA spectrum puts almost no constraint on the parameters (see table 6.9) and is consistent with Γ and N_{H} assumed by Kahabka (2000). We detected no sign of coherent pulsations from either an FFT analysis or an epoch folding search, which is probably due to the highly limited statistics. Therefore, it is not clear whether No. 43 is really the counterpart of RX J0052.1–7319.

6.1.10 No. 44 — XTE J0054–720

A new transient pulsar XTE J0054–720 was discovered with RXTE on December 17, 1997 (Lochner et al. 1998). The pulsations have persisted in observations performed through January 12, 1998, and a monotonic decrease of the pulse period from 169.30 s (December 17) to 168.40 s (January 12) was found. The flux (in 2–10 keV) initially increased from

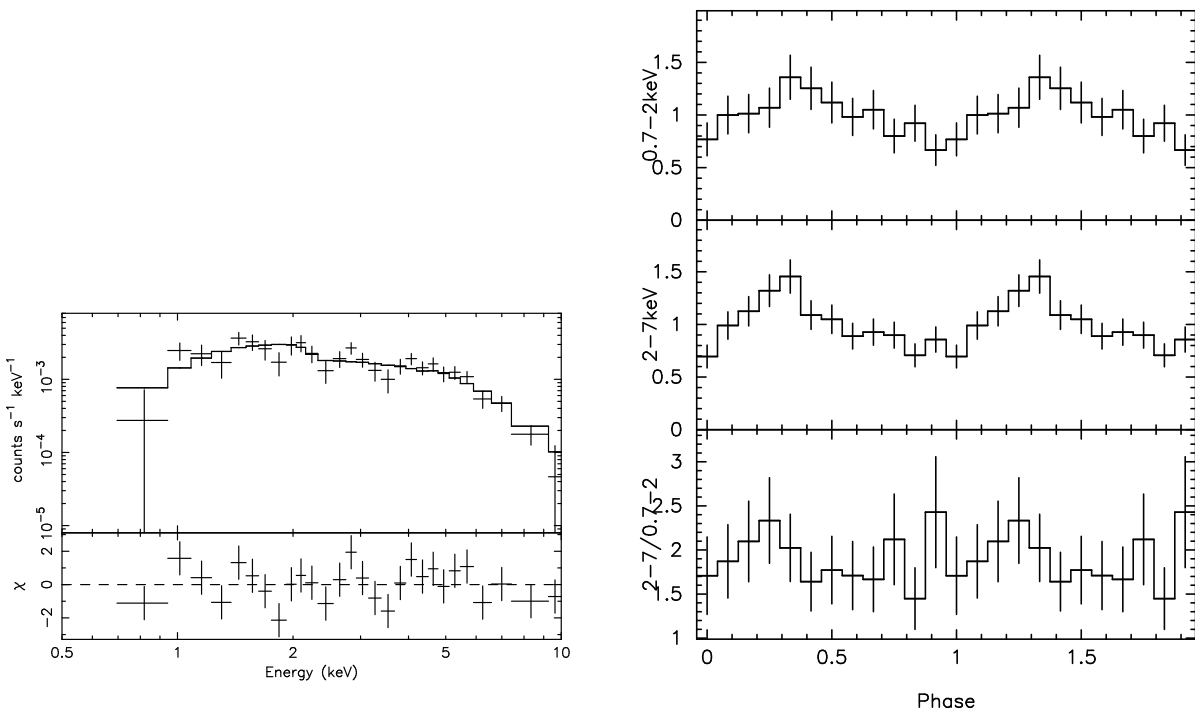


Figure 6.12: GIS spectrum (left) and pulse profiles (right) of XTE J0054–720. (Left) The crosses are data points obtained in obs. T, while the solid line represents the best-fit model. (Right) Pulse profiles in obs. T obtained from 0.7–2.0 keV and 2.0–7.0 keV, and their ratio.

Table 6.10: Spectral parameters for XTE J0054–720 taken from table 5.5.

HR	HRerr	Obs. ID	Γ	N_{H}	F_{X}	L_{X}
0.42	0.05	T	0.7 (0.5–1.0)	0.7 (< 5)	2.0	0.88

Note — See page 55 for legends.

6.0×10^{-11} erg s⁻¹ cm⁻² (December 17) to 8.3×10^{-11} erg s⁻¹ cm⁻² (December 20), and then decreased to 3.3×10^{-11} erg s⁻¹ cm⁻² (January 12).

Since the RXTE error circle was rather large (10' radius), identification with other sources has been difficult. In fact, five ROSAT HRI sources (Sasaki, Haberl, & Pietsch 2000) are located within the error circle. During this study, we detected coherent pulsations with a 167.8(2) s period from No. 44 (AX J0052.9–7157) and determined its position accurately (Yokogawa et al. 2001a). We found that AX J0052.9–7157 is located within the error circle of XTE J0054–720 and has a variable Be/X-ray binary, RX J0052.9–7158 (Cowley et al. 1997), as a counterpart. From the nearly equal pulse period and the positional coincidence, we conclude that the ASCA, ROSAT, and RXTE sources are identical, and thus XTE J0054–720 is a Be-XBP.

6.1.11 No. 47 — 1WGA J0053.8–7226 = XTE J0053–724

Coherent pulsations from No. 47 (1WGA J0053.8–7226) with a 46.63(4) s period were discovered in obs. H, as described in section 6.1.7 (Corbet et al. 1998). Buckley et al. (2001) investigated the archival data of 21 ROSAT observations and found a large flux variability. They also carried out follow-up optical and infrared observations and discovered two Be stars in the error circle. All the information indicates that 1WGA J0053.8–7226 is a Be-XBP.

Table 6.11: Spectral parameters for 1WGA J0053.8–7226 taken from table 5.5.

HR	HRerr	Obs. ID	Γ	N_{H}	F_{X}	L_{X}
0.37	0.02	H	0.8 (0.7–0.9)	1 (< 2)	12	5.2

Note — See page 55 for legends.

6.1.12 No. 49 — SMC X-2

SMC X-2 is a long-known transient Be/X-ray binary with a maximum luminosity of $\sim 10^{38}$ erg s⁻¹ (Clark et al. 1978; Murdin et al. 1979). Large outbursts have been detected with SAS-3, HEAO1, and ROSAT (Clark et al. 1978; Marshall et al. 1979; Kahabka & Pietsch 1996).

Corbet et al. (2001) detected a large outburst ($\sim 10^{38}$ erg s⁻¹) in the direction of

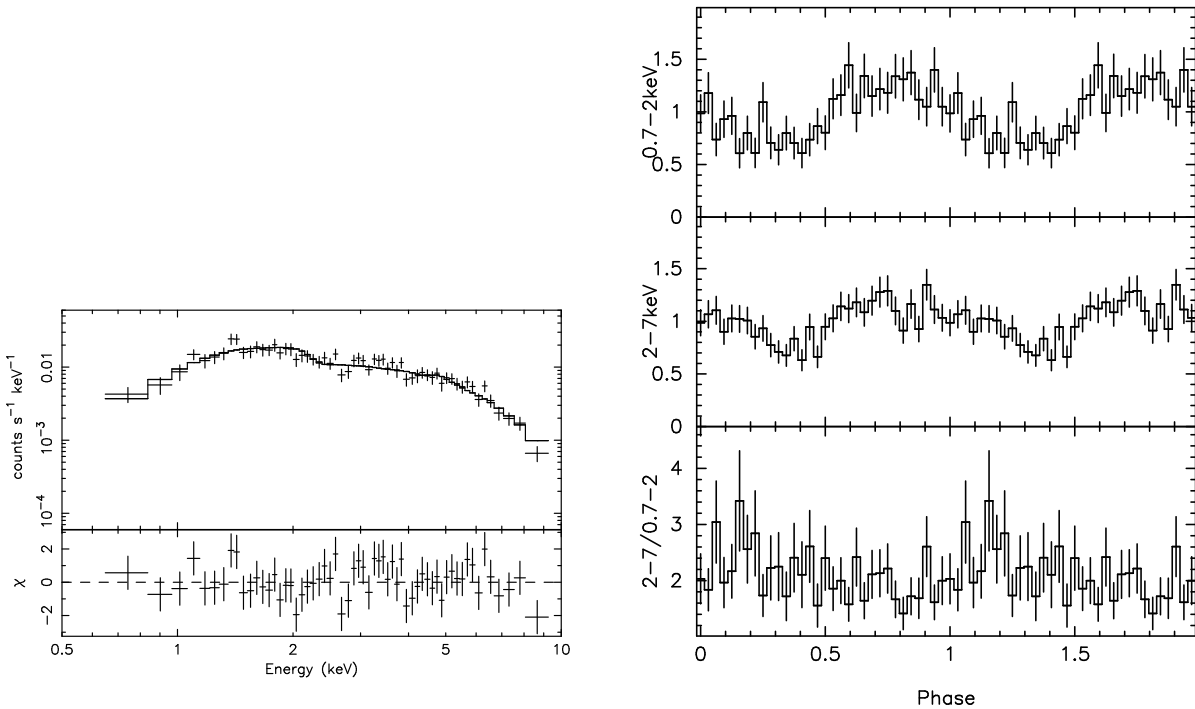


Figure 6.13: GIS spectrum (left) and pulse profiles (right) of 1WGA J0053.8–7226. (Left) The crosses are data points obtained in obs. H, while the solid line represents the best-fit model. (Right) Pulse profiles in obs. H obtained from 0.7–2.0 keV and 2.0–7.0 keV, and their ratio.

SMC X-2 in January–April, 2000, with the All-Sky Monitor onboard RXTE. The position was determined with an error radius of $3'$, and SMC X-2 is located near the edge of the error circle. Coherent pulsations were also discovered during the outburst, with periods of $2.371532(2)$ s on April 12 and $2.371861(3)$ s on April 22–23 (Corbet et al. 2001). We made a follow-up ASCA observation (obs. R) and detected No. 49 at the position of SMC X-2 with a better accuracy ($\sim 40''$; see section 5.2.1). We also detected pulsations with a $2.37230(4)$ s period (Yokogawa et al. 2001b), which is in full agreement with the RXTE result, indicating the RXTE pulsar and No. 49 are identical. Figure 6.15 shows a ROSAT PSPC image during the outburst, overlaid with error circles of SMC X-2 (determined with SAS-3), the pulsar discovered with RXTE, and the ASCA source No. 49. We find positional coincidence of these sources; hence, we conclude that the 2.37-s pulsations are attributable to the long-known transient SMC X-2.

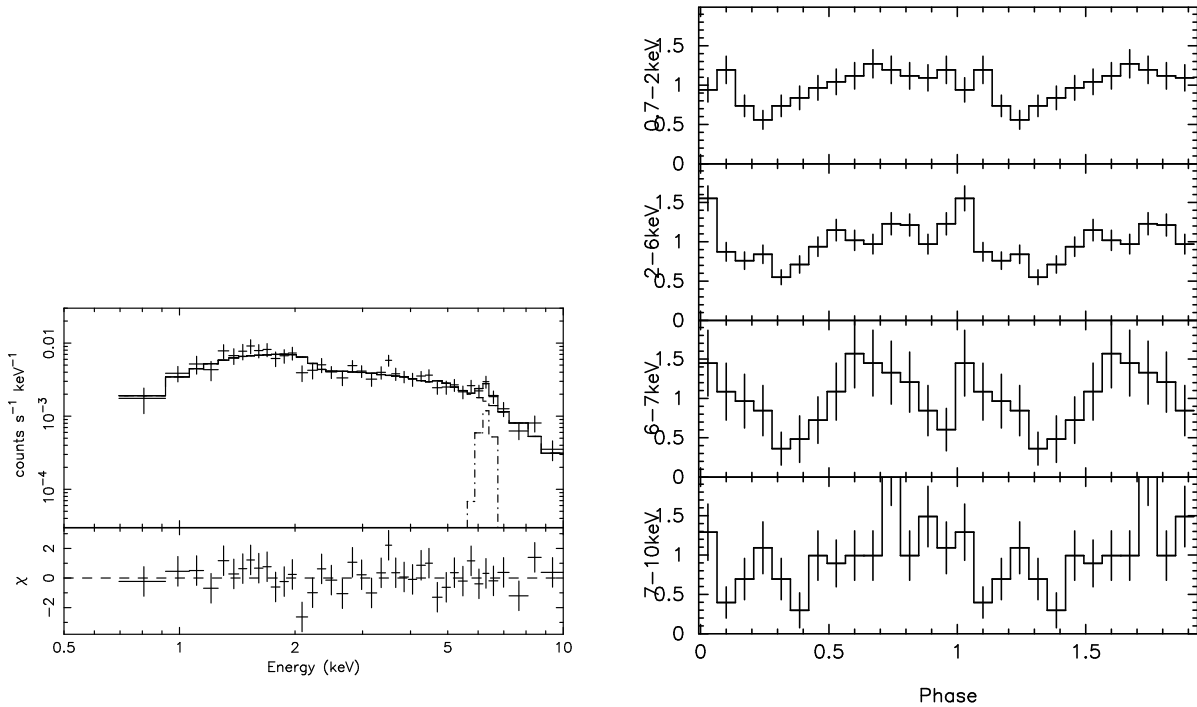


Figure 6.14: GIS spectrum (left) and pulse profiles (right) of SMC X-2. (Left) The crosses are data points obtained in obs. R, while the solid line represents the best-fit model. Spectral components are indicated by the broken lines. (Right) Pulse profiles in obs. R obtained from 0.7–2.0 keV, 2.0–6.0 keV, 6.0–7.0 keV, and 7.0–10.0 keV.

Table 6.12: Spectral parameters for SMC X-2 taken from table 5.5.

HR	HRerr	Obs. ID	Γ	N_{H}	F_{X}	L_{X}
0.36	0.03	R	0.7 (0.5–0.9)	0 (< 1)	9.1	3.9

Note — See page 55 for legends.

When fitted to a simple power-law, the ASCA spectrum showed bump-like residuals at 6–7 keV, which were eliminated by a narrow Gaussian. Adding the Gaussian component improved the χ^2 value by 7.3, which corresponds to a significance level of 97% in the F -test. The center energy and the equivalent width of the Gaussian were determined to be 6.3 (6.1–6.5) keV and 400 (150–640) eV, respectively. The center energy is consistent with the K-shell emission from neutral or low-ionization Fe. Yokogawa et al. (2001b) carried out a

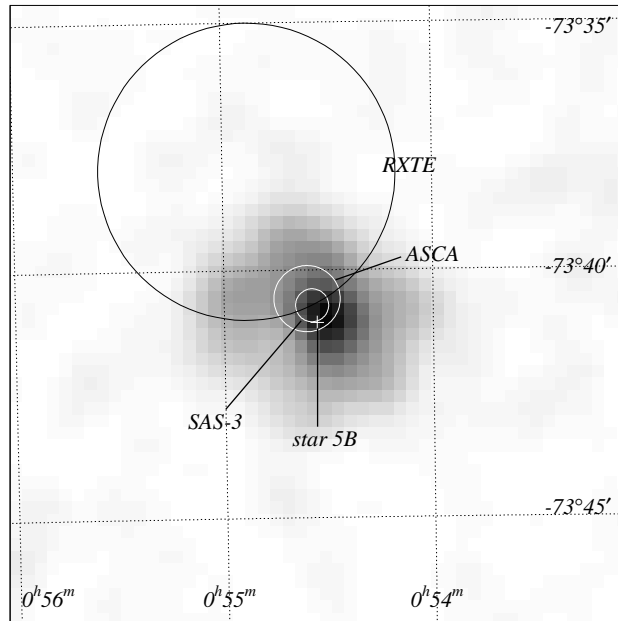


Figure 6.15: ROSAT PSPC image around SMC X-2 overlaid with error circles of SAS-3, ASCA (No. 49), and RXTE. The plus sign indicates the position of the proposed optical counterpart (“star 5B” in Murdin et al. 1979)

pulse phase resolved spectroscopy and found marginal evidence for pulsations of the Fe line intensity.

6.1.13 No. 51 — XTE J0055–724 = 1SAX J0054.9–7226

A scan observation made with RXTE on 1998 January 20 revealed a new X-ray pulsar, XTE J0055–724, with a pulse period of ~ 59 s (Marshall & Lochner 1998). Santangelo et al. (1998) made a follow-up observation with BeppoSAX on January 28, and detected pulsations with a 58.963(3) s period from 1SAX J0054.9–7226, which is located within the 10′ error circle of XTE J0055–724. The agreement of the period and position indicates that XTE J0055–724 and 1SAX J0054.9–7226 are the same source. During this study, we detected weak evidence for the ~ 59 s pulsations from No. 51 (see figure 5.6), which is positionally coincident with 1SAX J0054.9–7226; hence, we consider No. 51 to be the counterpart for this pulsar.

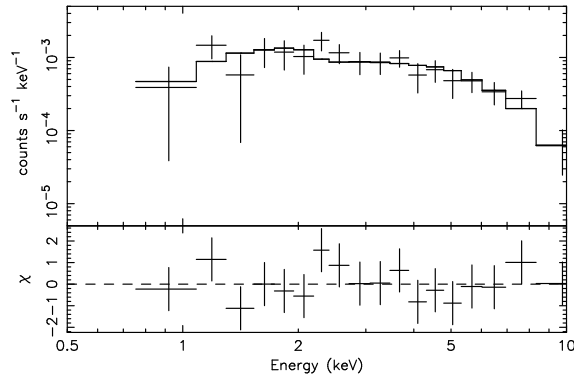


Figure 6.16: GIS spectrum of XTE J0055–724. The crosses are data points obtained in obs. G, while the solid line represents the best-fit model.

Table 6.13: Spectral parameters for XTE J0055–724 taken from table 5.5.

HR	HRerr	Obs. ID	Γ	N_{H}	F_{X}	L_{X}
0.51	0.10	G	0.4 (0.1–1.0)	0.02 (< 10)	2.7	1.2

Note — See page 55 for legends.

Israel et al. (1998b) investigated the archival data of 13 ROSAT observations covering 1SAX J0054.9–7226. They found a flux variation with a factor of > 30 between two observations of ROSAT in 1996 and RXTE in 1998. They also determined the position with a $10''$ error circle, in which a Be star was later discovered by Stevens, Coe, & Buckley (1999). XTE J0055–724 = 1SAX J0054.9–7226 is thus a Be-XBP.

6.1.14 No. 56 — AX J0057.4–7325

Coherent pulsations with a 101.45(7) s period from No. 56 (AX J0057.4–7325) were first discovered during this study from the data of obs. R (Torii et al. 2000b; Yokogawa et al. 2000c). This source was also detected in obs. L, and weak evidence for pulsations with a period of 101.47(6) s was detected. Yokogawa et al. (2000c) investigated six ROSAT observations covering this pulsar, and found a flux variability with a factor of > 10 . All the information indicates that AX J0057.4–7325 is an XBP.

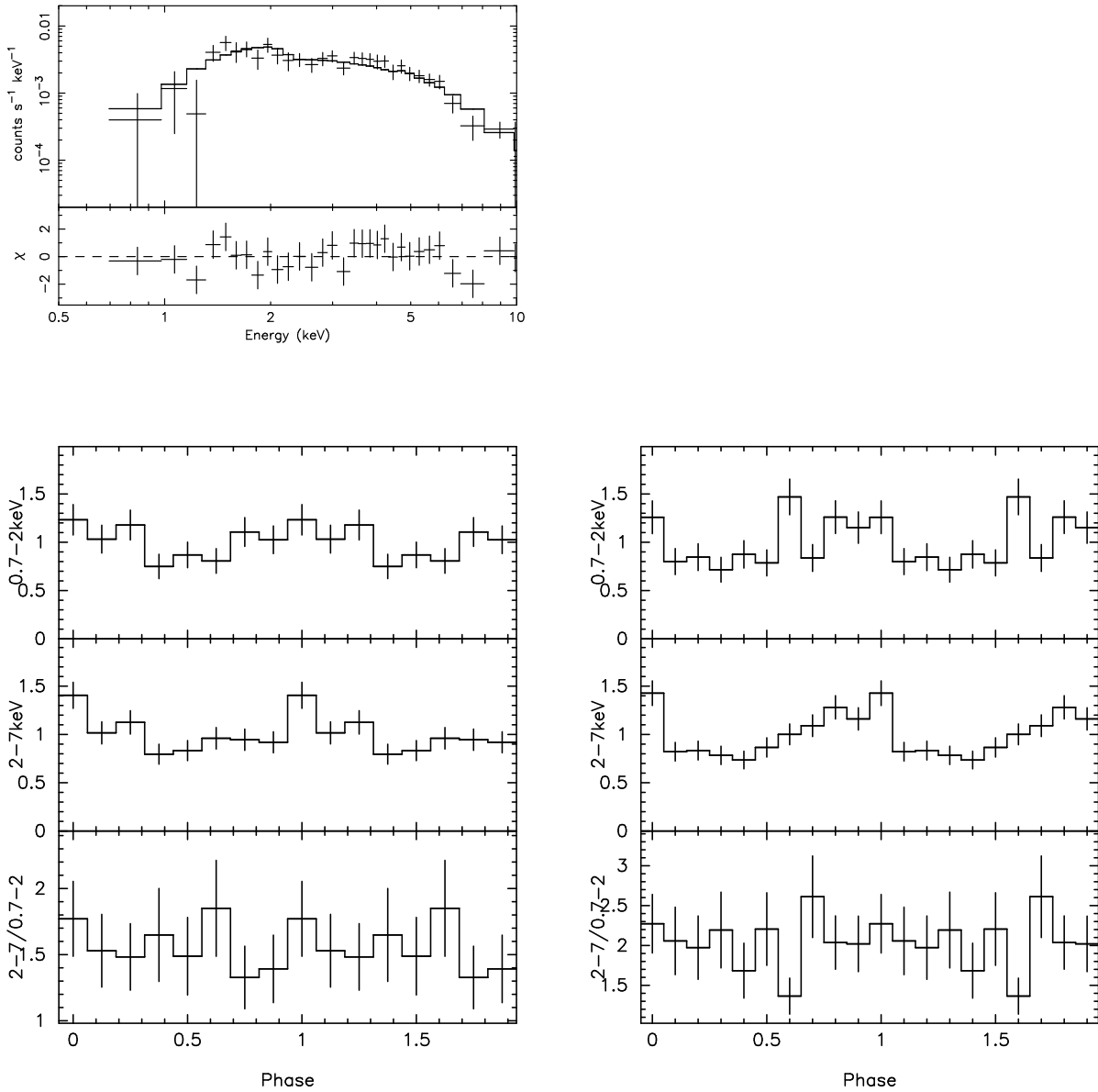


Figure 6.17: GIS spectrum (top) and pulse profiles (bottom) of AX J0057.4–7325. (Top left) The crosses are data points obtained in obs. R, while the solid line represents the best-fit model derived from the simultaneous fitting. (Bottom) Pulse profiles in obs. L (left) and obs. R (right) obtained from 0.7–2.0 keV and 2.0–7.0 keV, and their ratio.

So far optical follow-up observations have not been carried out. As far as we have investigated, only one optical source, MACS J0057–734#010, is located within the ASCA error

Table 6.14: Spectral parameters for AX J0057.4–7325 taken from table 5.5.

HR	HRerr	Obs. ID	Γ	N_{H}	F_{X}	L_{X}
0.48	0.05	L	1.1 (0.9–1.4)	8 (4–14)	1.1	0.56
		R			2.2	1.1

Note — See page 55 for legends.

circle, for which the spectral type and existence of the $\text{H}\alpha$ emission line are not known. No counterpart is found in the catalogues of emission line objects by Meyssonier & Azzopardi (1993) and Murphy & Bessell (2000). This is a rare case in which an XBP in the SMC is not associated with a Be star or an emission line object (see Haberl & Sasaki 2000). We note that AX J0057.4–7325 is located at the edge of the SMC main body, fronting the eastern wing. The fact that OB supergiant X-ray binaries (only SMC X-1 and EXO 0114.6–7361; see table 6.1 and table 7.1) are both located in the eastern wing leads us to suspect that AX J0057.4–7325 might be the third example. Therefore, deep and detailed optical observations around this pulsar are strongly encouraged.

6.1.15 No. 61 — AX J0058–7203

Coherent pulsations with a period of 280.4(4) s from No. 61 (AX J0058–7203) were first discovered during this study (Yokogawa & Koyama 1998a), and the PSD derived from the events in 1.0–6.0 keV is shown in figure 6.19 (a). In a new observation T, AX J0058–7203 was detected at a large off-axis angle of $\sim 23'$. We performed an FFT analysis on the events in the same energy band (1.0–6.0 keV) and found no significant peak as shown in figure 6.19 (b). The count rate, total counts (without background), and background level in 1.0–6.0 keV are 1.3×10^{-2} cnt s $^{-1}$, 1014 cnt, and 39% in obs. G, and 7.3×10^{-3} cnt s $^{-1}$, 642 cnt, and 42% in obs. T. The reduced total counts may cause the non detection of pulsations, although no quantitative estimation has been done.

Tsujimoto et al. (1999) investigated the archival data of 14 observations with Einstein and ROSAT covering this pulsar, and found a flux variation with a factor of $\gtrsim 10$. Haberl & Sasaki (2000) found an emission line object as a counterpart for AX J0058–7203. All the information indicates that AX J0058–7203 is an XBP, and probably has a Be star companion. The GIS spectra may show a soft excess below ~ 1 keV (figure 6.18). A blackbody model with a temperature of ~ 0.06 keV compensates for the excess, although

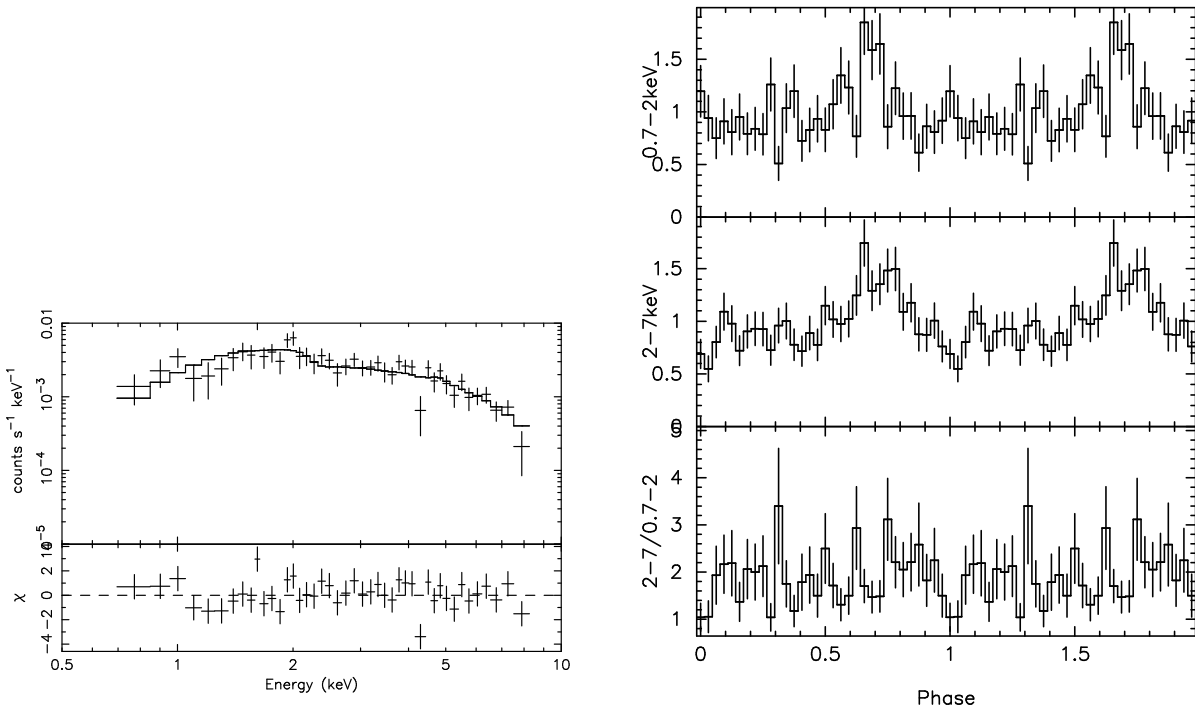


Figure 6.18: GIS spectrum (left) and pulse profiles (right) of AX J0058–7203. (Left) The crosses are data points obtained in obs. G, while the solid line represents the best-fit model derived from the simultaneous fitting. (Right) Pulse profiles in obs. G obtained from 0.7–2.0 keV and 2.0–7.0 keV, and their ratio.

Table 6.15: Spectral parameters for AX J0058–7203 taken from table 5.5.

HR	HRerr	Obs. ID	Γ	N_{H}	F_{X}	L_{X}
0.36	0.04	G	0.8 (0.6–1.0)	0.7 (< 4)	2.5	1.1
		T			4.4	1.9

Note — See page 55 for legends.

the blackbody component is not necessary from a statistical point of view.

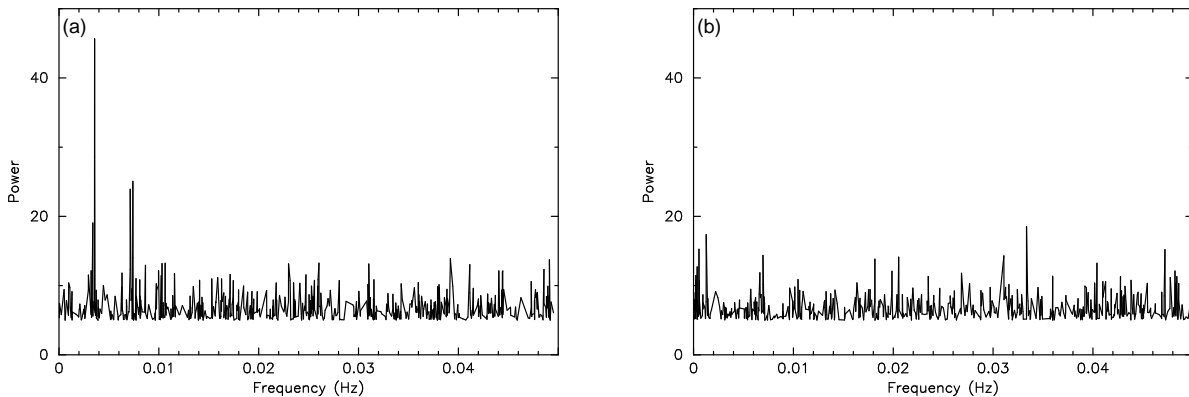


Figure 6.19: PSDs of AX J0058–7203 in (a) obs. G and (b) obs. T, obtained from the events in 1.0–6.0 keV (bin time = 10 s). Data points with a power less than 5 are not plotted. The peak detected in (a) is not found in (b).

6.1.16 No. 67 — RX J0059.2–7138

A new transient source RX J0059.2–7138 was detected with ROSAT and ASCA in simultaneous observations of SNR 0102–723 (obs. B). Coherent pulsations with a period of 2.7632(2) s were discovered from the ROSAT data (Hughes 1994), and were confirmed with the ASCA data (Kohno, Yokogawa, & Koyama 2000). The pulsed fraction is highly energy dependent as seen from figure 6.20, and is larger at higher energy (Hughes 1994; Kohno, Yokogawa, & Koyama 2000). The possible optical counterpart proposed by Hughes (1994) was later revealed to be a Be star (Southwell & Charles 1996), thus RX J0059.2–7138 is undoubtedly a Be-XBP.

The ASCA spectrum exhibits a soft excess below $\lesssim 2$ keV and a cut-off above $\gtrsim 7$ keV as described in section 5.4.4. We thus included a blackbody model as the soft component and a high energy exponential cut-off. The best-fit parameters are shown in table 6.16. Kohno, Yokogawa, & Koyama (2000) used the ROSAT and ASCA data simultaneously and carried out more elaborate analyses. They adopted various models to describe the soft excess and found that the soft component could be described by a thin-thermal plasma model or a broken power-law combined with an oxygen overabundance in the absorption column. They also found that the normalization of the soft component does not change (i.e., the

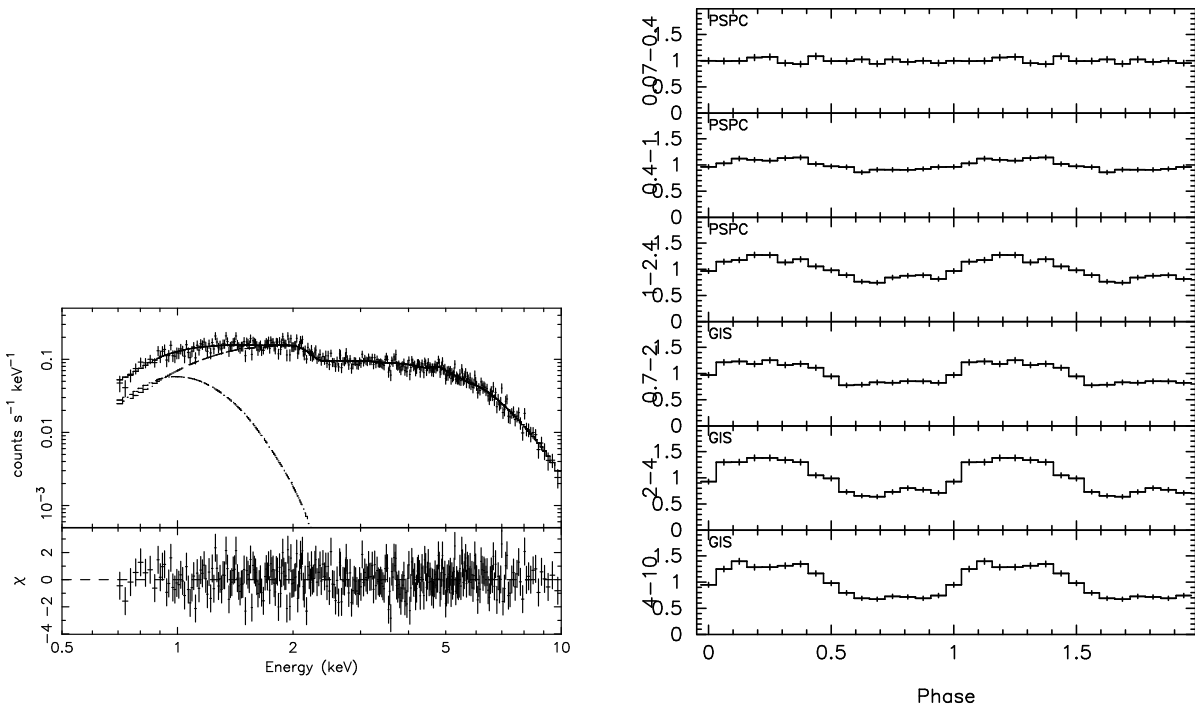


Figure 6.20: GIS spectrum (left) and pulse profiles (right) of RX J0059.2–7138. (Left) The crosses are data points obtained in obs. B, while the solid line represents the best-fit model. Spectral components are indicated by the broken lines. (Right) Pulse profiles obtained with ROSAT PSPC (upper three panels) and ASCA GIS (lower three panels) in the contemporaneous observations. Energy bands from top to bottom are 0.07–0.4 keV, 0.4–1.0 keV, 1.0–2.4 keV, 0.7–2.0 keV, 2.0–4.0 keV, and 4.0–10.0 keV.

Table 6.16: Spectral parameters for RX J0059.2–7138.

HR	HRerr	Obs. ID	Γ	E_{cut}	E_{fold}	kT	N_{H}	F_{X}	L_{X}
0.34	0.01	B	0.51	6.4	6.3	0.15	0	240	100
			(0.46–0.56)	(5.8–6.9)	(4.4–9.4)	(0.14–0.17)	(< 1.1)		

Note — See page 55 for legends. Units for E_{cut} and E_{fold} are keV.

soft component exhibits no pulsations) during the pulse phase, which is consistent with the energy dependent pulsed fraction (figure 6.20).

6.1.17 No. 74 — RX J0101.3–7211

RX J0101.3–7211 has been known to be a highly variable ROSAT source with an emission line object (Haberl & Sasaki 2000), and was classified as an XBP candidate in our earlier study (source No. 27 in Yokogawa et al. 2000e) because of its hard spectrum. Therefore, this source is strongly suspected to be a Be-XBP, although no pulsations have been detected, probably because of the limited statistics.

Sasaki et al. (2001) performed an XMM-Newton observation on SNR 0102–723 and serendipitously detected RX J0101.3–7211. Although the flux level was the lowest among previous detections with ROSAT and ASCA, coherent pulsations with a 455(2) s period were

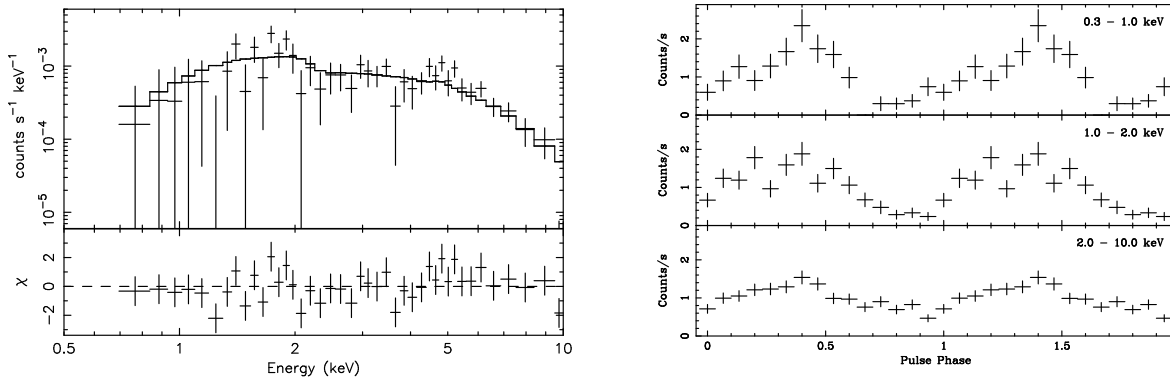


Figure 6.21: GIS spectrum (left) and XMM-Newton pulse profiles (right) of RX J0101.3–7211. (Left) The crosses are data points obtained in obs. D, while the solid line represents the best-fit model derived from the simultaneous fitting. (Right) Pulse profiles obtained with XMM-Newton in 0.3–1.0 keV, 1.0–2.0 keV, and 2.0–10.0 keV (taken from Sasaki et al. 2001).

Table 6.17: Spectral parameters for RX J0101.3–7211 taken from table 5.5.

HR	HRerr	Obs. ID	Γ	N_{H}	F_{X}	L_{X}
0.43	0.05	B	0.7 (0.5–0.9)	0.4 (< 4)	1.5	0.65
		D			1.6	0.69
		G			1.7	0.73

Note — See page 55 for legends.

discovered thanks to the high S/N ratio achieved by XMM-Newton. The pulsed fraction was found to be energy dependent and higher at lower energy, the same as AX J0049.5–7323 (section 6.1.5). Sasaki et al. (2001) also carried out a spectroscopic optical observation on the emission line object found by Haberl & Sasaki (2000), and revealed it to be a Be star. Therefore, RX J0101.3–7211 is undoubtedly a Be-XBP.

6.1.18 No. 78 — 1SAX J0103.2–7209

Hughes & Smith (1994) and Ye et al. (1995) performed ROSAT HRI observations of the shell-like radio SNR 0101–724 and detected no X-rays from the radio shell. Instead, an X-ray point source RX J0103.2–7209 (= 1SAX J0103.2–7209) having a Be star counterpart was detected inside the SNR.

Coherent pulsations with a period of 345.2(3) s from 1SAX J0103.2–7209 were first discovered in a BeppoSAX observation made on 1998 July 26–27 (Israel et al. 1998a; Israel et al. 2000). Subsequently, pulsations with a period of 348.9(3) s were detected from the ASCA source No. 78 on May 21–23, 1996 (obs. D; Yokogawa & Koyama 1998c). Israel et al. (2000) also detected 343.5(5) s pulsations from Chandra data obtained on August 23, 1999, and found a monotonic spin-up with a period derivative of -1.7 s yr^{-1} .

1SAX J0103.2–7209 has been detected in various observations with Einstein, ROSAT, ASCA, and Chandra, with nearly the same luminosity level of $\lesssim 10^{36} \text{ erg s}^{-1}$ (Israel et al. 2000, and references therein). Therefore, this pulsar can possibly be classified as a “persistent” Be-XBP, such as X Per, RX J0146.9+6121, RX J0440.9+4431, and RX J1037.5–564 (White, Swank, & Holt 1983; Mereghetti et al. 2000; Reig & Roche 1999). The 755-s pulsar AX J0049.5–7323 may also belong to this class, although the upper limit of the flux variation is not known.

Table 6.18: Spectral parameters for 1SAX J0103.2–7209 taken from table 5.5.

HR	HRerr	Obs. ID	Γ	N_{H}	F_{X}	L_{X}
0.36	0.06	B	0.8 (0.6–1.0)	0 (< 4)	1.3	0.56
		D			1.1	0.48
		G			0.79	0.34

Note — See page 55 for legends.

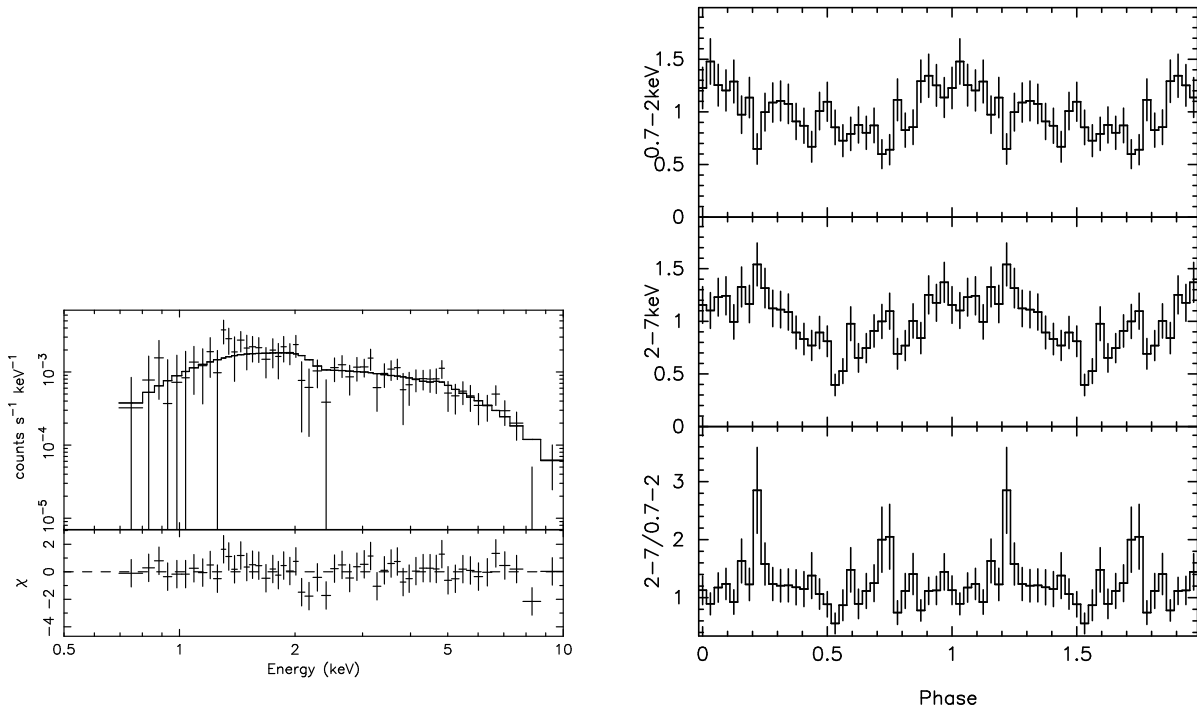


Figure 6.22: GIS spectrum (left) and pulse profiles (right) of 1SAX J0103.2–7209. (Left) The crosses are data points obtained in obs. D, while the solid line represents the best-fit model derived from the simultaneous fitting. (Right) Pulse profiles in obs. D obtained from 0.7–2.0 keV and 2.0–7.0 keV, and their ratio.

6.1.19 No. 83 — AX J0105–722

Since No. 83 (AX J0105–722) and No. 84 are located only $\sim 3'$ from each other, mutual contamination is not negligible. We therefore used an oval-shaped region including both AX J0105–722 and No. 84 (region 1 in figure 6.23 (a)) in the timing analysis, and detected coherent pulsations with a $3.34300(3)$ s period at a marginal significance of $\sim 99.5\%$ (Yokogawa & Koyama 1998b; figure 5.5 (c)). We then separately searched for pulsations from regions 2 and 3 in figure 6.23 (b) and found weak evidence for the 3.34-s pulsations only from region 2 (which includes AX J0105–722). Therefore, we conclude that the pulsations are attributable to AX J0105–722. The spectrum of AX J0105–722 is rather soft (see table 6.19) compared to those of typical XBPs ($\Gamma \sim 1$; Nagase 1989).

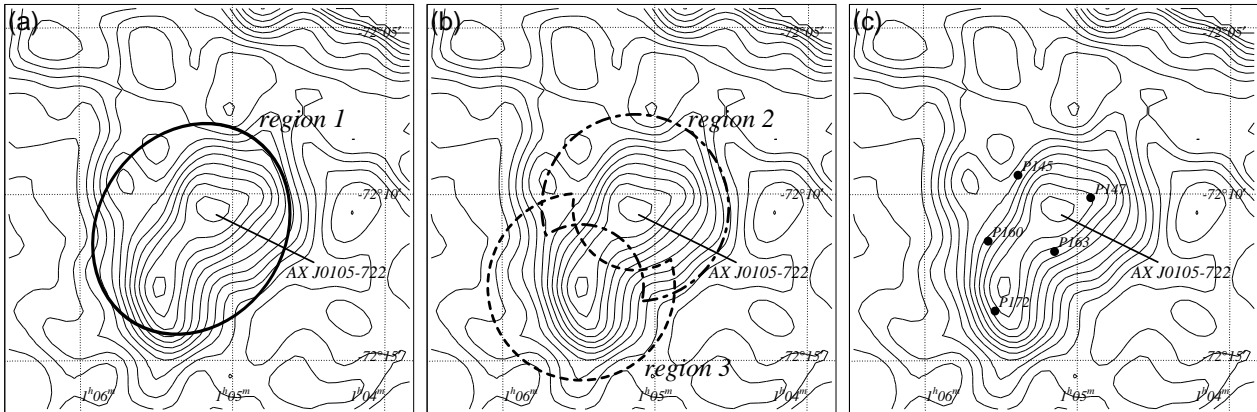


Figure 6.23: ASCA GIS contour images around AX J0105–722 in 0.7–7.0 keV, overlaid with the equatorial coordinates (J2000). Two ASCA sources are detected in this image, one of which is AX J0105–722 and the other is No. 84, located to the south. Regions 1–3 from which event lists were extracted for pulsation searches (see text) are indicated by the ellipse and circles in (a) and (b). The five dots marked with “Pn” in (c) are the ROSAT sources in Haberl et al. (2000) with an ID number of n .

Filipović et al. (2000) used the data from high resolution X-ray and radio observations around this source made with ROSAT, ATCA (Australia Telescope Compact Array), and MOST (Molonglo Observatory Synthesis Telescope). They resolved the ASCA sources AX J0105–722 and No. 84 into five sources as shown in figure 6.23 (c): AX J0105–722 is surrounded by three ROSAT PSPC sources, Nos. 145, 147, and 163 (here, PSPC-145, PSPC-147, and PSPC-163) in Haberl et al. (2000). PSPC-163 (RX J0105.1–7211) exhibits a hard spectrum typical of HMXBs and is identified with an emission line object catalogued in Meyssonier & Azzopardi (1993), and thus is a likely candidate for a Be/X-ray binary (e.g., Haberl & Sasaki 2000). PSPC-145 is positionally coincident with the ratio emission from SNR DEM S128, has a soft spectrum typical of SNRs, and exhibits no flux variation, thus is likely to be an X-ray emitting SNR. PSPC-147 has the hardest spectrum among the three, although the source nature of the source is unclear. Considering these facts, we propose that the 3.34-s pulsations can be attributed to RX J0105.1–7211, which is a Be-XBP, and that the mutual contamination of X-rays from RX J0105.1–7211, PSPC-145, and PSPC-147 in the ASCA data caused the rather soft spectrum of AX J0105–722. Because of this situation and the rather marginal detection of pulsations, follow-up X-ray observations with high spatial resolution and good S/N ratio are needed.

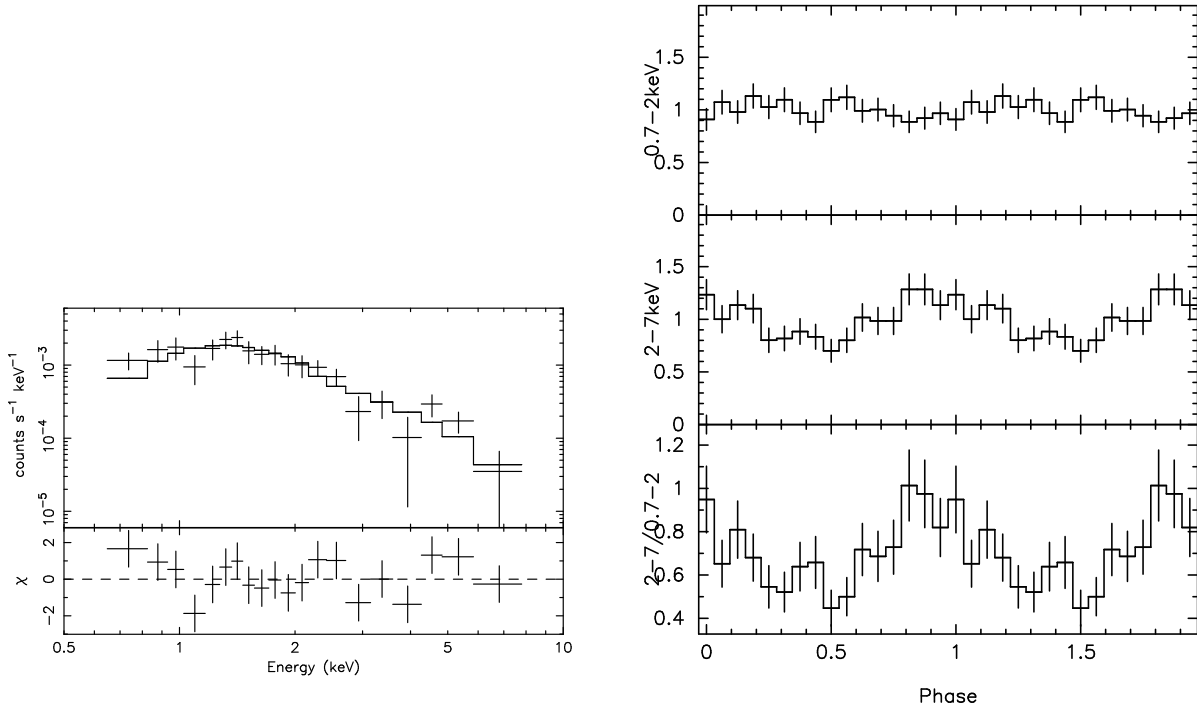


Figure 6.24: GIS spectrum (left) and pulse profiles (right) of AX J0105–722. (Left) The crosses are data points obtained in obs. D, while the solid line represents the best-fit model. (Right) Pulse profiles in obs. D obtained from 0.7–2.0 keV and 2.0–7.0 keV, and their ratio.

Table 6.19: Spectral parameters for AX J0105–722 taken from table 5.5.

HR	HRerr	Obs. ID	Γ	N_{H}	F_{X}	L_{X}
–0.20	0.08	D	2.2 (1.9–2.6)	0 (< 2)	0.30	0.13

Note — See page 55 for legends.

6.1.20 No. 90 — XTE J0111.2–7317

A new transient source, XTE J0111.2–7317, was serendipitously found with RXTE and CGRO, and at the same time coherent pulsations with a period of ~ 31 s were discovered (Chakrabarty et al. 1998a; Wilson & Finger 1998). In the TOO observation with ASCA (obs. I), pulsations with a 30.9497(4) s period were unambiguously detected from No. 90. Thus No. 90 is undoubtedly the counterpart for XTE J0111.2–7317, and the position was

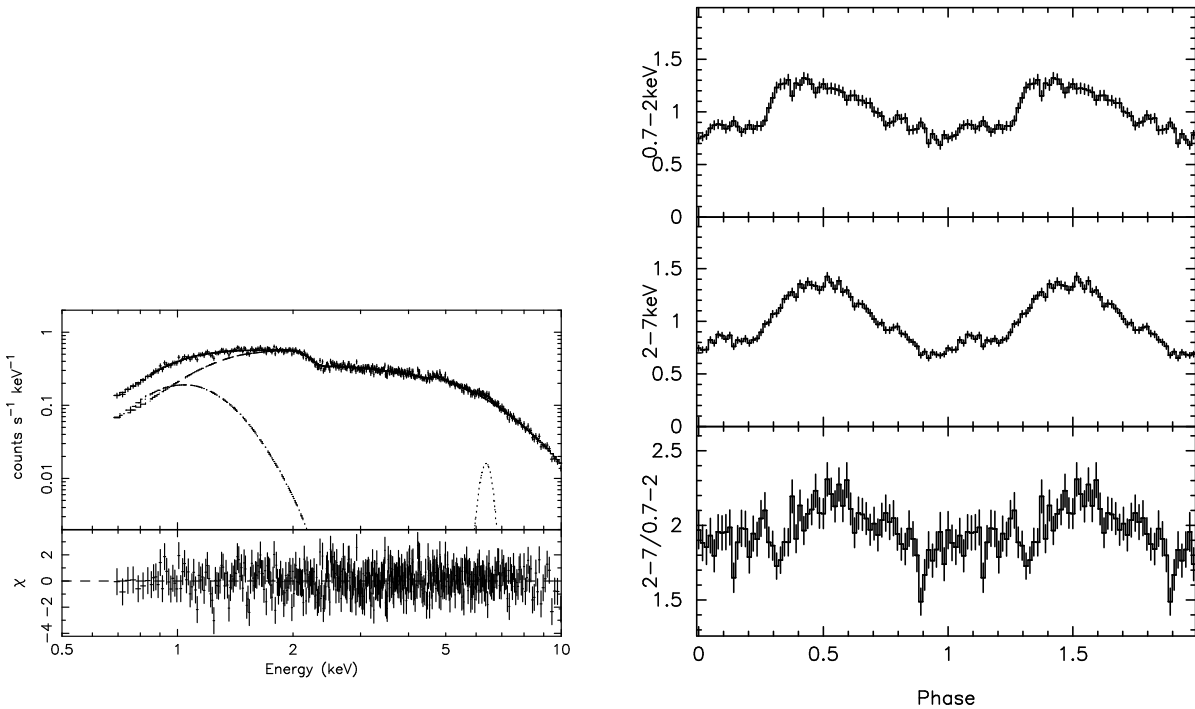


Figure 6.25: GIS spectrum (left) and pulse profiles (right) of XTE J0111.2–7317. (Left) The crosses are data points obtained in obs. I, while the solid line represents the best-fit model. Spectral components are indicated by the broken lines. (Right) Pulse profiles in obs. I obtained from 0.7–2.0 keV and 2.0–7.0 keV, and their ratio.

Table 6.20: Spectral parameters for XTE J0111.2–7317 taken from table 5.5.

HR	HRerr	Obs. ID	Γ	kT	N_{H}	F_{X}	L_{X}
0.33	0.003	I	0.79 (0.76–0.82)	0.144 (0.137–0.150)	2.3 (1.6–3.0)	370	170

Note — See page 55 for legends.

determined with better accuracy than RXTE (Chakrabarty et al. 1998b). Israel et al. (1999) detected two stars in the error circle; the fainter one was revealed to be a Be star and was proposed to be the optical counterpart for this pulsar. Coe, Haigh, & Reig (2000) carried out a more elaborate optical spectroscopy on the optical counterpart, and confirmed the Be nature of this star. Therefore, XTE J0111.2–7317 is undoubtedly a Be-XBP.

The ASCA spectrum of this pulsar shows a soft X-ray excess above a power-law model and bump-like residuals around 6–7 keV. Adding a blackbody component and a narrow Gaussian gave a nice fit to the spectrum, and the best-fit parameters in table 5.5 and table 6.20 are derived from this model. However, the pulse phase resolved spectroscopy performed by Yokogawa et al. (2000d) revealed that the soft blackbody component should be pulsating in this model, while the emission region of the blackbody is extremely large (~ 800 km in radius) and so pulsation is impossible. Therefore, Yokogawa et al. (2000d) proposed an alternative model, the “inversely broken power-law,” which is a power-law with a larger/smaller photon index below/above a break energy, to describe the whole continuum and the pulsations in the low energy band. The pulsations of the soft component are in striking contrast to the non-pulsating soft component of RX J0059.2–7138, although the overall continuum shapes in the ASCA band resemble each other (see table 6.16 and table 6.20).

6.1.21 No. 94 — SMC X-1

SMC X-1 (No. 94) is a well-established XBP with a pulse period of ~ 0.71 s, having a B-type supergiant companion (e.g., Bildsten et al. 1997). SMC X-1 has been detected in three ASCA observations. The 0.71-s pulsations were detected only from the data of obs. A and obs. I (see table 6.1). In obs. C, it was in a low-state and went into eclipse as predicted by the ephemeris of Wojdowski et al. (1998). Since the low-state of SMC X-1 should be caused by an occultation of the X-ray emitter, probably by the tilted accretion disk (Wojdowski et al. 1998; Vrtilik et al. 2001), the intrinsic luminosity in the low-state should be as high as that in the high-state. Therefore, the small F_X and L_X derived from the obs. C data (table 6.21) appear to be an underestimate of the true intensity.

The soft excess above a power-law was detected and was described by a blackbody component with parameters given in table 6.21. Paul et al. (2001) elaborately carried out a phase resolved spectroscopy with the ASCA data (GIS and SIS) of obs. A and found pulsations of the soft component. Therefore, for the same reason as described in section 6.1.20, attributing the soft excess to blackbody emission is not appropriate. Paul et al. (2001) found that the inversely broken power-law model or two-component power-law model could describe both the continuum shape and the pulsating nature of the soft excess.

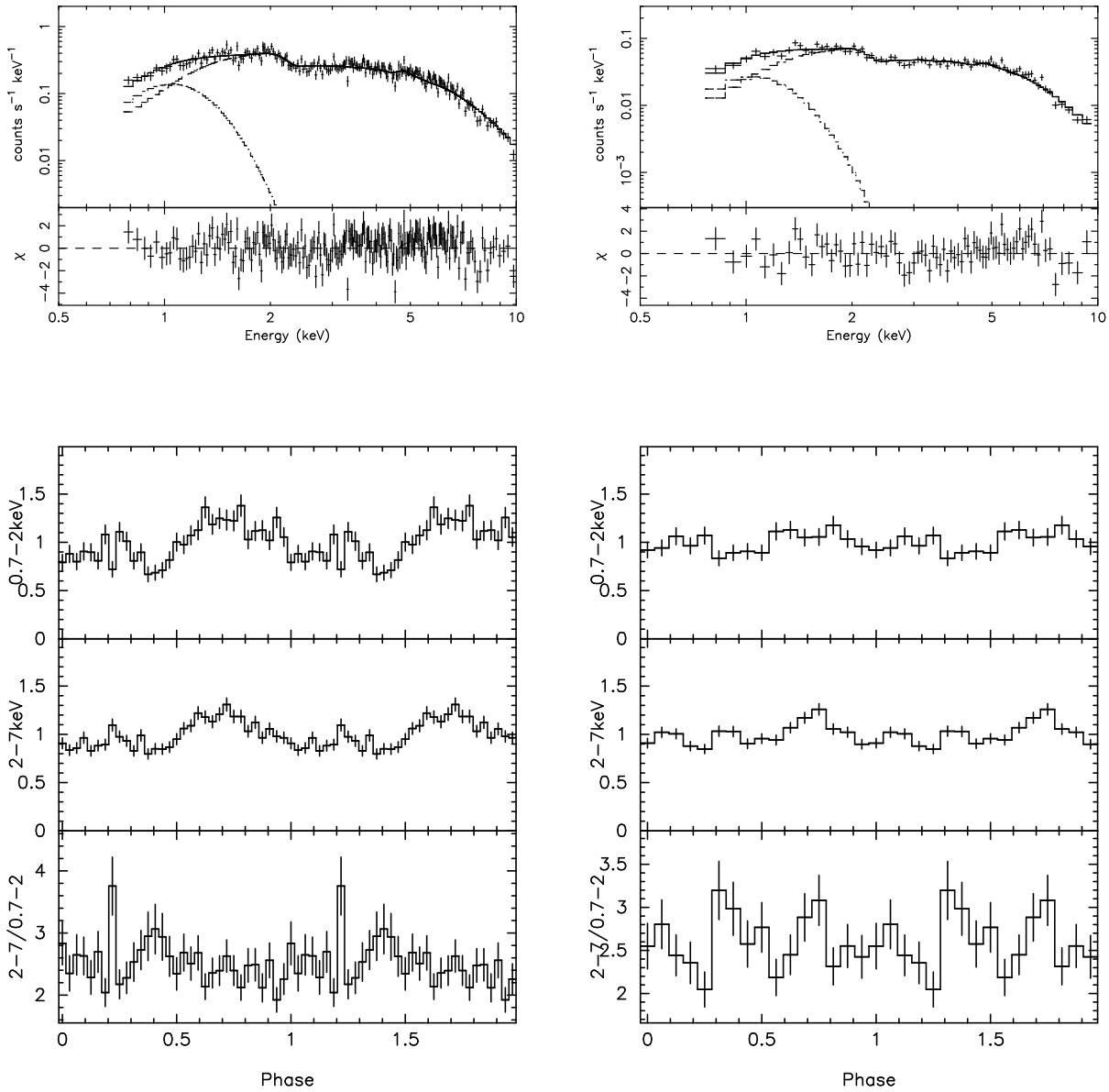


Figure 6.26: GIS spectra (top) and pulse profiles (bottom) of SMC X-1. (Top) The crosses are data points obtained in obs. A (left) and obs. I (right), while the solid lines represent the best-fit models. Spectral components are indicated by the broken lines. (Bottom) Pulse profiles in obs. A (left) and obs. I (right) obtained from 0.7–2.0 keV and 2.0–7.0 keV, and their ratio.

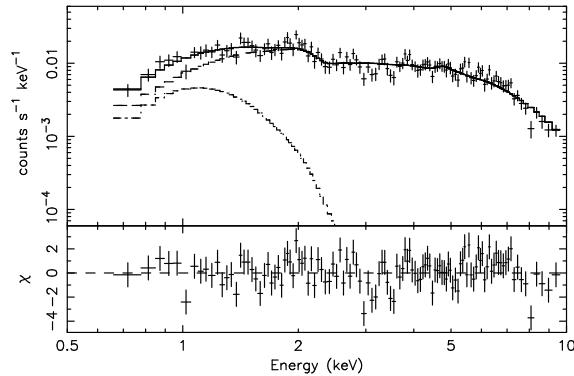


Figure 6.27: GIS spectrum of SMC X-1 in obs. C. The crosses are data points, while the solid line represents the best-fit model. Spectral components are indicated by the broken lines.

Table 6.21: Spectral parameters for SMC X-1 taken from table 5.5.

HR	HRerr	Obs. ID	Γ	kT	N_{H}	F_{X}	L_{X}
0.43	0.01	A	0.69 (0.61–0.76)	0.13 (0.11–0.15)	4 (2–6)	220	110
0.40	0.02	C	0.45 (0.35–0.53)	0.20 (0.13–0.29)	0 (< 2)	8.9*	3.8*
0.44	0.01	I	0.35 (0.27–0.44)	0.16 (0.13–0.19)	2 (< 4)	150	67

Note — See page 55 for legends.

*: Intrinsic intensity is much higher (see text).

6.1.22 Other pulsars not detected with ASCA — 2E 0050.1–7247, XTE J0052–723, RX J0117.6–7330, and XTE J0050–732#1 and #2

2E 0050.1–7247 Coherent pulsations with a 8.8816(2) s period from 2E 0050.1–7247 = RX J0051.8–7231 were discovered in a ROSAT observation by Israel et al. (1997). Flux variability of a factor 20 between two ROSAT observations and a Be star in the error circle were found, hence this pulsar is a Be-XBP. ASCA covered the position of 2E 0050.1–7247 in obs. H. We did not detect any positive excess above the background level from this position. The upper limit of its flux is estimated to be $\sim 1 \times 10^{-13} \text{erg s}^{-1} \text{cm}^{-2}$ (0.7–10.0 keV), assuming a photon index of ~ 1 .

XTE J0052–723 A new transient pulsar XTE J0052–723 with a period of 4.782(1) s was discovered in RXTE observations on December 27, 2000, and January 5, 2001 (Corbet, Marshall, & Markwardt 2001). The transient nature and the pulse period imply that this source is probably a Be-XBP. The position was determined with a $2' \times 1'$ error box and is covered by ASCA observation H. We detected no X-rays from this position and set the upper limit to be $\sim 1 \times 10^{-13} \text{erg s}^{-1} \text{cm}^{-2}$ (0.7–10.0 keV), assuming a photon index of ~ 1 .

RX J0117.6–7330 RX J0117.6–7330 was serendipitously discovered in a ROSAT PSPC observation (Clark, Remillard, & Woo 1996). The luminosity was $2.3 \times 10^{37} \text{erg s}^{-1}$ between 0.2–2.5 keV at that time (Clark, Remillard, & Woo 1997), and was found to diminish by a factor of over 100 within one year. Macomb et al. (1999) discovered coherent pulsations with a ~ 22.07 s period from the same data, with the aid of the archival data obtained by BASTE onboard CGRO in the same epoch. Strong Balmer emission lines and infrared excess were detected from the companion star in the error circle (Coe et al. 1998), indicating that RX J0117.6–7330 is a Be-XBP. Although the position of RX J0117.6–7330 was covered in ASCA observations A and C, no X-ray emissions were detected. It was difficult to estimate the upper limits of the flux because of the contamination from SMC X-1, which is located only $\sim 5'$ away from RX J0117.6–7330.

XTE J0050–732#1 and #2 Lamb et al. (2001) submitted a paper reporting on discovery of two pulsars with periods of 16.6 s and 25.5 s from archival data of RXTE. Although they gave no names for these pulsars, we tentatively designate them as XTE J0050–732#1 (16.6 s) and XTE J0050–732#2 (25.5 s) because the RXTE observation was centered on ($00^{\text{h}}50^{\text{m}}44^{\text{s}}.64$, $-73^{\circ}16'04''.8$). Their long pulse periods are typical of XBPs, although more information (optical counterparts and flux variability) is required for further confirmation. We argue that their identification of XTE J0050–732#1 with a ROSAT source, RX J0051.8–7310, is incorrect. They detected RX J0051.8–7310 in the ASCA archival data of obs. Q and found very weak evidence (significance = 82%) for 16.6 s pulsations by performing an FFT only in a range of 0.02–0.2 Hz. However, the ASCA source at the position of RX J0051.8–7310 is AX J0051.6–7311, which is a 172-s pulsar (see section 6.1.8) and is identified with RX J0051.9–7311. Non-detection of the 172 s pulsations by Lamb et al. (2001) is simply due to the limited frequency range used for the FFT analysis. Note that RX J0051.8–7310 and RX J0051.9–7311 are identical. The former name was used for No. 82 in Kahabka et al. (1999) while the latter was used for No. 41 in Sasaki, Haberl, & Pietsch

(2000). Therefore, in private we proposed that Lamb et al. should perform an FFT in a whole frequency range.

6.2 Period Distribution of XBPs

We have shown that at least 22 out of the 25 X-ray pulsars in the SMC are XBPs² probably with a high mass star companion. Recently Liu, van Paradijs, & van den Heuvel (2000) compiled a catalogue of Galactic HMXBs in which 49 XBPs are included³. In addition, we investigated the recent literature and found four new XBPs, AX J1740.1–2847, XTE J1543–568, SAX J2239.3+6116, and AX 1841.0–0536 (Sakano et al. 2000; Finger & Wilson 2000; In ’t Zand et al. 2001; Bamba et al. 2001). In figure 6.28 we show the distribution of pulse periods of the 53 XBPs in the Galaxy and 22 in the SMC; the actual numbers are given in (a), while the number of SMC pulsars is normalized (multiplied by 53/20) in (b). A weak hint that the Galactic XBPs tend to have longer pulse periods can be found, although the statistics are limited. However, the difference in the period distribution may be attributable to an observational selection effect for the following reason.

Mass accretion onto a neutron star is characterized by three radii: (1) the accretion radius r_a , within which material is captured by the gravitation and accretes onto the neutron star, (2) the magnetospheric radius r_m , where the magnetic field pressure and the ram pressure of the accreting material equate with each other, and (3) the corotation radius r_c , where the neutron star corotation velocity is equal to the Keplerian velocity. Thus the definitions are:

$$r_a = 4GM/v_0^2, \quad (6.2)$$

$$B(r_m)^2/8\pi = \rho(r_m)v(r_m)^2, \text{ and} \quad (6.3)$$

$$r_c = (GMP^2/4\pi^2)^{1/3}, \quad (6.4)$$

where M , $B(r)$, and P are the mass, magnetic field strength at r , and spin period of the neutron star, while $\rho(r)$, v_0 , and $v(r)$ are the density at r , terminal velocity, and inflowing velocity at r of the stellar wind. If $r_c < r_m < r_a$, the stellar wind material within r_a accretes onto the magnetosphere and is blown away by the centrifugal force, because the drag exerted

²AX J0043–737, AX J0049–732, and AX J0105–722 were excluded, as further confirmation is needed.

³In this paper we do not regard 4U 2206+543 as an XBP because of the non detection of pulsations in a further study by Corbet & Peele (2001)

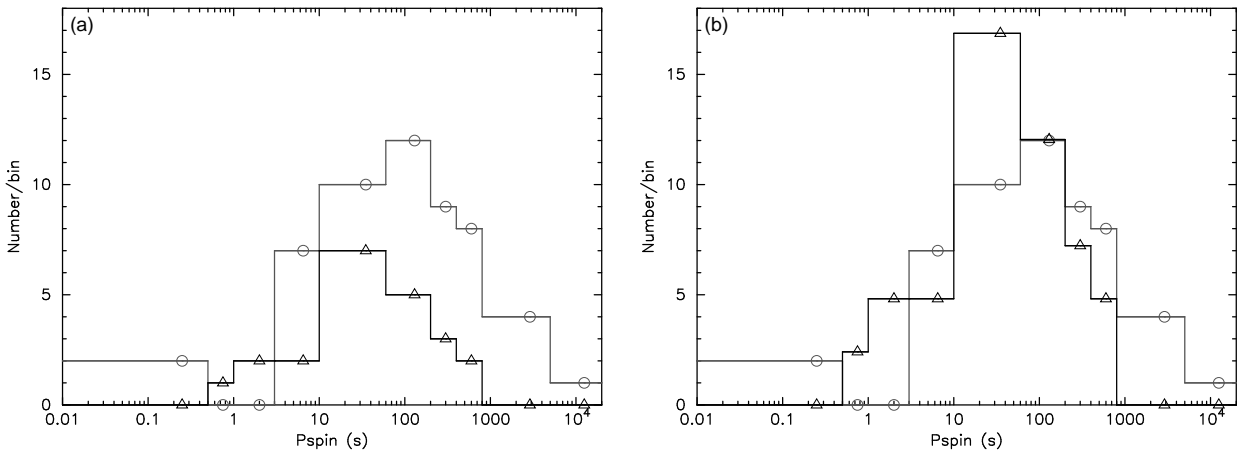


Figure 6.28: Period distribution of XBPs in the SMC (solid lines; triangles) and our Galaxy (dotted lines; circles). Horizontal and vertical axes respectively indicate the pulse period and the number of XBPs in each period bin. The number of SMC pulsars are normalized by multiplying the factor 53/22 in (b), while the actual (unnormalized) number is shown in (a).

by the magnetosphere is super-Keplerian (the so-called “propeller” effect). Therefore, by imposing $r_c = r_m$, the minimum luminosity L_{\min} at which accretion is permitted is

$$L_{\min} \approx 2 \times 10^{37} \left(\frac{R}{10^6 \text{ cm}} \right)^{-1} \left(\frac{M}{1.4M_{\odot}} \right)^{-2/3} \left(\frac{\mu}{10^{30} \text{ G cm}^3} \right)^2 \left(\frac{P}{1 \text{ s}} \right)^{-7/3} \text{ erg s}^{-1}, \quad (6.5)$$

where $\mu = BR^3/2 = 0.5 \times 10^{30} (B/10^{12} \text{ G})(R/10^6 \text{ cm})^3 \text{ G cm}^3$ is the magnetic dipole moment and R is the radius of the neutron star. From this equation, it is expected that XBPs with longer periods are fainter than those with shorter periods. Therefore, the lack of long period XBPs in the SMC (figure 6.28) may be due to the fact that such pulsars are too faint at the SMC distance, and so pulsations have not been detected.

We used our ASCA data and various data in the literature to investigate the relation between the pulse periods and minimum luminosities (L_{\min}) of the SMC XBPs, which were collected from observations in which the pulsations were detected. The luminosities were calculated for the 2–10 keV band in order to avoid the uncertainty from the absorption column density and the soft excess in the spectra. For the sources of which L_{\min} is detected with ASCA, we used the spectral parameters determined in this study (table 5.5) to calculate the luminosity. For SMC X-1, L_{\min} was obtained with ROSAT in its low-state (Kahabka & Li 1999). As mentioned in section 6.1.21, the intrinsic luminosity in the low-state should be

as high as that in the high-state; thus, we used $L_{\min} = 10^{38}$ erg s $^{-1}$ for SMC X-1, which is a typical value for the high-state. XTE J0052–723 has been detected with only RXTE, but the spectral parameters have not been reported. We thus assumed the photon index Γ to be 0.8, which is the mean value for XBPs derived from this study, and converted the source intensity (8 mCrab; Corbet, Marshall, & Markwardt 2001) to the luminosity. The minimum luminosities from XTE J0055–724 and RX J0101.3–7211 were detected with BeppoSAX and XMM-Newton, respectively. Since these satellites cover the 2–10 keV band, we used the spectral parameters determined with these satellites (Santangelo et al. 1998; Sasaki et al. 2001) to derive the 2–10 keV luminosities. For XTE J0050–732#1 and #2, only pulsed flux is reported (Lamb et al. 2001) because of contamination from other sources in the FOV of the RXTE observation. We followed the spectral model they assumed ($\Gamma = 1.0$ and $N_{\text{H}} = 1 \times 10^{21}$ cm $^{-2}$) and determined the pulsed luminosity. The minimum luminosities from 2E 0050.1–7247 and RX J0052.1–7319 were detected with ROSAT. In order to estimate the flux, Israel et al. (1997) determined that Γ was 1.1 from the ROSAT PSPC spectrum of 2E 0050.1–7247, while Kahabka (2000) assumed $\Gamma = 1$ for RX J0052.1–7319. Although the ROSAT bandpass is below ~ 2 keV, we extrapolated those power-law models to determine the 2–10 keV luminosities. ROSAT also detected the minimum luminosity from RX J0117.6–7330 and found a very soft spectrum ($\Gamma \sim 2.7$) in the ROSAT bandpass (Clark, Remillard, & Woo 1997). Such a soft spectrum is also found from RX J0059.2–7138 ($\Gamma \sim 2.1$ for the ROSAT spectrum; determined from the archival data in this study), which has a rather hard spectrum above ~ 2 keV (section 6.1.16; Kohno, Yokogawa, & Koyama 2000). Therefore, we assumed that RX J0117.6–7330 also has a hard spectrum above ~ 2 keV, and that the flux ratio below and above ~ 2 keV is the same as that of RX J0059.2–7138. We then converted the ROSAT flux to the 2–10 keV luminosity.

Table 6.22 and figure 6.29 give the minimum luminosities and pulse periods. The three lines in figure 6.29 indicate the centrifugal limit (equation 6.5) with $\mu = 10^{28}$, 10^{30} , and 10^{32} G cm 3 . Since no XBP can exist below the line corresponding to its magnetic moment, this plot provides an upper limit of the magnetic moment for each XBP. A loose anti-correlation between L_{\min} and pulse periods is found in figure 6.29, which would roughly be explained by the centrifugal barrier mechanism (equation 6.5). The fact that the observed L_{\min} is less sensitive to pulse periods than predicted by equation 6.5 may indicate a severe selection effect for XBPs on the fainter side. It is notable that the faintest four pulsars (RX J0101.3–7211, 1SAX J0103.2–7209, AX J0051.6–7311, and AX J0049.5–7323) have rather long periods, and their pulsations were detected in a high S/N observation with XMM-Newton or in very

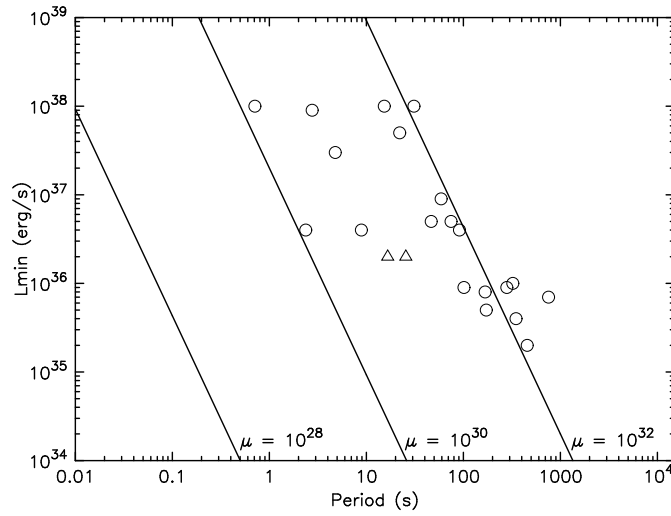


Figure 6.29: Plot of minimum luminosities as a function of pulse periods of X-ray binary pulsars in the SMC. Triangles and circles represent pulsed luminosity and total luminosity, respectively. The three lines indicate equation 6.5 with $\mu = 10^{28}$, 10^{30} , and 10^{32} G cm³, below which accretion is inhibited by centrifugal force at the magnetosphere.

long observations (D and Q) with ASCA. Therefore, high sensitivity observations in the future will probably discover long pulsations from fainter objects, which will compensate for the current lack of long pulsars in the SMC.

Table 6.22: Minimum luminosities and other relevant information of XBPs in the SMC. XBPs are arranged in order of L_{\min} .

No.	Name	Period (s)	L_{\min}^* (erg s ⁻¹)	References
94	SMC X-1	0.709103	1×10^{38}	1 (ROSAT)
43	RX J0052.1–7319	15.3	1×10^{38}	2 (ROSAT)
90	XTE J0111.2–7317	30.9497	1×10^{38}	3 (obs. I)
67	RX J0059.2–7138	2.763221	9×10^{37}	4 (obs. B)
...	RX J0117.6–7330	22.0669	5×10^{37}	5 (ROSAT)
...	XTE J0052–723	4.782	3×10^{37}	6 (RXTE)
51	XTE J0055–724	58.963	9×10^{36}	7 (SAX)
47	1WGA J0053.8–7226	46.63	5×10^{36}	This work (obs. H)
24	AX J0049–729	74.68	5×10^{36}	8 (obs. F)
49	SMC X-2	2.37230	4×10^{36}	9 (obs. R)
...	2E 0050.1–7247	8.8816	4×10^{36}	10 (ROSAT)
37	AX J0051–722	91.12	4×10^{36}	This work (obs. H)
...	XTE J0050–732#1	16.6	$2 \times 10^{36\dagger}$	11 (RXTE)
...	XTE J0050–732#2	25.5	$2 \times 10^{36\dagger}$	11 (RXTE)
32	AX J0051–733	323.2	1×10^{36}	12 (obs. F)
56	AX J0057.4–7325	101.45	9×10^{35}	13 (obs. R)
61	AX J0058–7203	280.4	9×10^{35}	14 (obs. G)
44	XTE J0054–720	167.8	8×10^{35}	15 (obs. T)
30	AX J0049.5–7323	755.5	7×10^{35}	16 (obs. Q)
40	AX J0051.6–7311	172.40	5×10^{35}	17 (obs. Q)
78	1SAX J0103.2–7209	348.9	4×10^{35}	This work (obs. D)
74	RX J0101.3–7211	455	2×10^{35}	18 (XMM)

*: In 2–10 keV.

†: Pulsed luminosity.

References — (1) Kahabka & Li 1999; (2) Kahabka 2000; (3) Yokogawa et al. 2000d; (4) Kohno, Yokogawa, & Koyama 2000; (5) Macomb et al. 1999 (6) Corbet, Marshall, & Markwardt 2001; (7) Santangelo et al. 1998; (8) Yokogawa et al. 1999; (9) Yokogawa et al. 2001b; (10) Israel et al. 1997; (11) Lamb et al. 2001; (12) Imanishi et al. 1999; (13) Yokogawa et al. 2000c; (14) Tsujimoto et al. 1999; (15) Yokogawa et al. 2001a; (16) Yokogawa et al. 2000a; (17) Yokogawa et al. 2000b; (18) Sasaki et al. 2001;

6.3 SNRS – I: from SIS

6.3.1 No. 21 — 0045–734 (N19)

Yokogawa et al. (2001c) carried out a detailed study of three SNRs, No. 21 (0045–734), No. 66 (0057–7226), and No. 82 (0103–726), with ROSAT HRI images and ASCA SIS spectra. We give a brief summary of each SNR separately in corresponding subsections.

We simultaneously used the SIS spectra of 0045–734 obtained in obs. F and obs. Q (figure 6.30). We fitted the spectra with an optically thin thermal plasma model in a non-equilibrium ionization (NEI) state, coded by Masai (1994). The physical parameters in the NEI model are the electron temperature kT , metal abundances, and the ionization timescale $\tau = n_e t$, where n_e is the electron density and t is the elapsed time after the plasma was heated up.

We first fitted the spectra with all the metal abundances fixed to the SMC mean value (0.2 solar). This model, however, left bump-like residuals at ~ 1 keV and ~ 1.3 keV, indicating the existence of emission lines from Ne-K/Fe-L and Mg-K. Therefore, we allowed the Mg abundance to be free. Since the Ne-K and Fe-L lines may equally contribute to the X-rays around ~ 1 keV, we treated the abundances of Ne and Fe in the following three cases: (I) Ne is free, (II) Fe is free, and (III) both Ne and Fe are free. In model III, the derived best-fit temperature is unusually large, $kT \sim 25$ keV, thus we did not adopt it. Models I and II, on the other hand, give equally better fits with no bump-like residuals as shown in figure 6.30. The best-fit parameters are given in table 6.23. In both models the abundances of Mg and Ne/Fe are larger than those of the SMC mean value.

The ROSAT HRI image is shown in figure 6.30, overlaid with the radio contours at 843 MHz. The radio emission exhibits a partial shell in the northwest (NW) and weak diffuse structure in the southeast (SE). No X-ray emissions are found at the radio shell; instead, X-rays are concentrated within the radio shell and diffuse structure.

From the X-ray image, we estimated the volume V of the X-ray emitting plasma. We simply assumed that the plasma in 0045–734 fills a cylinder with a height of $3'$ and a diameter of $1'$, thus we obtained $V = 3.6 \times 10^{59} \cdot \beta \text{ cm}^3$, where β represents the uncertainty of the volume. From the emission measure EM determined by the spectral fitting, we can estimate the electron density of the plasma n_e by $n_e = \sqrt{EM/V}$. Here and in the following, the number density of nucleons is simply assumed to be the same as that of electrons. The

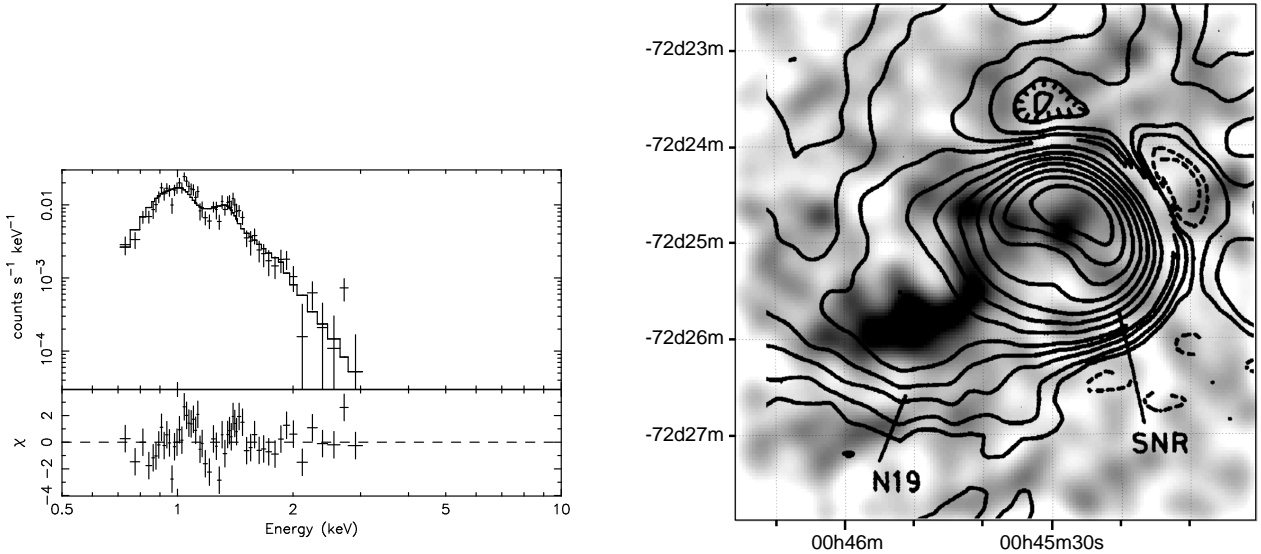


Figure 6.30: (Left) SIS spectrum of 0045–734 obtained in obs. Q (crosses) with the best-fit model in case I (solid line). (Right) Gray-scale image around 0045–734 obtained with ROSAT HRI, overlaid with contours of the MOST radio image at 843 MHz (Mills et al. 1982). The equatorial coordinates are in equinox 1950.0.

age t was then determined from the ionization timescale τ by $t = \tau/n_e$. The total mass of the plasma M_{total} is estimated by $M_{\text{total}} = n_e V m_H$, where m_H is the mass of a hydrogen atom. We then determined the mass of the overabundant heavy elements using M_{total} and the best-fit abundances. These estimated parameters are given in table 6.24. The lower limit for the ionization age of 0045–734 is 2.9×10^4 yr in both the models, which is consistent with the age of 5.7×10^4 yr derived from an optical study of the kinematics (Rosado, Le Coarer, & Georgelin 1994).

Since the best-fit abundances are much higher than the SMC mean value (table 6.23), the ejecta should contribute largely to the element masses derived above. Therefore, in figure 6.31, we compare the element masses with the theoretical predictions of chemical compositions produced with supernovae (SNe) with various progenitor masses (Tsujiimoto et al. 1995). A type Ia origin is rejected because the data do not show a large excess of Fe as expected from the theory. On the other hand, the data roughly agree with a type II SN origin with a progenitor mass of $\lesssim 20M_{\odot}$.

Table 6.23: Spectral parameters for 0045–734, 0057–7226, and 0103–726.

SNR	— 0045–734 —		0057–7226	— 0103–726 —	
Model*	I	II	...	I	III
$\log \tau$ (s cm ⁻³)	13.00 [‡] _{-1.20} ^{+∞}	11.74 ^{+∞} _{-0.41}	11.01 ^{+∞} _{-0.44}	10.97 ^{+0.21} _{-0.21}	10.82 ^{+0.25} _{-0.26}
kT_e (keV)	0.37 ^{+0.10} _{-0.05}	0.96 ^{+0.08} _{-0.05}	0.9 ^{+0.8} _{-0.3}	0.67 ^{+0.13} _{-0.10}	1.0 ^{+0.5} _{-0.2}
N_H (10 ²¹ H cm ⁻²)	10 ⁺¹ ₋₂	3 ⁺¹ ₋₂	1 ⁺² ₋₁	0 ^{+0.5}	0 ^{+0.3}
Flux [†] (erg s ⁻¹ cm ⁻²)	2.9 × 10 ⁻¹³	3.1 × 10 ⁻¹³	3.0 × 10 ⁻¹³	1.1 × 10 ⁻¹²	1.0 × 10 ⁻¹²
– Abundances (solar) –					
O	0.2 (fixed)	0.2 (fixed)	0.2 (fixed)	0.5 ^{+0.3} _{-0.1}	1.7 ^{+3.0} _{-0.7}
Ne	2.6 ^{+1.0} _{-0.7}	0.2 (fixed)	0.2 (fixed)	1.0 ^{+0.2} _{-0.2}	1.9 ^{+1.7} _{-0.6}
Mg	1.0 ^{+0.5} _{-0.4}	1.6 ^{+1.7} _{-0.6}	0.2 (fixed)	0.9 ^{+0.3} _{-0.2}	2.0 ^{+1.8} _{-0.8}
Si	0.2 (fixed)	0.2 (fixed)	0.2 (fixed)	0.4 ^{+0.2} _{-0.2}	0.7 ^{+1.1} _{-0.4}
Fe	0.2 (fixed)	0.9 ^{+0.5} _{-0.3}	0.2 (fixed)	0.2 (fixed)	1.0 ^{+1.1} _{-0.5}
Reduced χ^2 /d.o.f.	1.45/89	1.60/89	0.91/22	1.47/64	1.41/63

Note — Errors indicate the 90% confidence limits.

*: Defined in section 6.3.1.

†: In 0.7–10.0 keV.

‡: Pegged by the upper limit of the plasma code.

Table 6.24: Plasma parameters for 0045–734, 0057–7226, and 0103–726.

SNR	— 0045–734 —		0057–7226	— 0103–726 —	
Model*	I	II	...	I	III
V (β cm ³)	— 3.6 × 10 ⁵⁹ —		6.6 × 10 ⁵⁹	— 1.3 × 10 ⁶⁰ —	
n_e ($\beta^{-1/2}$ cm ⁻³) ..	0.69	0.23	0.18	0.17	0.097
t ($\beta^{1/2}$ yr)	(> 2.9 × 10 ⁴)	7.6 ^{+∞} _{-4.7} × 10 ⁴	1.8 ^{+∞} _{-1.2} × 10 ⁴	1.8 ^{+1.0} _{-0.7} × 10 ⁴	2.2 ^{+1.6} _{-1.0} × 10 ⁴
M_{total} ($\beta^{1/2} M_\odot$) ..	210	69	100	180	110
– Mass ($\beta^{1/2} M_\odot$) –					
O [†]	... [†]	... [†]	5.6 ^{+3.3} _{-1.1} × 10 ⁻¹	1.2 ^{+2.0} _{-0.5}
Ne	6.0 ^{+2.3} _{-1.6} × 10 ⁻¹	... [†]	... [†]	2.0 ^{+0.4} _{-0.4} × 10 ⁻¹	2.3 ^{+2.1} _{-0.7} × 10 ⁻¹
Mg	8.6 ^{+4.4} _{-3.4} × 10 ⁻²	4.6 ^{+4.9} _{-1.7} × 10 ⁻²	... [†]	6.7 ^{+2.3} _{-1.5} × 10 ⁻²	9.1 ^{+7.9} _{-3.6} × 10 ⁻²
Si [†]	... [†]	... [†]	3.3 ^{+1.6} _{-1.7} × 10 ⁻²	3.5 ^{+5.5} _{-2.0} × 10 ⁻²
Fe [†]	6.9 ^{+4.1} _{-2.3} × 10 ⁻²	... [†]	... [†]	1.2 ^{+1.4} _{-0.6} × 10 ⁻¹

Note — The uncertainty of the volume V is represented by β (which could be different for different SNRs). Errors are derived from the 90% confidence limits for τ and elemental abundances in the spectral fitting (table 6.23).

*: Defined in section 6.3.1.

†: Fixed at 0.2 solar abundance in the spectral fitting.

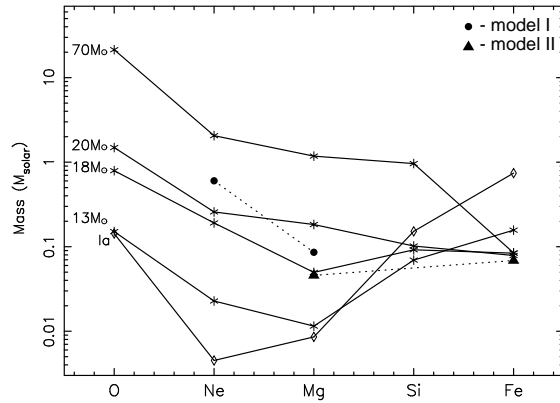


Figure 6.31: Nucleosynthesis products of various SNe overlaid with the element masses derived from the spectral analyses (table 6.24) for 0045–734. Solid lines with asterisks and diamonds represent products in type II and type Ia SNe, respectively (Tsujimoto et al. 1995). Progenitor masses of type II SNe are also indicated. Dotted lines with circles and triangles represent models I and II, respectively. Plots for elements fixed at 0.2 solar in the fitting are not presented.

6.3.2 No. 25 — 0047–735

Source and background regions for 0047–735 (No. 25) were carefully chosen to avoid contamination from the nearby pulsar AX J0049–732 (No. 26). As a result, the extracted SIS spectrum had rather poor statistics, which probably caused non-detection of emission lines (section 5.4.3). We thus used the GIS spectra (in obs. F and Q) as well to compensate for the poor statistics of the SIS spectrum, and carried out a simultaneous fit.

The spectra were well fitted to both the power-law and the CIE thermal model. However, we adopt the thermal model because the best-fit temperature is reasonable for an SNR. This fact would indicate that X-ray emission from this SNR has a thermal origin.

6.3.3 No. 66 — 0057–7226 (N66)

Although the SIS spectrum of 0057–7226 (figure 6.33) can be fitted well with an NEI model with free abundances, we obtained no constraint on the abundances due to the limited

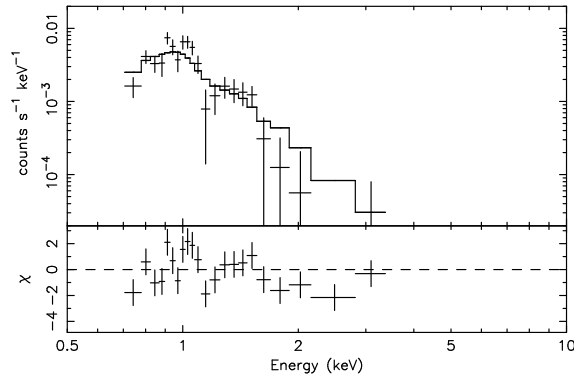


Figure 6.32: SIS spectrum of 0047–735. The crosses are data points obtained in obs. Q, while the solid line represents the best-fit model obtained by the simultaneous fitting.

Table 6.25: Spectral parameters for 0047–735 taken from table 5.5.

HR	HRerr	Obs. ID	kT	N_{H}	F_{X}	L_{X}
-1.00	1.38	F	0.86 (0.82–0.90)	0 (< 0.4)	0.14	0.060
		Q			0.11	0.048

Note — See page 55 for legends.

statistics. Therefore, we fixed the abundances at the SMC mean value (0.2 solar) and fitted the spectrum again. The best-fit parameters are given in table 6.23 (page 103).

The ROSAT HRI image is shown in figure 6.33, overlaid with the contours which indicate non-thermal radio structure. The radio emission exhibits a shell-like structure with a $\sim 3'$ diameter, while the X-rays are concentrated in the radio shell with a $\sim 2'$ diameter.

Assuming that the plasma fills a sphere with a diameter of $\sim 2'$, we obtained the volume $V = 6.6 \times 10^{59} \cdot \beta \text{ cm}^3$. With the same procedure as described in section 6.3.1, plasma parameters are obtained and given in table 6.24.

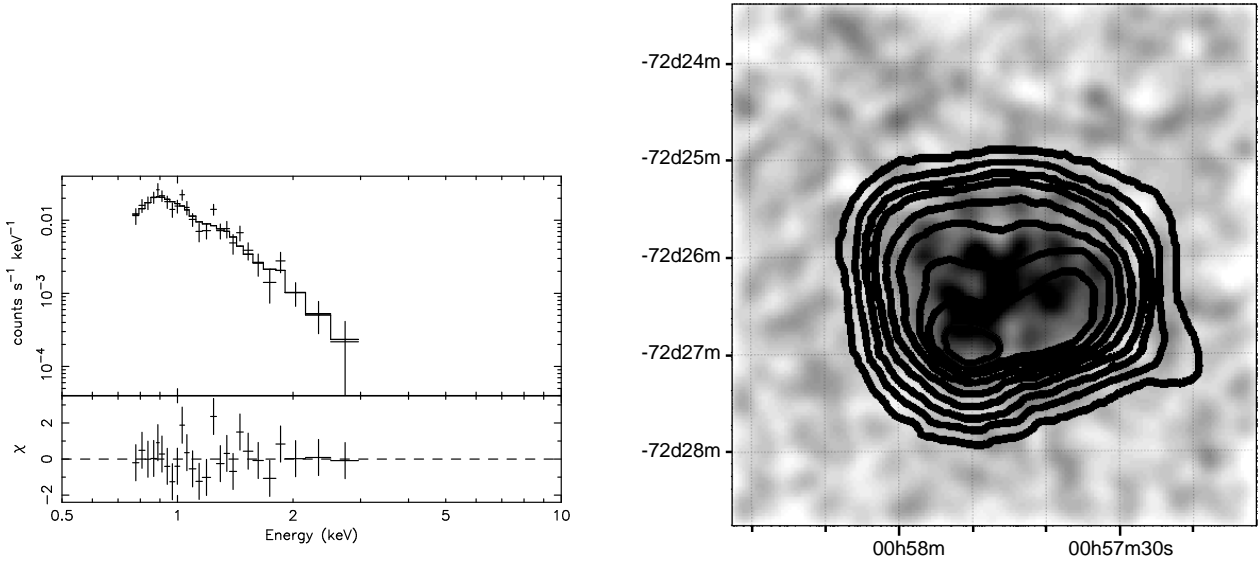


Figure 6.33: (Left) SIS spectrum of 0057–7226 obtained in obs. G (crosses) with the best-fit model (solid line). (Right) Gray-scale image around 0057–7226 obtained with ROSAT HRI. Overlaid contours represent the difference map of $H\alpha$ and MOST 843 MHz images reproduced from Ye, Turtle, & Kennicutt (1991), which selectively reveals non-thermal radio emission. The equatorial coordinates are in equinox 1950.0.

6.3.4 No. 81 — 0102–723

A detailed analysis of the SIS spectrum of SNR 0102–723 was carried out by Hayashi et al. (1994). Strong emission lines from various elements were detected, which is consistent with this SNR being young. We adopted the same model and determined its flux and luminosity in table 5.5.

6.3.5 No. 82 — 0103–726

We first fitted the SIS spectrum of 0103–726 with an NEI model, in which all abundances were fixed to the SMC mean value. This model showed bump-like residuals at energies of K-shell emission lines from O, Ne, Mg, and Si, and Fe-L lines. Therefore, we allowed the abundances of O, Mg, and Si to be free, while the abundances of Ne and Fe were treated as described in section 6.3.1 (models I–III). We did not adopt model II because this model

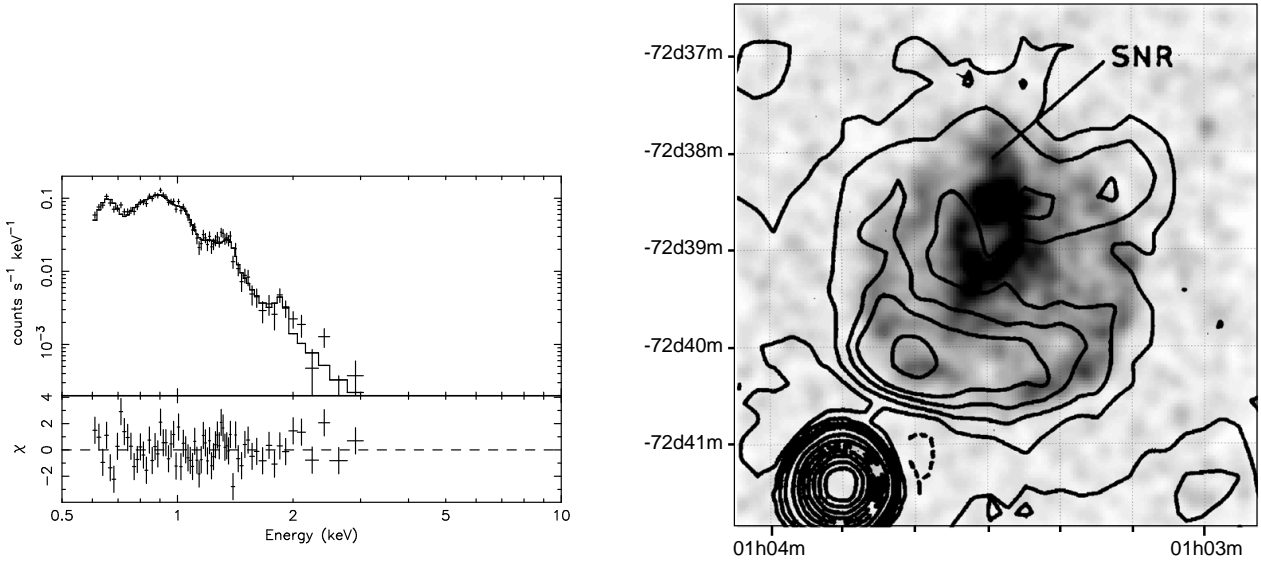


Figure 6.34: (Left) SIS spectrum of 0103–726 obtained in obs. D (crosses) with the best-fit model in case III (solid line). (Right) Gray-scale image around 0103–726 obtained with ROSAT HRI, overlaid with contours of the MOST radio image at 843 MHz (Mills et al. 1982). The equatorial coordinates are in equinox 1950.0.

gave a much worse fit than models I and III, with a reduced $\chi^2 = 1.94$ for 64 d.o.f. (see table 6.23). In both models (I and III), abundances are larger than the SMC mean value. The best-fit model is shown in figure 6.34.

The ROSAT HRI image is shown in figure 6.34, overlaid with the radio contours at 843 MHz. The radio emission has a faint shell with a diameter of $\sim 3'$, with enhanced emission at the SE part. The X-rays also show faint emission along the radio shell, in addition to the more prominent emission near the center of the radio shell.

Assuming that the plasma fills a sphere with a diameter of ~ 2.5 , we obtained the volume $V = 1.3 \times 10^{60} \cdot \beta \text{ cm}^3$. With the same procedure as described in section 6.3.1, plasma parameters are obtained and given in table 6.24.

For the same reason described in section 6.3.1, we compared the element masses with the theoretical predictions as shown in figure 6.35. A type Ia origin is rejected and a type II SNe with a progenitor mass of $\lesssim 20M_{\odot}$ is preferred, similar to 0045–734.

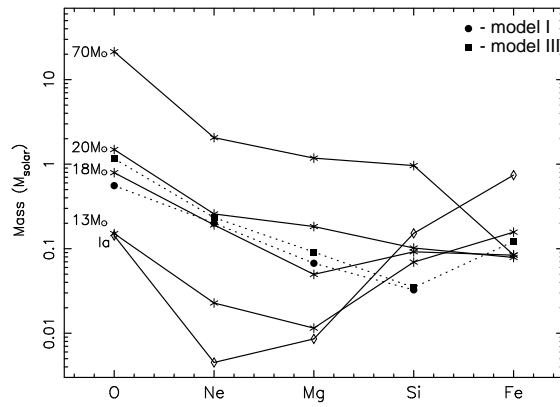


Figure 6.35: Nucleosynthesis products of various SNe overlaid with the element masses derived from the spectral analyses (table 6.24) for 0103–726. Solid lines with asterisks and diamonds represent products in type II and type Ia SNe, respectively (Tsujiimoto et al. 1995). Progenitor masses of the type II SNe are also indicated. Dotted lines with circles and squares represent models I and III, respectively. Plots for elements fixed at 0.2 solar in the fitting are not presented.

6.4 SNRS – II: from GIS

6.4.1 No. 23 — 0046–735

Both a power-law model and a thermal CIE model describe the GIS spectrum well due to highly limited statistics. However, we adopted a thermal model because the derived temperature is reasonable for an SNR; the thermal nature of this SNR is thus suggested.

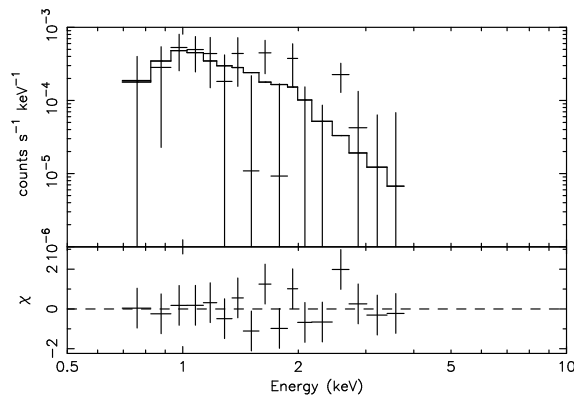


Figure 6.36: GIS spectrum of 0046–735. The crosses are data points obtained in obs. Q, while the solid line represents the best-fit model.

Table 6.26: Spectral parameters for 0046–735 taken from table 5.5.

HR	HRerr	Obs. ID	kT	N_{H}	F_{X}	L_{X}
-0.62	0.36	Q	0.9 (0.1–1.8)	0 (< 15)	0.058	0.025

Note — See page 55 for legends.

6.4.2 No. 36 — 0049–736

In our earlier study (Yokogawa et al. 2000e), this SNR was regarded as a thermal SNR because of its soft spectrum, although no emission lines were detected due to highly limited statistics. Data from new observations (L and Q) allowed us to detect emission lines (see section 5.4.3), and thus the thermal nature is now established. The GIS spectra were well

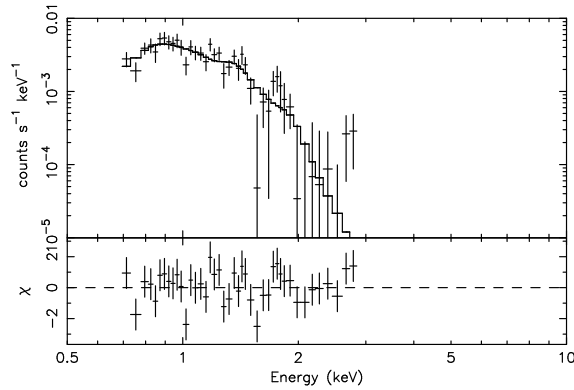


Figure 6.37: GIS spectrum of 0049–736. The crosses are data points obtained in obs. Q, while the solid line represents the best-fit model obtained by the simultaneous fitting.

Table 6.27: Spectral parameters for 0049–736 taken from table 5.5.

HR	HRerr	Obs. ID	kT	N_{H}	F_{X}	L_{X}
-0.92	0.07	F	0.23 (0.18–0.47)	6 (2–7)	0.64	1.8
		L			0.65	1.8
		Q			0.74	2.0

Note — See page 55 for legends.

fitted to a CIE thermal model, and the best-fit parameters are given in table 6.27. The bump-like residuals are found at ~ 1.9 keV (figure 6.37), which corresponds to the energy of the emission line from He-like Si. However, allowing the Si abundance to be free did not improve the result within the statistical error.

6.4.3 No. 64 — 0056–725

Since fitting the spectrum with a thin thermal plasma model yielded an unusually high temperature of ~ 20 keV, we adopted a power-law model. There is a possibility that X-rays from 0056–725 actually have a non-thermal origin.

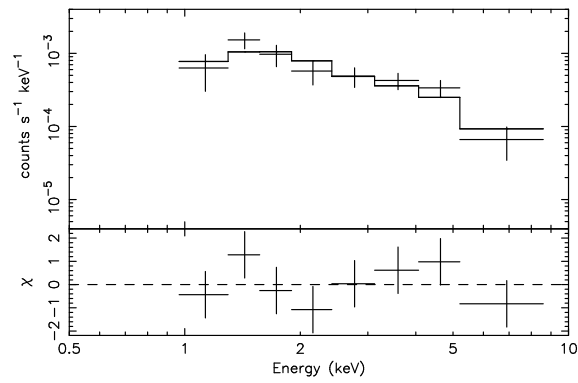


Figure 6.38: GIS spectrum of 0056–725. The crosses are data points obtained in obs. G, while the solid line represents the best-fit model.

Table 6.28: Spectral parameters for 0056–725 taken from table 5.5.

HR	HRerr	Obs. ID	Γ	N_{H}	F_{X}	L_{X}
0.20	0.12	G	1.5 (1.0–2.3)	2 (< 12)	0.34	0.16

Note — See page 55 for legends.

6.5 Other Interesting Sources

6.5.1 No. 20 — IKT1

We tentatively consider No. 20, RX J0047.3–7312, and IKT1 to be identical simply because of the positional coincidence. Haberl & Sasaki (2000) proposed RX J0047.3–7312 as a Be/X-ray binary candidate because this source exhibits a flux variation with a factor of 9 and has an emission line object as a counterpart.

The GIS spectra in two observations (F and Q) are hard, having a photon index of ~ 1 , which is typical of Be/X-ray binaries. In addition, a flare-like behaviour is found from the light curve in obs. Q (figure 6.40). These results further strengthen the Be/X-ray binary scenario.

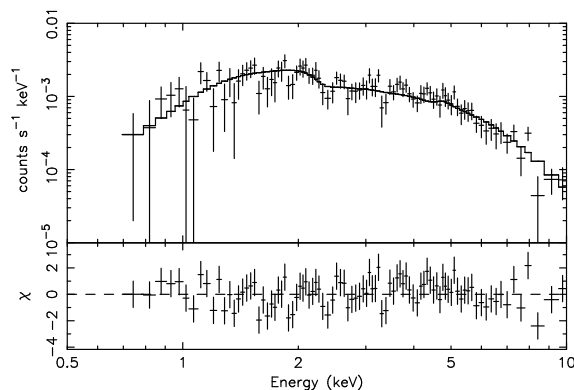


Figure 6.39: GIS spectrum of IKT1. The crosses are data points obtained in obs. Q, while the solid line represents the best-fit model derived from the simultaneous fitting.

Table 6.29: Spectral parameters for IKT1 taken from table 5.5.

HR	HRerr	Obs. ID	Γ	N_{H}	F_{X}	L_{X}
0.39	0.03	F	1.0 (0.9–1.2)	4 (1–7)	0.67	0.32
		Q			1.4	0.65

Note — See page 55 for legends.

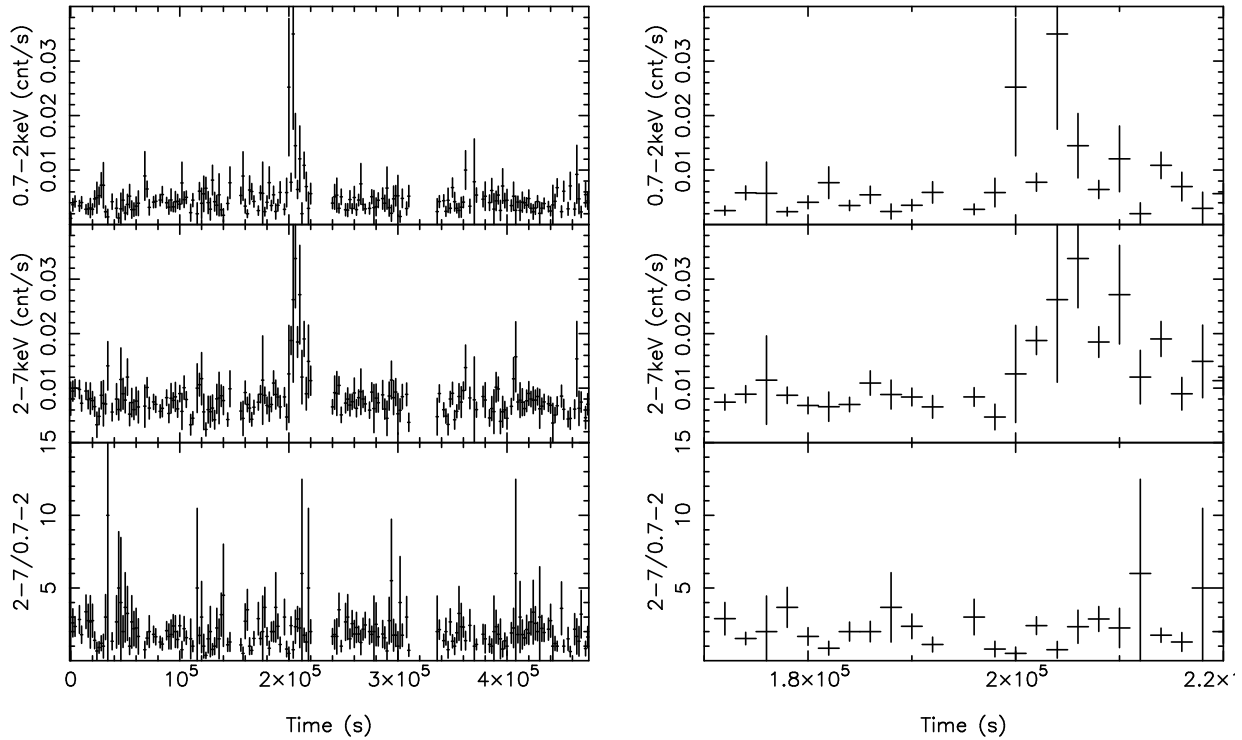


Figure 6.40: Light curves of IKT1 in obs. Q with a bin time of 2000 s. The upper and middle panels present the light curves in the soft (0.7–2.0 keV) and hard (2.0–7.0 keV) bands, respectively. The lower panels present the ratio of the two bands. A flare-like activity is found at the time $\sim 2 \times 10^5$ s; the right panel shows the time zone around the flare.

6.5.2 No. 22 — AX J0048.2–7309

No. 22 (AX J0048.2–7309) was detected in two observations (F and Q) and shows a hard spectrum ($\Gamma \sim 1$) and a flux variability with a factor of ~ 5 (table 6.30). In addition, we found an emission line object, No. 215 in Meyssonier & Azzopardi (1993), in the error circle of AX J0048.2–7309. All the information suggests that this source is probably a Be-XBP. Follow-up observations for pulsation searches and optical identification are thus encouraged.

Although the GIS spectra were well fitted to a simple power-law (figure 6.41 (a)), there remains a bump-like residual in the vicinity of 6–7 keV. In order to examine the existence of an emission line, we used only the data of obs. Q, which has much better statistics. We added a narrow Gaussian and fitted the spectrum (figure 6.41 (b)), and then determined

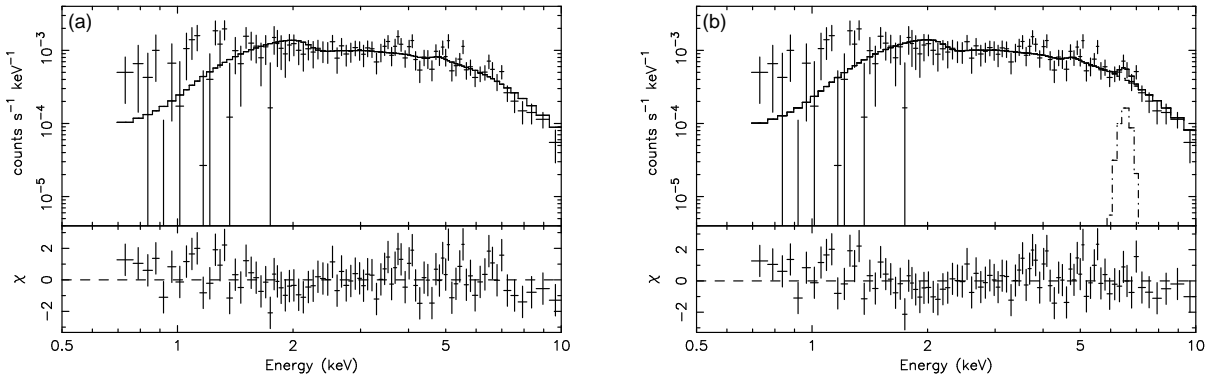


Figure 6.41: GIS spectra of AX J0048.2–7309. The crosses are data points obtained in obs. Q, while the solid lines represent the best-fit models described in the text; a power-law without a Gaussian (a), and with a Gaussian (b). Spectral components are indicated by the broken lines in (b).

Table 6.30: Spectral parameters for AX J0048.2–7309 taken from table 5.5.

HR	HRerr	Obs. ID	Γ	N_{H}	F_{X}	L_{X}
0.59	0.05	F	0.8 (0.6–1.1)	9 (3–17)	0.20	0.099
		Q			1.1	0.52

Note — See page 55 for legends.

the center energy and the equivalent width of the Gaussian to be 6.6 (6.4–6.9) keV and 240 (40–440) eV, respectively. However, the significance of the Gaussian is only $\sim 90\%$ in the F -test, thus the existence of the emission line is still not clear. Confirmation of the existence of the emission line would further strengthen the X-ray binary nature of this source.

6.5.3 No. 105 — AX J0128.4–7329

No. 105 (AX J0128.4–7329) is located near the center of an expanding supergiant shell, SMC-1, which has a diameter of $\sim 1^\circ$ (Meaburn 1980). Wang & Wu (1992) reported that the X-ray emission from AX J0128.4–7329 appears to be diffuse in an Einstein IPC image, and that the spectral hardness ratio indicates a temperature of ~ 0.8 keV if the absorption

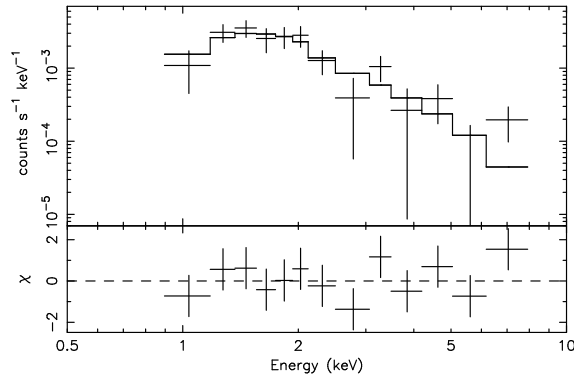


Figure 6.42: GIS spectrum of AX J0128.4–7329. The crosses are data points obtained in obs. O, while the solid line represents the best-fit model.

Table 6.31: Spectral parameters for AX J0128.4–7329 taken from table 5.5.

HR	HRerr	Obs. ID	Γ	N_{H}	F_{X}	L_{X}
-0.06	0.12	O	2.8 (1.7–4.8)	7 (< 20)	0.34	0.29

Note — See page 55 for legends.

column density is $3 \times 10^{20} \text{ cm}^{-2}$.

Since the GIS spectrum (figure 6.42) has rather limited statistics, no rigid constraint was obtained for the spectral parameters. When we fitted the spectrum with a CIE thermal model, a temperature of 2.6 (0.9–10) keV was obtained, which is marginally consistent with the argument of Wang & Wu (1992). Since half the GIS FOV is polluted by stray light that is probably from SMC X-1, it is difficult to know the extent of AX J0128.4–7329.

Chapter 7

Source Classification

7.1 Criteria for Source Classification

We classify the 106 ASCA sources into several source classes, which are given in the last column of table 5.3. In this section, we give the definitions of the classes.

XBPs (“BP” in table 5.3) are the 22 pulsars having a long pulse period (~ 1 –1000 s), hard spectrum ($\Gamma \sim 1$), flux variability, and/or an optical counterpart, as described in section 6.1; 17 of the 22 were detected with ASCA. Pulsars which are not definitely regarded as XBPs are designated as “P”. Thermal SNRs (“TS”) are the five SNRs from which emission lines of ionized atoms were detected in section 5.4.3. The other SNRs with no significant emission line are classified as radio SNRs (“RS”). Candidates for XBPs and thermal SNRs (“BPe” and “TSc”) are defined in section 7.2.3.

Nonpulsating HMXBs (“NH”) and candidates (“NHc”) are defined by the optical counterparts and flux variability as summarized in table 7.1. Grades from A to E are assigned according to the following criteria. Grade A and B sources are X-ray sources with a Be or a supergiant star companion. Flux variability has been known for grade A’s while not for grade B’s. Grade C and D sources consist of X-ray sources having an emission line object (Be star candidate) as a counterpart, which are catalogued in Haberl & Sasaki (2000). Again, flux variability has been known for grade C’s while not for grade D’s. Grade E sources also have an emission line object counterpart, but there are other possibilities (AGN or active corona of a late type star) for the nature of the sources. In table 5.3, we designate grade A

Table 7.1: Nonpulsating HMXBs and likely candidates in the SMC.

Number		Name	Optical Identification*	Variability [†]	Grade
ASCA	HS00				
...	1	RX J0032.9–7348	Be	Yes (KP96)	A
...	22	SMC X-3	Be ^a	Yes (CDL78)	A
...	...	1H 0103–762	Be ^b	Yes (KP96)	A
...	42	RX J0101.0–7206	Be	Yes (KP96)	A
...	...	EXO 0114.6–7361	B (SG) ^c	Yes (WW92)	A
...	24	2E 0051.1–7304	Be	Yes? (WW92)	B
63	38	RX J0058.2–7231	Be	...	B
...	...	RX J0106.2–7205	Be ^d	...	B
20	6	RX J0047.3–7312 (IKT1)	Be?	Yes (HS00, ASCA, flare [‡])	C
22	...	AX J0048.2–7309 [§]	Be? ^e	Yes (ASCA)	C
50	30	RX J0054.9–7245	Be?	Yes (HS00)	C
...	36	RX J0057.8–7207	Be?	Yes (HS00)	C
...	44	RX J0101.6–7204	Be?	Yes (HS00)	C
76	45	RX J0101.8–7223	Be?	Yes (HS00)	C
...	50	RX J0103.6–7201	Be?	Yes (HS00)	C
...	53	RX J0105.1–7211	Be?	Yes (FHPM00)	C
87	56	RX J0107.1–7235	Be?	Yes (HS00)	C
...	2	RX J0041.2–7306	Be?	...	D
...	3	RX J0045.6–7313	Be?	...	D
...	8	RX J0048.5–7302	Be?	...	D
28	11	RX J0049.5–7331	Be?	Yes? (ASCA)	D
...	14	RX J0050.7–7332	Be?	...	D
35	15	RX J0050.9–7310	Be?	...	D
...	17	RX J0051.3–7250	Be?	...	D
...	21	No. 26 in WW92	Be?	...	D
...	26	RX J0053.4–7227	Be?	...	D
...	29	RX J0054.5–7228	Be?	...	D
...	32	2E 0054.4–7237 (IKT13)	Be?	...	D
...	34	2E 0055.8–7229 (IKT15)	Be?	...	D
...	37	RX J0057.9–7156	Be?	...	D
...	51	RX J0104.1–7243	Be?	...	D
...	52	RX J0104.5–7121 [¶]	Be?	...	D
...	54	RX J0105.7–7226	Be?	...	D
85	55	RX J0105.9–7203	Be?	...	D
...	60	RX J0119.6–7330	Be?	...	D
...	5	RX J0047.3–7239	Be?AGN? ^{**}	...	E
...	18	RX J0051.8–7159	Be?AC? ^{††}	...	E

Note — In table 5.3, we designate grade A and B sources as NH and grade C and D sources as NHc.

*: References are found in Haberl & Sasaki (2000), except for the five sources marked with *a–e*. (*a*) Crampton, Hutchings, & Cowley 1978; (*b*) Whitlock & Lochner 1994; (*c*) Wang & Wu 1992 (SG=supergiant); (*d*) Hughes & Smith 1994; (*e*) this work (No. 215 in MA93 is located 23'' from the ASCA position).

†: For sources with a “Yes” sign, flux variability has been detected by KP96 (Kahabka & Pietsch 1996), CDL78 (Clark et al. 1978), WW92 (Wang & Wu 1992), HS00 (Haberl & Sasaki 2000), ASCA (this work), and FHPM00 (Filipović et al. 2000).

‡: Flaring behaviour is detected in obs. Q (see section 6.5.1).

§: Fe line is marginally detected in obs. Q (see section 6.5.2).

¶: This source is designated as RX J0104.5–7121 in HS00 (section 6.4), but probably should be RX J0104.5–7221 according to its coordinate.

** : A point-like radio source is also located in the error circle, thus the possibility that it is an AGN remains (HS00).

†† : X-ray emission may be attributable to an active corona (AC) of a late type star (HS00).

and B sources as “NH” and grade C and D sources as “NHc”.

Foreground stars (“FS”) and AGN candidates (“AGN”) are defined merely based on positional coincidence of ROSAT sources in these classes (see Sasaki, Haberl, & Pietsch 2000 and references therein). Sources which do not fall into any classes are designated as “UN” (unclassified sources).

7.2 Classification by Hardness Ratio

7.2.1 XBPs and thermal SNRs

The source classes most rigidly defined in this study are XBPs and thermal SNRs. For a statistical discussion, more samples of thermal SNRs are needed because there are only five thermal SNRs in the SMC. X-ray sources in the LMC are suitable for inclusion for the reason described in section 7.2.2. Therefore, we included ASCA data of XBPs and thermal SNRs in the LMC, which are systematically analyzed by Nishiuchi (2001). Four XBPs in the LMC have been detected with ASCA: EXO 053109–6609.2, LMC X-4, A0538–67, and 1SAX J0544.1–710. From these, flux variability and optical counterparts have been detected (Bildsten et al. 1997; Burderi et al. 1998; Cusumano et al. 1998; Haberl, Dennerl, & Pietsch 1995; Corbet et al. 1997). Although pulsations were not detected from the ASCA data of A0538–67, this source is very likely a Be-XBP (Corbet et al. 1997, and references therein). ASCA has detected over 20 SNRs in the LMC. Among them, 10 SNRs analyzed by Hughes et al. (1995) and Hughes, Hayashi, & Koyama (1998) are well-established thermal SNRs (N103B, 0509–67.5, 0519–69.0, N23, N49, N63A, DEM71, N132D, 0453–68.5, and N49B). Two other classes of sources, Crab-like SNRs¹ (0540–69 and N157B) and BH binaries (LMC X-1 and LMC X-3), have also been detected with ASCA, and are included in our discussion.

Spectral parameters for the four XBPs, 10 thermal SNRs, two Crab-like SNRs, and two BH binaries in the LMC were derived by Nishiuchi (2001), almost in the same way as we did for the SMC sources. In figure 7.1, we show a plot of HR for these classes against observed luminosity L_{obs} , defined as $L_{\text{obs}} = F_x \times 4\pi d^2$, where d is the distance to the SMC (60 kpc) or LMC (50 kpc). Sources detected multiple times are represented by single points, which

¹We use “Crab-like SNRs” to refer to SNRs associated with a rotation-powered X-ray pulsar.

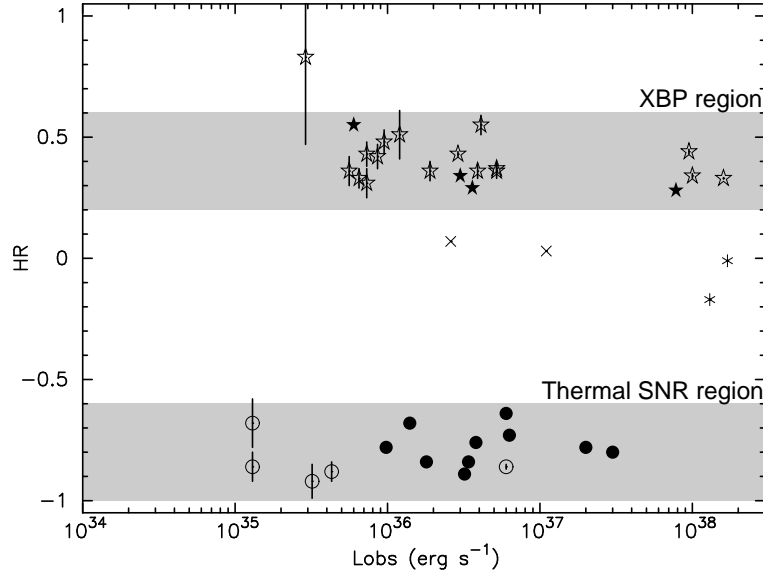


Figure 7.1: Plot of HR against L_{obs} (0.7–10.0 keV) for XBP, thermal SNRs, Crab-like SNRs, and BH binaries. The symbols represent XBP (stars), thermal SNRs (circles), Crab-like SNRs (crosses), and BH binaries (asterisks). Open and filled symbols are for the SMC and LMC, respectively. Sources detected multiple times are represented by single points, which correspond to the largest L_{obs} of each source. The source at $\text{HR} = 0.83$ is No. 43, which is positionally coincident with XBP RX J0052.1–7319, but does not exhibit coherent pulsations in the ASCA data.

correspond to the largest L_{obs} of each source. Thanks to the LMC samples, the number of thermal SNRs is enhanced, and so a clear split between XBP and thermal SNRs could be found. We can safely say that in the Magellanic Clouds, XBP fall in a narrow region of $0.2 \lesssim \text{HR} \lesssim 0.6$ (“XBP region”), while thermal SNRs fall in the region $-1.0 \lesssim \text{HR} \lesssim -0.6$ (“thermal SNR region”). The source located above the XBP region (at $\text{HR} = 0.83$) is No. 43, which is positionally coincident with XBP RX J0052.1–7319, but does not exhibit coherent pulsations in the ASCA data. Because of the large HR error and the fact that there are no pulsations, we ignored this source when defining the XBP region.

We also show the $\text{HR}-L_{\text{obs}}$ plot for the other sources in figure 7.2, i.e., nonpulsating HMXBs, radio SNRs (not regarded as thermal), pulsars (not regarded as XBP), sources coincident with AGNs and foreground stars, and the remaining unclassified sources. Although some sources have very large HR errors, we find that most of the sources tend to be located

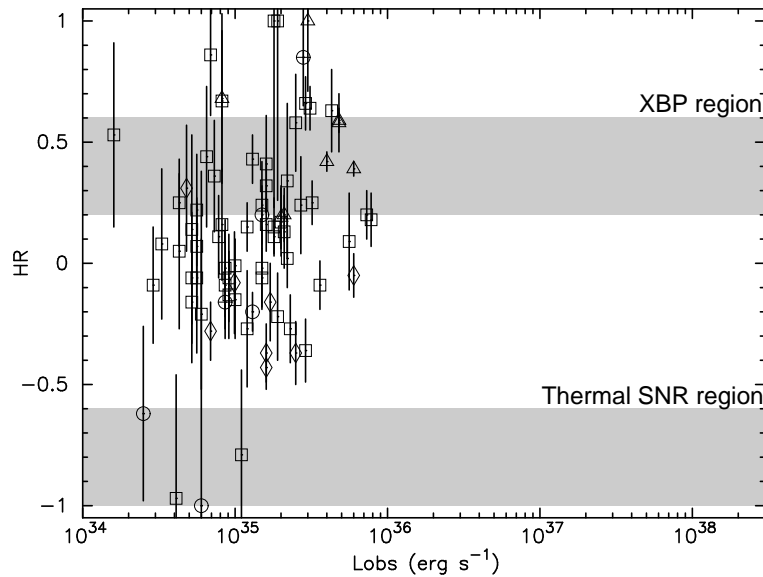


Figure 7.2: Plot of HR against L_{obs} (0.7–10.0 keV) for the SMC sources not plotted in figure 7.1. The symbols represent nonpulsating HMXBs and their candidates (triangles), radio SNRs not regarded as thermal (dotted circles), pulsars not regarded as XBPs (circles with a plus sign), sources coincident with AGNs and foreground stars (diamonds), and other unclassified sources (squares). Sources detected multiple times are represented by single points, which correspond to the largest L_{obs} of each source.

in the XBP region and between the XBP and thermal SNR regions.

7.2.2 Validity of the classification by hardness ratio

The spectral hardness ratio has been used as an aid for classification of X-ray sources (e.g., Wang & Wu 1992; Haberl et al. 2000). We should note that the hardness ratios used in their/our studies are defined only by the number of detected photons. Therefore, a strong point of the classification by hardness ratio is that it is independent of any spectral models. However, there could be uncertainty from interstellar absorption, which reduces the soft photon flux and thus makes the spectra harder. Below we show that interstellar absorption does not affect our HR classification method when applied to the Magellanic Cloud sources, but does have an effect if applied to sources in our Galaxy.

We simulated HRs for simple spectra of thin-thermal plasma with a temperature of 0.5 keV, a typical value for a thermal SNR, and of a power-law with a photon index of 1.0, a typical value for an XBP. For an absorption column density of $3 \times 10^{21} \text{ cm}^{-2}$, which roughly corresponds to a distance of 1 kpc in our Galaxy, HRs are -0.89 and 0.36 for the thermal and power-law model, respectively. For a larger absorption column density of $8 \times 10^{22} \text{ cm}^{-2}$, which is equivalent to the Galactic center region, the HR of the thermal model and the power-law model increases to 0.5 and 0.96 , respectively. We therefore conclude that in our Galaxy, HR values can have a large scatter even for the same source class, depending on the source distances. On the other hand, according to H I observations made by Luks (1994), we can safely assume that the interstellar absorption is rather uniform towards the SMC and LMC with a scale down to $15'$ (HPBW). In fact, the H I column density derived by Luks (1994) was $\sim 1 \times 10^{20} - 7 \times 10^{21} \text{ cm}^{-2}$. Within this N_{H} range, HR values show little variation: -0.94 to -0.81 for thin-thermal spectra, and 0.25 to 0.48 for power-law spectra. Thus we conclude that the possible uncertainty in HR due to the N_{H} spatial variation is smaller than the width of the XBP region and thermal SNR region, hence the present classification by HR value should be reliable for X-ray sources in the Magellanic Clouds.

7.2.3 Candidates for XBPs and thermal SNRs

In the HR– L_{obs} plot (figure 7.1), no thermal SNRs are found in the XBP region, nor vice versa. In addition, Crab-like SNRs and BH binaries are not found in these two regions. Therefore, we can regard sources in the XBP (or thermal SNR) region as candidates for XBPs (or thermal SNRs). In figure 7.3, we show the HR– L_{obs} plot for all sources in the SMC and for the selected LMC sources. We find 20 XBP candidates and four thermal SNR candidates, which are designated as BPc and TSc in table 5.3, respectively. We excluded No. 91 from the XBP candidates because it is identified with an AGN. Although the HRs of No. 2 and No. 13 are -1^2 , we do not classify them as thermal SNRs because of their large HR errors. No. 25 also has a large HR error (HR = -1.00 ± 1.38), but we classify this source as a thermal SNR because its SIS spectrum is typical of this class and because it has a radio SNR counterpart (0047–735).

Nonpulsating HMXBs and their candidates (table 7.1) are all located within or near the XBP region, thus are very promising targets for pulsation searches. Non-detection of pulsations from these sources is very likely due to the poor statistics. Detection of pulsations from

²These sources are not plotted in figure 7.2 and 7.3 because L_{obs} is not derived (see section 5.4.5).

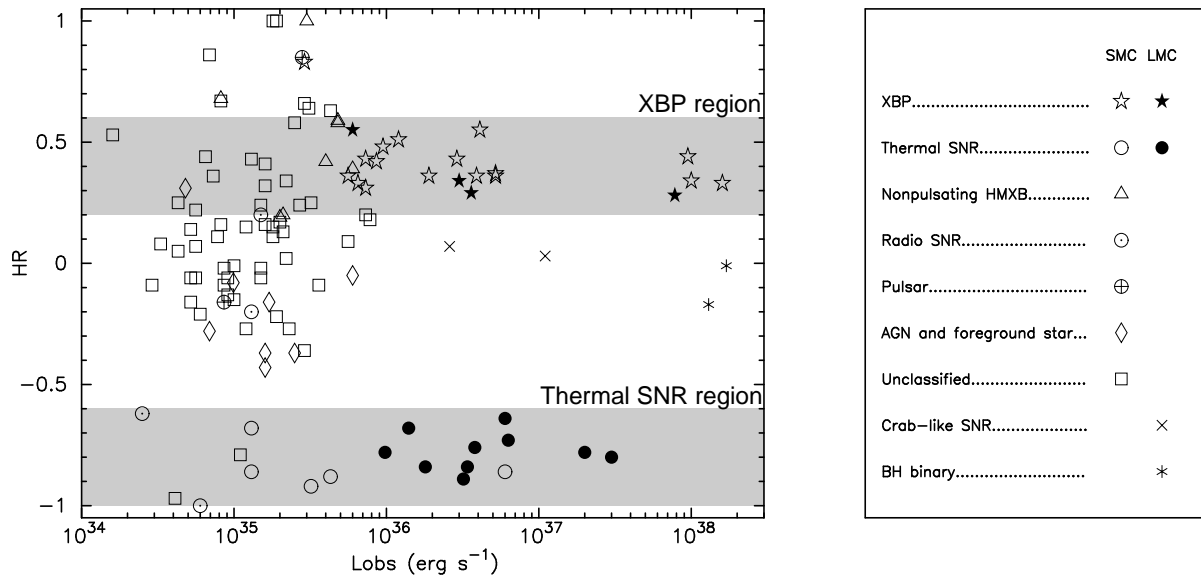


Figure 7.3: Plot of HR against L_{obs} (0.7–10.0 keV) for all sources in the SMC. Legends for the symbols are given in the right panel. Sources detected multiple times are represented by single points, which correspond to the largest L_{obs} of each source. HR errors for the unclassified sources are mostly $\sim \pm 0.2$ (see figure 7.2).

low flux sources AX J0049.5–7323, AX J0051.6–7311, and RX J0101.3–7211 demonstrates well the necessity of high sensitivity observations (see sections 6.1.5, 6.1.8, and 6.1.17).

Two radio SNRs (0046–735 and 0047–735) are found among the thermal SNR candidates. These SNRs have very limited statistics, and thus were not classified as thermal SNRs in section 5.4.3. Another radio SNR, 0056–725, is located within the XBP region. Therefore, X-rays from this source may be attributed to an unresolved XBP in the radio SNR 0056–725, such as 1SAX J0103.2–7209.

Crab-like SNRs, BH binaries, and sources coincident with AGNs or foreground stars are mostly located between the XBP and thermal SNR regions (except for No. 91 in the XBP region, but it has a rather large HR error of ± 0.26). We find 33 unclassified sources in this regime; are they located within the SMC, or are they background/foreground sources? Ueda et al. (1999) carried out the ASCA Medium-Sensitivity Survey and derived the $\log N$ – $\log S$ relation with a sensitivity limit of $6 \times 10^{-14} \text{ erg s}^{-1} \text{ cm}^{-2}$ (0.7–7 keV). It is difficult

to obtain an accurate detection limit for our survey because of various uncertainties, such as contamination from bright sources, and the position-dependent efficiency of the detector. Therefore, we only make a rough estimation from figure 7.3 that the detection limit for background sources in our SMC survey is 10^{-13} – 10^{-12} $\text{erg s}^{-1} \text{cm}^{-2}$ (4×10^{34} – 4×10^{35} erg s^{-1}). With this limit, several AGNs would be detected in the GIS FOV in each observation (Ueda et al. 1999), thus we can expect that several tens of AGNs would be detected in our SMC survey. Therefore, it is likely that most of the 33 unclassified sources in the medium HR regime are background AGNs. This conclusion is independently supported by the spatial distribution of these sources, as shown in section 8.2.

The very hard regime ($\text{HR} > 0.6$) contains seven unclassified sources. Even if a source has a hard spectrum with $\Gamma = 1.0$, a large absorption column of $N_{\text{H}} > 10^{22}$ cm^{-2} is required for HR to exceed 0.6. Therefore, we regard these seven very hard sources as highly absorbed objects, although a possibility that they are XBP candidates could not be rejected due to the large HR error (see figure 7.2).

Chapter 8

Implication for the Star Forming Activity

8.1 Source Populations in the SMC and in our Galaxy

8.1.1 Basic data

We have shown that most of the SMC sources detected with ASCA are classified as XBPs (mostly Be-XBPs), nonpulsating HMXBs, and SNRs, in addition to foreground stars and background AGNs. In order to make a comparison of source populations in the SMC and in our Galaxy, we combined the results of our study with various catalogues compiled by other authors. The source classes included in this discussion are summarized in table 8.1: HMXBs (XBPs and nonpulsating HMXBs), LMXBs, and SNRs (Crab-like and others).

HMXBs in the SMC consist of 22 XBPs (section 6.1) and eight nonpulsating HMXBs (grades A and B in table 7.1). Candidates for HMXBs are a combination of the 20 XBP candidates defined in this study (BPc in table 5.3) and the grade C and D sources in table 7.1. Here we regard the XBPs (and candidates) with an unknown optical counterpart as HMXBs, because most XBPs hitherto found are HMXBs (e.g., Bildsten et al. 1997). Evidence for LMXBs has not been detected from any source in the SMC. SNRs in the SMC have been surveyed by Mathewson et al. (1983; 1984) in the radio band and later by Filipović et al. (1998a) in both the radio and X-ray bands; as a result 14 SNRs have been detected. Five SNR candidates have been found by Filipović et al. (1998b) and Haberl et al. (2000). In

Table 8.1: Source populations in the SMC and in our Galaxy.

	HMXBs			LMXBs	SNRs		
	XBPs	Nonpulse	Candidates		Crab-like	Other	Candidates
Galaxy	53	30	...	130	10	220	100
Galaxy $\times 1/100^*$	0.53	0.3	...	1.3	0.1	2.2	1
SMC	22	8	41	0	0	14	7

*: Since the mass of the SMC is about 1/100 of that of our Galaxy, the source numbers in our Galaxy should be divided by 100 for a simple comparison.

addition, two thermal SNR candidates defined in this study (No. 6 and No. 45) have no radio SNR counterpart, thus are candidates for new SNRs. No evidence for Crab-like SNRs has been found.

HMXBs and LMXBs in our Galaxy are catalogued by Liu, van Paradijs, & van den Heuvel (2000, 2001; BH binaries are also included). We find 49 XBPs, ~ 30 nonpulsating HMXBs, and ~ 130 LMXBs in those catalogues. We also include four new XBPs, AX J1740.1–2847, XTE J1543–568, SAX J2239.3+6116, and AX 1841.0–0536 (Sakano et al. 2000; Finger & Wilson 2000; In 't Zand et al. 2001; Bamba et al. 2001). Green (2000) has compiled a most complete catalogue of 225 radio SNRs in our Galaxy. Among them, about 10 are associated with a rotation-powered X-ray pulsar, thus are regarded as Crab-like SNRs. In addition, some new SNRs have been discovered in the X-ray band with ROSAT and ASCA. We tentatively expect 100 SNR candidates to be discovered in the near future (e.g., Aschenbach 1996).

8.1.2 Comparison of the source populations

Based on table 8.1, we compare the source populations in the SMC and in our Galaxy from various aspects.

Since the mass of the SMC is about 1/100th the mass of our Galaxy, the source numbers in our Galaxy should be divided by 100 for a simple comparison (as in the second row of table 8.1). Accordingly, we find that the normalized number of HMXBs is much higher in the SMC. On the other hand, the normalized numbers of LMXBs are comparable in the two galaxies. Since the detection limit of our survey is $\sim 10^{35}$ erg s $^{-1}$ (see figure 7.3), the typical luminosity ranges of HMXBs and LMXBs has been covered. Hard X-rays from HMXBs brighter than

$\sim 10^{35}$ erg s $^{-1}$ can penetrate the thick interstellar matter in our Galaxy. Although LMXBs have softer spectra, they are mainly distributed at high Galactic latitudes, thus the Galactic interstellar absorption is again neglectable. Therefore, the discrepancy/similarity of the normalized numbers of HMXBs/LMXBs are not attributable to a selection effect. LMXBs are probably much older than HMXBs because they have properties such as weak magnetic fields and spatial distribution outside active star forming regions (e.g., Lewin, van Paradijs, & Taam 1995). Therefore, we propose that (1) in a very old epoch ($\gtrsim 10^9$ yr ago) the star forming rate in the SMC was similar to that in our Galaxy, which resulted in the similarity of the (normalized) LMXB numbers, and then (2) more recently ($\sim 10^6$ – 10^7 yr ago) there was a bursting star formation only in the SMC, which resulted in the much larger (normalized) HMXB number in the SMC.

According to this proposed star forming history, the normalized number of SNRs should be higher in the SMC, similar to HMXBs. However, SNRs are rather lacking in the SMC when compared with HMXBs; the number ratio of SNRs to HMXBs is 14/30 (21/71 when the candidates are included), while it is 230/83 in our Galaxy (330/83 when the candidates are included). This fact may indicate that many SNRs in the SMC remain to be discovered. For example, as mentioned before, No. 6 and No. 45 are thermal SNR candidates with no radio SNR counterpart (the two squares in the thermal SNR region in figure 7.3). Therefore, follow-up radio observations for these objects may prove fruitful.

Both HMXBs and Crab-like SNRs are direct descendants of massive stars. However, the number ratios of these classes in our Galaxy (10/83) and in the SMC (0/30; 0/71 when the HMXB candidates are included) are significantly different. If the ratio is identical between galaxies, at least several Crab-like SNRs should be found in the SMC. According to figure 7.3, Crab-like SNRs should be located around HR ~ 0 , where those in the LMC are located. Since the unclassified sources in that HR regime are relatively faint, non-detection of pulsations may be due to limited statistics. Therefore, high sensitivity observations of those sources with a good time resolution would be fruitful. In addition, high resolution radio surveys to search for plerionic emission are also encouraged. If, on the other hand, Crab-like SNRs are really lacking in the SMC, it may be implied that the binary frequency of massive stars is much higher in the SMC because Crab-like SNRs and HMXBs are descendants of single and binary massive stars, respectively. A higher binary frequency can in part be a cause of the lower number ratio of SNRs to HMXBs mentioned above.

8.2 Spatial Distribution of Various Classes of Sources

In order to explore spatial inhomogeneity of the star forming history in the SMC, we investigated the spatial distributions of HMXBs and SNRs. These sources are produced by SNe of massive stars (except for SNRs from type Ia SNe), thus are good indicators of the recent star forming history (10^6 – 10^7 yr ago). In this section, “HMXBs” include the XBPs, nonpulsating HMXBs, and HMXB candidates in table 8.1, while “SNRs” include the Crab-like and other SNRs and SNR candidates in table 8.1.

In figure 8.1 (a) and (b), we show the spatial distributions of HMXBs and SNRs. We find that most HMXBs are concentrated in the optical main body, and $\sim 10\%$ are located in the eastern wing. Maragoudaki et al. (2000) carried out an optical survey of the SMC and derived spatial distributions of stars in seven ranges of ages (figure 2.4; page 8). Comparing figure 8.1 (a) and (b) with figure 2.4, we find that the distribution of the HMXBs well resembles that of stars with ages of 1.2 – 3×10^7 yr (figure 8.2). This is naturally expected because HMXBs are descendants of massive (young) stars with an age of $\sim 10^7$ yr. The SNRs have a distribution pattern similar to HMXBs, thus we suppose that most of the SNRs were produced by SNe of massive stars.

We also investigated the distribution of the 33 unclassified sources with medium hardness ratios ($-0.6 < HR < 0.2$; see section 7.2.3) and six AGN candidates (Nos. 52, 72, 80, 84, 91, and 92) as shown in figure 8.1 (c). The distribution is relatively uniform, which exhibits a clear contrast with HMXBs and SNRs and is qualitatively consistent with the distribution of old stars ($> 2 \times 10^9$ yr; see figure 2.4). This fact implies either that (1) most of those medium HR sources are unrelated to the SMC, i.e., background or foreground sources, or that (2) they represent a population much older than the HMXBs. Scenario (1) is consistent with the estimate from the $\log N$ – $\log S$ relation made in section 7.2.3. However, taking into account the large uncertainty in the above estimate, there still remains a possibility that some of the medium HR sources represent an older population, probably LMXBs. Since the number of LMXBs has a relatively large impact on the star forming activity in the old epoch (see section 8.1.2), follow-up observations of these medium HR sources are encouraged.

The distribution of the seven very hard sources ($HR > 0.6$) shown in figure 8.1 (d) seems to be as uniform as that of the AGN candidates and the medium HR sources, although the number of sources is highly limited. Therefore, the very hard sources may be unrelated to the SMC, i.e., background or foreground sources. Considering the suggestion that these sources

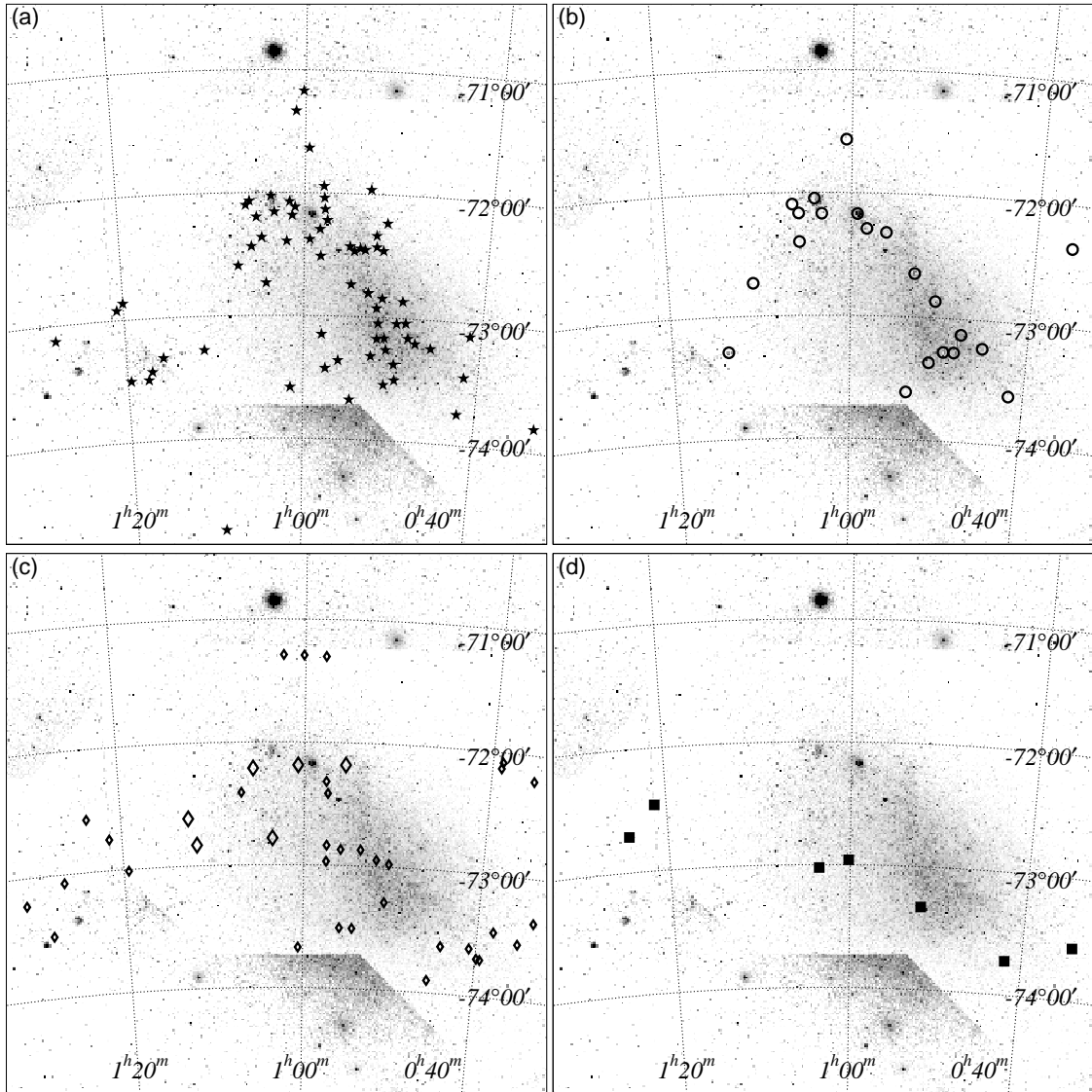


Figure 8.1: Spatial distribution of HMXBs (a: indicated by stars), SNRs (b: circles), the six AGN candidates and the 33 unclassified sources with medium HR (c: diamonds), and the seven very hard sources (d: squares), superimposed on the DSS image of the SMC. The large and small diamonds in (c) indicate the AGN candidates and the medium HR sources, respectively. The discontinuity seen in the DSS image is an artifact. Equatorial coordinates in equinox 2000.0 are overlaid.

should be highly absorbed (see section 7.2.3), we propose that most of them are seyfert 2 galaxies. We thus encourage optical follow-up observations of these sources.

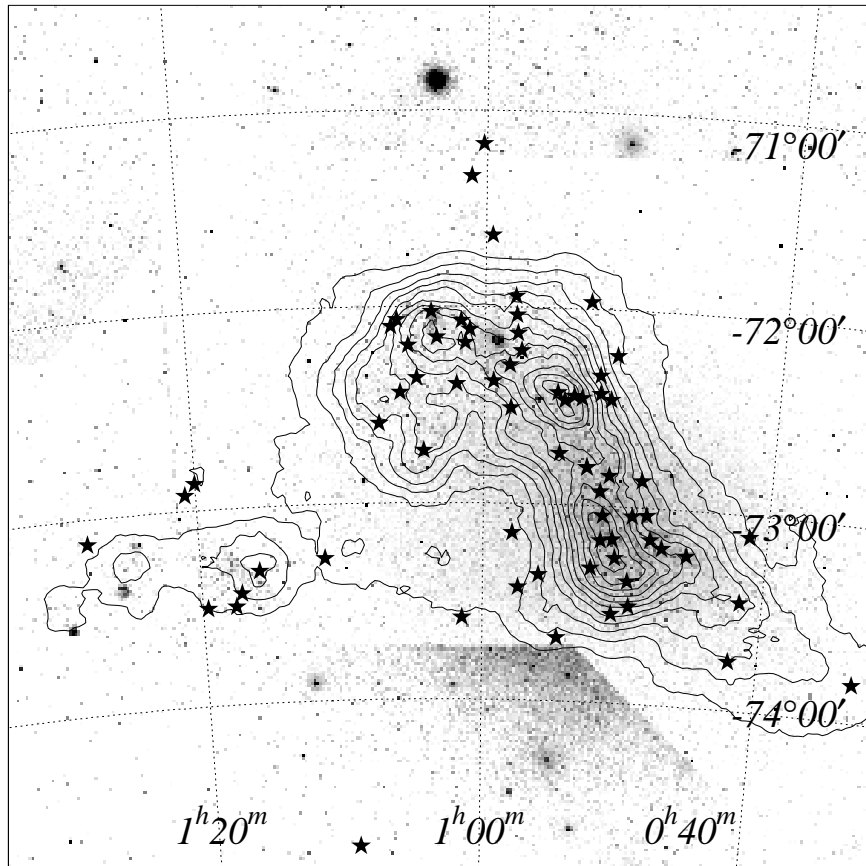


Figure 8.2: Spatial distribution of HMXBs (indicated by star-marks) and young stars ($\sim 2 \times 10^7$ yr; contours) overlaid with the DSS image of the SMC. The discontinuity seen in the DSS image is an artifact. Equatorial coordinates in equinox 2000.0 are overlaid.

Chapter 9

Conclusion

We performed systematic analyses on all the ASCA data of the SMC region. We detected 106 sources with a criterion of $S/N > 5$. Basic properties such as positions, correlation with other catalogues, and spectral parameters are compiled in the catalogue. We determined the source positions with Gotthelf et al.'s correction, and found that the 90% error radius is in practice $\sim 40''$ for sources detected in the inner circle of the GIS.

We discovered eight new X-ray pulsars and also determined precise positions for four already known X-ray pulsars. As a result, there are now 25 X-ray pulsars known in the SMC. We regarded 22 pulsars among the 25 as XBPs because of their pulse period, hard spectrum, flux variability, and, for some sources, the existence of an optical counterpart.

Among the 14 radio SNRs known in the SMC, eight were detected with ASCA. We detected emission lines of highly ionized atoms from five SNRs, and thus regarded them as thermal SNRs.

We established a simple method of source classification using the spectral hardness ratio (HR). XBPs and thermal SNRs respectively fall in a range of $0.2 \lesssim \text{HR} \lesssim 0.6$ and $-1.0 \lesssim \text{HR} \lesssim -0.6$. Other source classes such as Crab-like SNRs, BH binaries, AGNs, and foreground stars have medium hardness ratios ($-0.6 < \text{HR} < 0.2$). This method is a powerful tool for classifying faint sources which remain unclassified. With this method, we found 20 XBP candidates and four thermal SNR candidates.

We combined the results of this study with those of other catalogues to compare the source populations in the SMC and in our Galaxy. Normalized by the galaxy mass, the

number of LMXBs is consistent between the SMC and our Galaxy, while the number of HMXBs is very much higher in the SMC. This contrast indicates that in a very old epoch the star forming activity was comparable between the two galaxies, and that very recently there was a bursting star formation only in the SMC. SNRs in the SMC are not as populous as HMXBs, although the normalized number is still larger than that in our Galaxy. This may indicate that there are many SNRs in the SMC that remain to be discovered.

We derived the spatial distributions of HMXBs and SNRs, including candidates. We found that HMXBs are distributed mainly along the main body and partly in the eastern wing; this quite resembles the distribution of young ($\lesssim 2 \times 10^7$ yr) stars. SNRs also have a similar distribution, indicating that most of the SNRs are remnants of type II SNe. Medium HR sources ($-0.6 < \text{HR} < 0.2$) have, on the other hand, a relatively regular distribution. This implies that most of them are AGNs, which is also supported by the $\log N$ - $\log S$ relation derived from the ASCA Medium-Sensitivity Survey.

Appendix A

Two Color X-Ray Mosaic Image of the SMC

The mosaic images shown in figure 5.1 and 5.2 are combined into a two color image in figure A.1. Red and blue indicate X-ray photons in the soft (0.7–2.0 keV) and hard (2.0–7.0 keV) bands, respectively. Most of the “blue” or “red” sources are XBPs or thermal SNRs (including their candidates), respectively. Evidently many XBPs and the candidates are found, which is in a strong contrast between the LMC color image presented by Nishiuchi (2001).

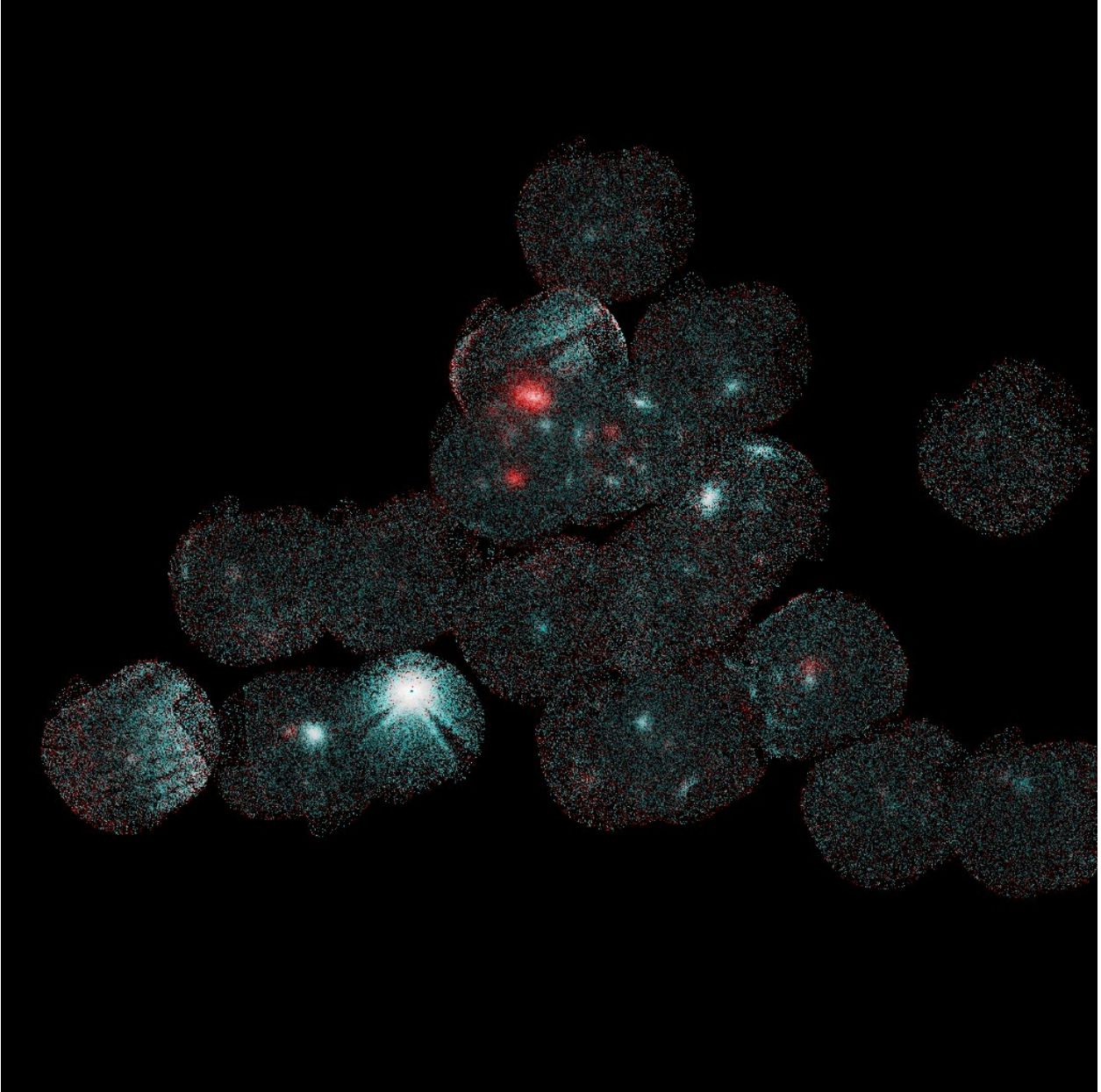


Figure A.1: Two color X-ray mosaic image of the SMC. Electronic version of this image can be obtained from <http://www-cr.scphys.kyoto-u.ac.jp/member/jun/job/phd/>.

Bibliography

- [1] Allen, W. H. et al. 1993, ApJ 403, 239
- [2] Aschenbach, B. 1996, MPE report 263, 213
- [3] Bamba, A., Yokogawa, J., Ueno, M., Koyama, K., & Yamauchi, S. 2001, PASJ in press
- [4] Bildsten, L. et al. 1997, ApJS 113, 367
- [5] Buckley, D. A. H., Coe, M. J., Stevens, J. B., van der Heyden, K., Angelini, L., White, N., & Giommi, P. 2001, MNRAS 320, 281
- [6] Burderi, L., Di Salvo, T., Robba, N. R., Del Sordo, S., Santangelo, A., & Segreto, A. 1998, ApJ 498, 831
- [7] Burke, B. E., Mountain, R. W., Daniels, P. J., Dolat, V. S., & Cooper, M. J. 1994, IEEE Trans. Nucl. Sci., 41, 375
- [8] Caldwell, J. A. R. & Coulson, I. M. 1986, MNRAS 218, 223
- [9] Chakrabarty, D., Levine, A. M., Clark, G. W. & Takeshima, T. 1998a, IAU Circ. 7048
- [10] Chakrabarty, D., Takeshima, T., Ozaki, M., Paul, B., & Yokogawa, J. 1998b, IAU Circ. 7062
- [11] Cioni, M. -R. L., Habing, H. J., & Israel, F. P. 2000, A&A 358, L9
- [12] Clark, G. W., Doxsey, R., Li, F., Jernigan, J. G., & van Paradijs, J. 1978, ApJ 221, L37
- [13] Clark, G. W., Remillard, R. A., & Woo, J. W. 1996, IAU Circ. 6305
- [14] Clark, G. W., Remillard, R. A., & Woo, J. W. 1997, ApJ 474, L111

- [15] Coe, M. J., Buckley, D. A. H., Charles, P. A., Southwell, K. A., & Stevens, J. B. 1998, MNRAS 293, 43
- [16] Coe, M. J., Haigh, N. J., & Reig, P. 2000, MNRAS 314, 290
- [17] Coe, M. J., & Orosz, J. A. 2000, MNRAS 311, 169
- [18] Corbet, R. H. D. 1984, A&A 141, 91
- [19] Corbet, R. H. D., Charles, P. A., Southwell, K. A., & Smale, A. P. 1997, ApJ 476, 833
- [20] Corbet, R., Marshall, F. E., Lochner, J. C., Ozaki, M., & Ueda, Y. 1998, IAU Circ. 6803
- [21] Corbet, R., Marshall, F. E., & Markwardt, C. B. 2001, IAU Circ. 7562
- [22] Corbet, R. H. D., Marshall, F. E., Coe, M. J., Laycock, S., & Handler, G. 2001, ApJ 548, L41
- [23] Corbet, R. H. D., & Peele, G. 2001, ApJ 562, 936
- [24] Cowley, A. P., Schmidtke, P. C., McGrath, T. K., Ponder, A. L., Fertig, M. R., Hutchings, J. B., & Crampton, D. 1997, PASP 109, 21
- [25] Crampton, D., Hutchings, J. B., & Cowley, A. P. 1978, ApJ 223, L79
- [26] Cusumano, G., Israel, G. L., Mannucci, F., Masetti, N., Mineo, T., & Nicastro, L. 1998, A&A 337, 772
- [27] Cusumano, G., Maccarone, M. C., Nicastro, L., Sacco, B., & Kaaret, P. 2000, ApJ 528, L25
- [28] Davies, R. D., Elliot, K. H., & Meaburn, J. 1976, Mem. R. astr. Soc. 81, 89
- [29] Dotani, T., Yamashita, A., Ezuka, H., Takahashi, K., Crew, G., Mukai, K., & the SIS Team 1997, ASCA News 5, 14
- [30] Filipović, M. D. et al. 1998a, A&AS 127, 119
- [31] Filipović, M. D. et al. 1998b, A&AS 130, 421
- [32] Filipović, M. D., Pietsch, W., & Haberl, F. 2000, A&A 361, 823

- [33] Filipović, M. D., Haberl, F., Pietsch, W., & Morgan, D. H. 2000, *A&A* 353, 129
- [34] Finger, M. H., & Wilson, C. A. 2000, *IAU Circ.* 7366
- [35] Gardiner, L. T., Sawa, T., & Fujimoto, M. 1994, *MNRAS* 266, 567
- [36] Gardiner, L. T., & Noguchi, F. 1996, *MNRAS* 278, 191
- [37] Giacconi, R., Murray, S., Gursky, H., Kellogg, E., Schreier, E., & Tananbaum, H. 1972, *ApJ* 178, 281
- [38] Girardi, L., Chiosi, C., Bertelli, G. & Bressan, A. 1995, *A&A* 298, 87
- [39] Gotthelf, E. V., Ueda, Y., Fujimoto, R., Kii, T., & Yamaoka, K. 2000, *ApJ* 543, 417
- [40] Green, D. A. 2000, ‘A Catalogue of Galactic Supernova Remnants (2000 August version)’, Mullard Radio Astronomy Observatory, Cavendish Laboratory, Cambridge, United Kingdom (available on the World-Wide-Web at “<http://www.mrao.cam.ac.uk/surveys/snrs/>”).
- [41] Haberl, F., Dennerl, K., & Pietsch, W. 1995, *A&A* 302, L1
- [42] Haberl, F., Filipovic, M. D., Pietsch, W., & Kahabka P. 2000, *A&AS* 142, 41
- [43] Haberl, F., & Sasaki, M. 2000, *A&A* 359, 573
- [44] Hayashi, I. et al. 1994, *PASJ* 46, L121
- [45] Henize, K. G. 1956, *ApJS* 2, 315
- [46] Hirayama et al. 1996, *ASCA News* 4, 18
- [47] Hughes, J. P., & Smith, R. C. 1994, *AJ* 107, 1363
- [48] Hughes, J. P. 1994, *ApJ* 427, L25
- [49] Hughes, J. P. et al. 1995, *ApJ* 444, L81
- [50] Hughes, J. P., Hayashi, I., & Koyama, K. 1998, *ApJ* 505, 732
- [51] Imanishi, K., Yokogawa, J., & Koyama, K. 1998, *IAU Circ.* 7040
- [52] Imanishi, K., Yokogawa, J., Tsujimoto, M., & Koyama, K. 1999, *PASJ* 51, L15

- [53] Inoue, H., Koyama, K., & Tanaka, Y. 1983, Proceedings of the IAU Symposium #101, "Supernova Remnants and their X-Ray Emission," ed. I. J. Danziger et al. (Venice, Italy, August 30–September 2, 1982), p. 535
- [54] In 't Zand, J. J. M., Swank, J., Corbet, R. H. D., & Markwardt, C. B. 2001, *A&A* 380, L26
- [55] Irwin, M. J., Demers, S. & Kunkel, W. E. 1990, *AJ* 99, 191
- [56] Ishisaki, Y., Ueda, Y., Kubo, H., Ikebe, Y., Makishima, K., & the GIS Team 1997, *ASCA News* 5, 26
- [57] Israel, G. L., Stella, L., Angelini, L., White, N. E., Giommi, P., & Covino, S. 1997, *ApJ* 484, L141
- [58] Israel, G. L. et al. 1998a, *IAU Circ.* 6999
- [59] Israel, G. L., Campana, S., Cusumano, G., Frontera, F., Orlandini, M., Santangelo, A., & Stella, L. 1998b, *A&A* 334, L65
- [60] Israel, G. L., Stella, L., Covino, S., Campana, S., & Mereghetti, S. 1999, *IAU Circ.* 7101
- [61] Israel, G. L. et al. 2000, *ApJ* 531, L131
- [62] Kaaret, P., Piraino, S., Halpern, J., & Eraculeous, M. 1999, *ApJ* 523, 197
- [63] Kahabka, P., Pietsch, W., & Hasinger, G. 1994, *A&A* 288, 538
- [64] Kahabka, P., & Pietsch, W. 1996, *A&A* 312, 919
- [65] Kahabka, P., & van den Heuvel, E. P. J. 1997, *ARA&A* 35, 69
- [66] Kahabka, P., & Pietsch, W. 1998, *IAU Circ.* 6840
- [67] Kahabka, P., & Li, X. -D. 1999, *A&A* 345, 117
- [68] Kahabka, P., Pietsch, W., Filipovic, M. D. & Haberl, F. 1999, *A&AS* 136, 81
- [69] Kahabka, P. 2000, *A&A* 354, 999
- [70] Kohno, M., Yokogawa, J., & Koyama, K. 2000, *PASJ* 52, 299

- [71] Kroupa, P., & Bastian, U. 1997, *New Astronomy* 2, 77
- [72] Lamb, R. C., Prince, T. A., Macomb, D. J. & Finger, M. H. 1999, *IAU Circ.* 7081
- [73] Leahy, D. A., Darbro, W., Elsner, R. F., Weisskopf, M. C., Sutherland, P. G., Kahn, S., & Grinslay, J. E. 1983, *ApJ* 266, 160
- [74] Lewin, W. H. G., van Paradijs, J., & Taam, R. E. 1995, in “X-Ray Binaries”, ed. W. H. G. Lewin, J. van Paradijs, & E. P. J. van den Heuvel (Cambridge University Press: Cambridge), 536
- [75] Liu, Q. Z., van Paradijs, J., & van den Heuvel, E. P. J. 2000, *A&AS* 147, 25
- [76] Liu, Q. Z., van Paradijs, J., & van den Heuvel, E. P. J. 2001, *A&A* 368, 1021
- [77] Lochner, J. C., Marshall, F. E., Whitlock, L. A., & Brandt, N. 1998, *IAU Circ.* 6814
- [78] Lochner, J. C. 1998, *IAU Circ.* 6858
- [79] Lucke, R., Yentis, D., Friedman, H., Fritz, G., & Shulman, S. 1976, *ApJ* 206, L25
- [80] Luks, T. 1994, *Rev. Mod. Astr.* 7, 171
- [81] Macomb, D. J., Finger, M. H., Harmon, B. A., Lamb, R. C., & Prince, T. A. 1999, *ApJ* 518, L99
- [82] Maragoudaki, F., Kontizas, M., Morgan, D. H., Kontizas, E., Dapergolas, A., & Livanou, E. 2001, *A&A* 364, 869
- [83] Marshall, F. E., Boldt, E. A., Holt, S. S., Mushotzky, R. F., Pravdo, S. H., Rothchild, R. E., & Serlemitsos, P. J. 1979, *ApJS* 40, 657
- [84] Marshall, F. E., Lochner, J. C., & Takeshima, T. 1997, *IAU Circ.* 6777
- [85] Marshall, F. E., & Lochner, J. C. 1998, *IAU Circ.* 6818
- [86] Masai, K. 1994, *ApJ* 437, 770
- [87] Mathewson, D. S., Cleary, M. N., & Murray, J. D. 1974, *ApJ* 190, 291
- [88] Mathewson, D. S., Ford, V. L., Dopita, M. A., Tuohy, I. R., Long, K. S., & Helfand, D. J. 1983, *ApJS* 51, 345

- [89] Mathewson, D. S., Ford, V. L., Dopita, M. A., Tuohy, I. R., Mills, B. Y., & Turtle, A. J. 1984, *ApJS* 55, 189
- [90] Mathewson, D. S. 1985, *Proc. ASA* 6, 104
- [91] Meaburn, J. 1980, *MNRAS* 192, 365
- [92] Mereghetti, S., Tiengo, A., Israel, G. L., & Stella, L. 2000, *A&A* 354, 567
- [93] Meyssonier, N., & Azzopardi, M. 1993, *A&AS* 102, 451
- [94] Mills, B. Y., Little, A. G., Durdin, J. M., & Kesteven, M. J. 1982, *MNRAS* 200, 1007
- [95] Murai, T., & Fujimoto, M. 1980, *PASJ* 32, 581
- [96] Murdin, P., Morton, D. C., & Thomas, R. M. 1979, *MNRAS* 1979, 186
- [97] Murphy, M. T., & Bessell, M. S. 2000, *MNRAS* 311, 741
- [98] Nagase, F. 1989, *PASJ* 41, 1
- [99] Nishiuchi, M. 2001, Ph. D. thesis, Kyoto University
- [100] Ohashi, T., et al. 1996, *PASJ* 48, 157
- [101] Ozaki, M., Corbet, R. H. D., Marshall, F. E., & Lochner, J. C. 2000, *Adv. Space Res.* 25, No. 3/4, 425
- [102] Paul, B., Nagase, F., Endo, T., Dotani, T., Yokogawa, J., & Nishiuchi, M. 2001, *ApJ* submitted
- [103] Petro, L., Feldman, F., & Hiltner, W. A. 1973, *ApJ* 184, L123
- [104] Price, R. E., Groves, D. J., Rodrigues, R. M., Seward, F. D., Swift, C. D., & Toor, A. 1971, *ApJ* 168, L7
- [105] Putman, M. E. et al. 1998, *Nature* 394, 752
- [106] Raymond, J. C., & Smith, B. W. 1977, *ApJS* 35, 419
- [107] Reig, P., & Roche, P. 1999, *MNRAS* 306, 100
- [108] Rosado, M., Le Coarer, E., & Georgelin, P. 1994, *A&A* 286, 231

- [109] Russell, S. C., & Dopita, M. A. 1992, *ApJ* 384, 508
- [110] Sakano, M. 2000, Ph.D. thesis, Kyoto University
- [111] Sakano, M., Torii, K., Koyama, K., Maeda, Y., & Yamauchi, S. 2000, *PASJ* 52, 1141
- [112] Santangelo, A., Cusumano, G., Dal Fiume, D., Israel, G. L., Stella, L., Orlandini, M., & Parmar, A. N. 1998, *A&A* 338, L59
- [113] Sasaki, M., Haberl, F., & Pietsch, W. 2000, *A&AS* 147, 75
- [114] Sasaki, M., Haberl, F., Keller, S., & Pietsch, W. 2001, *A&A* 369, L29
- [115] Sawa, T., Fujimoto, M., & Kumai, Y. 1999, Proceedings of the IAU Symposium #190, “New Views of the Magellanic Clouds,” ed. Y. -H. Chu et al. (Victoria, British Columbia, Canada, 12–17 July 1998), p. 499
- [116] Schmidtke, P. C. et al. 1999, *AJ* 117, 927
- [117] Serlemitsos, P. J. et al. 1995, *PASJ* 47, 105
- [118] Southwell, K. A., & Charles, P. A. 1996, *MNRAS* 281, L63
- [119] Sreekumar, P., & Fichtel, C. E. 1991, *A&A* 251, 447
- [120] Sreekumar, P. et al. 1993, *Phys. Rev. Lett.* 70, 127
- [121] Stanimirović, S., Staveley-Smith, L., Dickey, J. M., Sault, R. J., & Snowden, S. L. 1999, *MNRAS* 302, 417
- [122] Stevens, J. B., Coe, M. J., & Buckley, D. A. H. 1999, *MNRAS* 309, 421
- [123] Tanaka, Y., Inoue, H., & Holt, S. S. 1994, *PASJ* 46, L37
- [124] Torii, K., Yokogawa, J., Imanishi, K., & Koyama, K. 2000a, *IAU Circ.* 7428
- [125] Torii, K., Kohmura, T., Yokogawa, J., & Koyama, K. 2000b, *IAU Circ.* 7441
- [126] Tsujimoto, T., Nomoto, K., Yoshii, Y., Hashimoto, M., Yanagita, S., & Thielemann, F. -K. 1995, *MNRAS* 277, 945
- [127] Tsujimoto, M., Imanishi, K., Yokogawa, J., Koyama, K. 1999, *PASJ* 51, L21

- [128] Ueda, Y. 1996, Ph.D. thesis, University of Tokyo
- [129] Ueda, Y. et al. 1999, *ApJ* 518, 656
- [130] Ueno, M., Yokogawa, J., Imanishi, K., & Koyama, K. 2000a, *PASJ* 52, L63
- [131] Ueno, M., Yokogawa, J., Imanishi, K., & Koyama, K. 2000b, *IAU Circ.* 7442
- [132] van den Bergh, S. 2000, *PASP* 112, 529
- [133] Vallenari, A., Chiosi, C., Bertelli, G., & Ortolani, S. 1996, *A&A* 309, 358
- [134] Vrtilik, S. D., Raymond, J. C., Boroson, B., Kallman, T., Quaintrell, H., & McCray, R. 2001, *ApJ* 563, L139
- [135] Wang, Q., & Wu, X. 1992, *ApJS* 78, 391
- [136] White, N. E., Swank, J. H., & Holt, S. S. 1983, *ApJ* 270, 711
- [137] Whitlock, L., & Lochner, J. C. 1994, *ApJ* 437, 841
- [138] Wilson, C. A., & Finger, M. H. 1998, *IAU Circ.* 7048
- [139] Wojdowski, P., Clark, G. W., Levine, A. M., Woo, J. W., & Zhang, S. N. 1998, *ApJ* 502, 253
- [140] Ye, T., Turtle, A. J., & Kennicutt, Jr., R. C. 1991, *MNRAS* 249, 722
- [141] Ye, T., Amy, S. W., Wang, Q. D., Ball, L., & Dickel, J. 1995, *MNRAS* 275, 1218
- [142] Yokogawa, J., & Koyama, K. 1998a, *IAU Circ.* 6853
- [143] Yokogawa, J., & Koyama, K. 1998b, *IAU Circ.* 7028
- [144] Yokogawa, J., & Koyama, K. 1998c, *IAU Circ.* 7009
- [145] Yokogawa, J., Imanishi, K., Tsujimoto, M., Kohno, M., & Koyama, K. 1999, *PASJ* 51, 547
- [146] Yokogawa, J., Imanishi, K., Ueno, M., & Koyama, K. 2000a, *PASJ* 52, L73
- [147] Yokogawa, J., Torii, K., Imanishi, K., & Koyama, K. 2000b, *PASJ* 52, L37

- [148] Yokogawa, J., Torii, K., Kohmura, T., Imanishi, K., & Koyama, K. 2000c, PASJ 52, L53
- [149] Yokogawa, J., Paul, B., Ozaki, M., Nagase, F., Chakrabarty, D., & Takeshima, T. 2000d, ApJ 539, 191
- [150] Yokogawa, J., Imanishi, K., Tsujimoto, M., Nishiuchi, M., Koyama, K., Nagase, F., & Corbet, R. H. D. 2000e, ApJS 128, 491
- [151] Yokogawa, J., & Koyama, K. 2000, IAU Circ. 7361
- [152] Yokogawa, J., Torii, K., Kohmura, T., & Koyama, K. 2001a, PASJ 53, L9
- [153] Yokogawa, J., Torii, K., Kohmura, T., & Koyama, K. 2001b, PASJ 53, 227
- [154] Yokogawa, J., Imanishi, K., Koyama, K., Nishiuchi, M., & Mizuno, N. 2001c, PASJ in press
- [155] Zaritsky, D., Harris, J., Grebel, E. K., & Thompson, I. B. 2000, ApJ 534, L53

Acknowledgment

I am deeply grateful to Prof. K. Koyama for his continuous guidance throughout the five years of my graduate course and his leadership in the ASCA SMC survey project. I also thank my collaborators, Mr. K. Imanishi, Mr. M. Tsujimoto, and Dr. M. Nishiuchi, for their helpful comments and sharing in data analyses throughout the survey project.

Some of new pulsars have not been discovered without efforts made by Dr. K. Torii, Mr. M. Ueno, and Mr. T. Kohmura. Collaboration with Prof. F. Nagase, Dr. B. Paul, and Dr. M. Ozaki in the analysis of XTE J0111.2–7317 was very good experience. Comments from Dr. N. Mizuno and Dr. K. Yoshita were helpful in the analysis of SNRs.

I thank all the members of the Cosmic-ray laboratory in Kyoto University for the daily discussion and insightful comments. Of course I thank you, who are interested in this thesis and have just finished reading it!